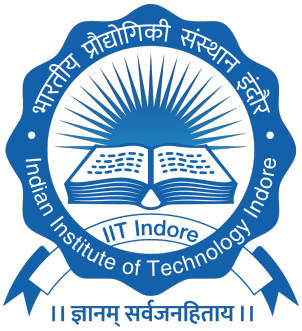
Constraining Temperature Fluctuations in the IGM with Lyα Forest at $4 < z < 5$

M.Sc Thesis

By
Kartik Kambhampati V.



DEPARTMENT OF ASTRONOMY, ASTROPHYSICS & SPACE ENGINEERING
INDIAN INSTITUTE OF TECHNOLOGY INDORE
May 17, 2026

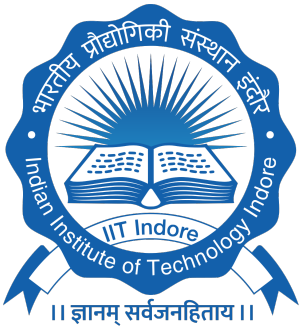
Constraining Temperature Fluctuations in the IGM with Lyα Forest at $4 < z < 5$

A THESIS

Submitted in partial fulfillment of the requirements for the awards of the degree
of
Master of Science

by

Kartik Kambhampati V.



DEPARTMENT OF ASTRONOMY, ASTROPHYSICS & SPACE ENGINEERING

INDIAN INSTITUTE OF TECHNOLOGY INDORE

May 17, 2026

INDIAN INSTITUTE OF TECHNOLOGY INDORE

CANDIDATE'S DECLARATION

I hereby certify that the work which is being presented in the thesis entitled **Constraining Temperature Fluctuations in the IGM with Lyα Forest at 4 < z < 5** in the partial fulfillment of the requirements for the award of the degree of **MASTER OF SCIENCE** and submitted in the **DEPARTMENT OF ASTRONOMY, ASTROPHYSICS AND SPACE ENGINEERING, Indian Institute of Technology Indore**, is an authentic record of my own work carried out during the time period from **July 2025 to May 2026** under the supervision of **Dr. Prakash Gaikwad**, **Assistant Professor**, **Department of Astronomy, Astrophysics and Space Engineering.**

The matter presented in this thesis has not been submitted by me for the award of any other degree of this or any other institute.

07/05/2026

Signature of the student with date
(Kartik Venkataramana Kambhampati)

This is to certify that the above statement made by the candidate is correct to the best of my/our knowledge.

07 May 2026

Signature of the Supervisor of

M.Sc. thesis with date

(Dr. Prakash Gaikwad)

Kartik Venkataramana Kambhampati has successfully given his M.Sc. Oral Examination held on **05/05/2026**

Signature(s) of Supervisor(s) of MSc thesis
Date: 7 May 2026

Programme Coordinator, M.Sc.
Date: 08/05/2026

Convenor, DPGC
Date: 08/05/2026

HoD, DAASE
Date: 08/05/2026

ACKNOWLEDGEMENTS

First and foremost, I want to express my gratitude to my thesis supervisor **Dr. Prakash Gaikwad** for his wonderful mentorship throughout the project. His constant guidance and discussions on the project made it easier for me to overcome the challenges I faced while working on the project. His approach towards solving a problem by delving into the smallest technical details, while also developing the necessary and right physical intuition has uplifted my learning and problem handling approach. I also thank him for the constant support and guidance he provided during my entrance exams and PhD interviews. Working under his mentorship was a wonderful research experience for me.

A big thanks to my lab partner, **Manpreet**, for always being for discussions related to project and PhD applications. His enthusiasm for attending seminars and talks is what I would like to have in me.

I will always be grateful to **my parents**, **my brother** and my guru **Munjal Mehta** Sir. Their blessings and guidance have carried me until now. I could not have imagined studying in this institute without their support and the discipline of work they have taught me. Thanks for always being there for me.

I thank **Kaivan**, my table tennis partner, for making me part of the most exciting games I have had on this campus. A big thanks to my batch mates **Nityanand, Mayukh, Vishal, Sangeeta, Sangeetha, Kanishka, and Aditya**.

Last but not the least, I want to thank my dearest roommates **Meet** and **Naru**. I will always cherish our vacation trips, movie nights, and chai sessions. Thank you for making my campus life beautiful.

Kartik Kambhampati

ABSTRACT

The Epoch of Reionization (EoR) marks as a key phase transition event in the evolution of the Universe. During EoR the first star-forming galaxies, with the emission of UV radiation, ionize the neutral hydrogen present in the intergalactic medium (IGM). Several studies have suggested that this process was extended and inhomogeneous in nature. The denser regions in the Universe collapsed first, forming bright sources that ionized their surroundings, heating up the gas to large temperatures. Whereas, less dense regions remained neutral and cool till longer time. The difference in the timing of ionization of different regions produces spatial temperature fluctuations in the IGM during the end stages of reionization that continue to persist even shortly after hydrogen reionization. The objective of the thesis is to probe and constrain these temperature fluctuations induced by inhomogeneous reionization.

We work with high resolution simulations, designed to produce controlled temperature fluctuations in the IGM using different reionization histories and temperature for inhomogeneous reionization of the hydrogen. To detect the temperature fluctuations, we use the Lyα forest in the redshift $4 \leq z \leq 5$ as our observational tool to probe the IGM. The synthetic Lyα forest spectrum are generated at $z = 4.2$, 4.6, and 5.0, with $\Delta z \approx 0.088$. Additionally, another set of the Lyα forest spectrum at $z = 4.4$ with $\Delta z = 0.4$ are generated for different reionization models.

We begin a with qualitative assessment of the temperature fluctuations arising from different models their effect absorption features of the Lyα forest. Following this, the 1D flux power spectrum (FPS) and wavelet statistics of the Lyα forest as our statistical tools to quantify the effects of temperature fluctuations across different velocity scales. The FPS is calculated for different reionization models probing k modes ranging between $0.0001 \lesssim k$ (km^{-1} s) $\lesssim 0.2$. This would help to study the impact of temperature fluctuations on the shape of the power at small and large velocity scales. We further take the ratios of the power from inhomogeneous with the homogeneous model in order to detect large scale temperature fluctuations in the IGM. Finally, we perform wavelet analysis on the Lyα forest and draw the distributions of wavelet amplitudes for different models. Our analysis aims to detect the large scale temperature fluctuations in the IGM because of patchy reionization. Further, we want to distinguish between different reionization models. This would help to improve our understanding of the ionizing sources, timing and the morphology of the EoR.

Contents

List of Figures iii

List of Tables vii

1 Introduction 1
- 1.1 An overview to the history of the Universe . . . 1
- 1.2 First stars and galaxies . . . 2
- 1.3 Observational probes of Reionziation . . . 3
  - 1.3.1 Cosmic Microwave Background (CMB) . . . 4
  - 1.3.2 The Lyα forest . . . 5
  - 1.3.3 HI 21 cm emission . . . 7
- 1.4 Research Objectives . . . 9
- 1.5 Outline . . . 10

2 Physics of the intergalactic medium 11
- 2.1 Heating of the IGM . . . 11
  - 2.1.1 Photoionization heating . . . 11
  - 2.1.2 Shock Heating . . . 12
- 2.2 Physics of reionization . . . 12
- 2.3 IGM temperature density relation (TDR) . . . 14

3 Simulation 16
- 3.1 Cosmological hydrodynamical simulation . . . 16
- 3.2 Modelling of temperature fluctuations in the IGM . . . 17
- 3.3 Reionization Models . . . 18

4 Method 20
- 4.1 Generating Lyα forest . . . 20
- 4.2 Effects of temperature on Lyα absorption features . . . 22
- 4.3 Lyα Statistics . . . 24
  - 4.3.1 1D Flux Power Spectrum . . . 24
  - 4.3.2 Wavelet statistics . . . 25

5 Results 27
- 5.1 Density, reionization redshift, and temperature maps . . . 27
  - 5.1.1 Density and reionization redsift maps . . . 28

5.1.2 Temperature fluctuations in inhomogeneous reionization models at $z = 4$ . . . 28
5.2 Temperature Density Relation for inhomogeneous reionization models . . . 30
5.3 Evolution of T_0 . . . 31
5.4 Effects of temperature fluctuations on the absorption features of the Lyα forest . . . 33
5.5 1D flux power spectrum . . . 34
5.5.1 Sensitivity of 1D flux power spectrum to T_0 and γ . . . 34
5.5.2 Effects of temperature fluctuations on the flux power spectrum . . . 35
5.5.3 Large Scale Power Enhancement . . . 36
5.5.4 Flux power spectrum on small velocity scales . . . 38
5.6 Wavelet Amplitude (A_n) . . . 38
5.6.1 Effects of temperature fluctuations on the wavelet amplitude . . . 39
5.6.2 Probability distribution function (PDF) of $\langle log(A_n) \rangle$ . . . 40

6 Summary and Future Scope **44**
6.1 Summary . . . 44
6.2 Future Scope . . . 47

List of Figures

1.1 Schematic representing the major events in the evolution of the Universe from the Big Bang to the present day. Image credits: National Astronomical Observatory of Japan 1

1.2 Schematic illustration of the Thompson scattering of CMB photons. The red dots represent free electrons and the blue dots with circle represent hydrogen nuclei. The dashed black curved arrows represent the incoming CMB photons and the yellow solid curved arrows represents the scattered CMB photons by free electrons. Image credits: Chakraborty & Tirthankar Roy Choudhury 2026 4

1.3 Schematic illustration of the Lyα forest. The bright source on top right corner represents a quasar whose intrinsic spectrum is shown in solid white curve. The Lyα absorption features are represented in the green lines. Image credit: Kavli Institute for Cosmology, Cambridge (KICC) 5

1.4 Figure shows the evolution of brightness temperature of the 21 cm signal relative to CMB temperature. The upper panel shows the slice from simulation of the evolution in the spatial fluctuations in the 21 cm brightness temperature. The lower panel shows the sky-average global 21 cm signal. Image credits: Pritchard & Abraham Loeb 2012. 8

2.1 Comparison of the temperature density relation between cold (panel A) and hot (panel B) IGM at $z = 5.8$. In both the models the best fit obtained using the TDR relation from Eq. 2.8 is shown by dashed black line. The color scheme represents the density of particle from the simulation box. High heating makes the temperature almost independent of density, giving the hot model a flat slope with higher $T_{\rm o}$. The values ($T_{\rm o}$, γ) calculated for hot and cold model are (7413 K, 1.22) and (14191 K, 1.02), respectively. Figure credit: Gaikwad et al. 2020 15

3.1 Figure shows the evolution of the volume-averaged neutral hydrogen fraction $\langle f_{\rm HI} \rangle$ for the early (dashed blue), mid (dashed green), and late (dashed red) models from redshift 10 to 4. The y-axis shows the neutral fraction in log-scale. The different markers represent the constraints on $f_{\rm HI}$ from measurements the Lyα forest (McGreer et al. 2015; Zhu et al. 2022; Jin et al. 2023; Davies et al. 2026; Spina et al. 2024; Zhu 2024) and damping wing analysis of QSO proximity regions (Greig et al. 2017; Bañados et al. 2018; Mason et al. 2018; Greig et al. 2019; Wang et al. 2020; Yang et al. 2020b) 19

4.1 Sample of generated Lyα forest spectrum in the redshift range $4.0 \leq z \leq 4.4$ with a mean redshift of $\bar{z} = 4.2$. The upper panel shows the Lyα optical depth profile and the lower panel shows the corresponding normalized Lyα flux profile generated for $T_{\rm o}$ = 10,000 K and $\gamma = 1.6$. 22

4.2 Figure illustrates the sensitivity of the Lyα absorption feature on the Doppler parameter (b) and neutral hydrogen column density ($\rm N_{HI}$). In the right panel, $\rm N_{HI}$ is fixed at 10^{13} cm^{-2}. The blue and the red profile are for $b = 1 \times 10^6$ and 2×10^6 cm s^{-1}, respectively. In the left panel b is fixed at 1×10^6 cm s^{-1}. The blue and red curves are for $\rm N_{HI} = 10^{13}$ and 10^{18} cm^{-2}, respectively. 23

4.3 Figure shows the Morlet wavelet filter for $s_{\rm n} = 35$ km s^{-1}. The solid blue and the dashed red curves show the real and the imaginary part of the filter. 26

5.1 Slice of the density field from Sherwood simulations at $z = 4$. The region highlighted in the white circle shows a cosmic void with $\Delta \lesssim \frac{1}{10}$. 27

5.2 Figure shows slice through the reionization redshift z_{reion} maps for the early (left panel), mid (center panel), and late (right panel). The blue (red) patches represent early (late) ionized regions. In all three panels the region shown in white circle is ionized at $5 \lesssim z \lesssim 6$. 28

5.3 Figure shows slices of temperature field from the simulation at $z = 4$. From left to right, the panels correspond to early, mid, and late reionization histories. From upper to lower the reionization temperature T_{reion} increases from 10,000 K, 20,000 K , and 30,000 K. On the upper-left corner of each panel the mean IGM temperature $\log(T_{\rm o})$ is indicated. With $T_{\rm reion}$ the difference in spatial temperature fluctuations in the early and late models increases. The hot region present systematically in the lower panel for a constant $T_{\rm reion}$ = 30,000 K) for all models are due to recent heating of cosmic voids. 29

5.4 Comparison between temperature-density relation (TDR) between the early (left panel), mid (center panel), and late (right panel) models at $z = 4.2$ and $T_{\rm reion}$ = 20,000 K. The best fit in each panel is represented by a dashed black line. The stars in green represent the median temperature corresponding to each $\log(\Delta)$ bin. The mean IGM temperature $T_{\rm o}$ and the slope of the TDR, γ, is indicated on the upper right corner of each panel. The scatter in the temperature reduces as the difference in the reionization redshift for different cell decreases. 30
5.5 Comparison between temperature-density relation (TDR) for the mid model with $T_{\rm reion}$ 20,000 K at z; 4.2 (left panel), 4.6 (mid panel), and 5.0 (right panel). The best fit in each panel is represented by a dashed black line. The stars in green represent the median temperature corresponding to each $\log(\Delta)$ bin. The mean IGM temperature $T_{\rm o}$ and the slope of the TDR, γ, is indicated on the upper right corner of each panel. The less scatter in temperature as we move to lower redshifts can be attributed to fading of temperature fluctuations due to cosmic expansion. . . 31
5.6 Figure shows the evolution of the temperature at cosmic mean density ($\Delta = 1$), $T_{\rm o}$, as a function of redshift for the early, mid, and late reionization models. The green, orange, and blue shaded areas indicate the $T_{\rm o}$ values foe the early, mid, and late models, calculated at each redshift bin specified in Section 3.3 by varying the reionization temperature $T_{\rm reion}$ from 5000 to 50,000 K in steps of 500 K. 32
5.7 Comparison of the Lyα absorption features for hot (solid red) and cold (solid blue) IGM model. The values for ($T_{\rm o}$; γ) for hot and cold model are (20,000 K; 1.3) and (10,000 K; 1.3), respectively. 33
5.8 Comparison of the Lyα absorption in the early (top panel) and late (bottom panel) reionization models, shown for two reionization temperatures: $T_{\rm reion}$ = 10,000 K (solid blue curve) and $T_{\rm reion}$ = 30,000 K (dashed red curve). 34
5.9 The figure illustrates the effect of varying T_0 and γ on the flux power spectrum (FPS). The power spectra are computed for three parameter combinations: $(T_0, \gamma) = (10{,}000\,\mathrm{K},\ 1.3)$, $(10{,}000\,\mathrm{K},\ 1.6)$, and $(20{,}000\,\mathrm{K},\ 1.3)$, shown by the solid blue, green, and red curves, respectively. The parameters $T_{\rm o}$ and γ mainly affects the power spectrum at scales $k \gtrsim 10^{-2}\mathrm{km}^{-1}\mathrm{s}$. 34
5.10 The figure shows the 1D flux power spectrum for inhomogeneous models at $z = 4.2$ for different $T_{\rm reion}$ values. The power for the early, mid, and late models are represented in solid blue, green, and red lines. From left to right panel the reionization temperature $T_{\rm reion}$ is varied from 10,000 K to 30,000 K. 35

5.11 The figure shows the evolution of FPS for the early (solid blue), mid (solid green), and late (solid red) models with redshift. The reionization temperature, $T_{\rm reion}$ is set to 20,000 K. From left to right panel the redshift increases as $z = 4.2$ (left), 4.6, (center), 5.0 (right). 36
5.12 Comparison of the ratio of the power, $R(k)$, computed for the early (solid blue curve), mid (solid green curve), and late (solid red curve) models at $z = 4.2$, for three reionization temperatures; (i) $T_{\rm reion}$ = 10,000 K (left panel), (ii) $T_{\rm reion}$ = 20,000 K (center panel), and (iii) $T_{\rm reion}$ = 30,000 K (right panel). 37
5.13 Comparison between FPS of the early (blue solid) and late (red solid) model at $z = 4.2$ for $T_{\rm reion}$ = 30,000 K. The dashed black solid line represents a velocity separation of $v = 35$ km s^{-1}. At $k \gtrsim 0.1$ km^{-1} s the early model shows a higher power because of the rapidly varying absorption features arising from strong temperature fluctuations compared to the late model. 38
5.14 Figure shows the variation in the Lyα flux (top panel) and the log wavelet amplitude, $\log(A_{\rm n})$ (bottom panel), for the early (solid blue) and late (dashed red) models for $T_{\rm reion} = 30{,}000$ K at $z = 4.4$. The smoothing scale adopted for the wavelet filter is $s_{\rm n} = 35$ km s^{-1} 39
5.15 Similar to figure 5.14, instead for $T_{\rm reion} = 10{,}000$ K. 40
5.16 Comparison for $\log(A_{\rm n})$ between the early (blue solid) and late (dashed red) models for three smoothing scales. (i) $s_{\rm n} = 35$ km s^{-1} (top panel), (ii) $s_{\rm n} = 50$ km s^{-1} (middle panel), and (iii) $s_{\rm n} = 100$ km s^{-1} (bottom panel). For all the panels the reionization temperature is set at $T_{\rm reion} = 30,000$ K. 40
5.17 Comparison of the PDF of $\log(A_{\rm n})$ between the early (blue solid) and late (dashed red) models for two $T_{\rm reion}$ values. (i) $T_{\rm reion}$ = 10,000 K (upper panel) and (ii) $T_{\rm reion}$ = 30,000 K (lower panel). The wavelet filter scale s_n is fixed at 35 km s^{-1}. 41
5.18 Comparison of the PDF of $\log(A_{\rm n})$ between the early (blue solid) and late (dashed red) models for two $T_{\rm reion}$ values. (i) $T_{\rm reion}$ = 10,000 K (upper panel) and (ii) $T_{\rm reion}$ = 30,000 K (lower panel). The wavelet filter scale s_n is fixed at 50 km s^{-1}. 42
5.19 Comparison of the PDF of $\log(A_{\rm n})$ between the early (blue solid) and late (dashed red) models for two $T_{\rm reion}$ values. (i) $T_{\rm reion}$ = 10,000 K (upper panel) and (ii) $T_{\rm reion}$ = 30,000 K (lower panel). The wavelet filter scale s_n is fixed at 100 km s^{-1}. 43

List of Tables

5.1 Mean IGM temperature T_0 and slope γ at $z = 4.2$ 32
5.2 Mean IGM temperature T_0 and slope γ at $z = 4.6$ 32
5.3 Mean IGM temperature T_0 and slope γ at $z = 5.0$ 33

CHAPTER 1

Introduction

1.1 An overview to the history of the Universe

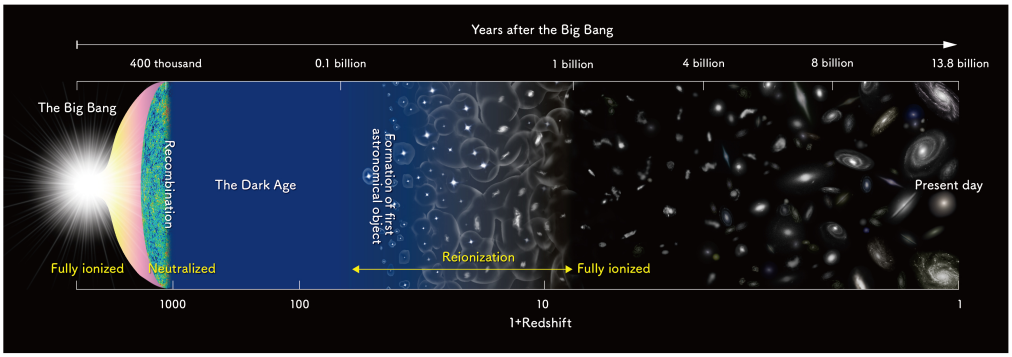


Figure 1.1: Schematic representing the major events in the evolution of the Universe from the Big Bang to the present day. Image credits: National Astronomical Observatory of Japan

The evolution of the Universe begins with a rapid accelerated expansion known as ”inflation” (Guth 1981; Linde 1982; Albrecht & Steinhardt 1982). The theory was proposed to explain the homogeneity, isotropy, and flatness of the Universe, which could not be explained by the hot Big Bang model. The theory also explains the generation of initial density fluctuations, which at later times are essential in structure formation. Following inflation, the Universe entered a very hot and dense phase, where matter and radiation were coupled together, maintaining thermal equilibrium. During the first minutes ($\sim$ 3-20 minutes) after the Big Bang, when the temperature of the Universe was about 10^9 K, the nuclei of elements including hydrogen, helium, and lithium were formed. The theoretical framework for this is called Big Bang nucleosynthesis (Gamow 1946; Alpher et al. 1948). About 380,000 years after the Big Bang, the Universe cooled further, allowing matter and radiation to decouple. This is called as Recombination epoch, which marks as the first phase transition event in the Universe. During this period, the hydrogen and helium nuclei captured free electrons to form the first neutral atoms, allowing radiation to move freely in the Universe. This radiation is observed at present time as the Cosmic Microwave Background (CMB), first discovered by Penzias & Wilson 1965 which is the earliest snapshot of the Universe.

After the recombination epoch, the Universe entered a phase called the "Dark Ages". During this phase, the Universe had cooled to below 10^3 K and was mostly filled with neutral hydrogen. At this point, no luminous sources have formed yet. Thereafter, the small perturbations in the matter density from CMB slowly grew larger under gravitational instability, eventually leading to the formation of the first stars and galaxies. The radiation emitted from these bright sources with energy $E_\gamma \geq 13.6$ eV started to ionize neutral hydrogen (Madau et al. 1999) (see, Figure 1.4, where roughly between 0.1 and 1 billion years after the Big Bang sources are shown surrounded by white bubbles that represent the ionized regions. The gas within these bubbles is ionized, while the rest is neutral). As the Universe evolved, more galaxies formed, participating in the ionization, eventually ionizing neutral hydrogen almost entirely. The formation of singly ionized helium (HeI $\rightarrow$HeII) was carried out by the first stars and galaxies that ionize hydrogen. This requires photons with an energy $E_\gamma \geq 24.6$ eV. However, the formation of doubly ionized helium (HeII $\rightarrow$HeIII) occurs later. This requires photons with energy $E_\gamma \geq 54.4$ eV that are produced by accreting supermassive black holes called quasars (Miralda-Escudé et al. 2000; R. H. Becker et al. 2001; Fan et al. 2006). This entire period in which hydrogen and helium in the Universe is ionized is known as the Epoch of Reionization (EoR). This is the second phase transition event in the Universe, as it went from a neutral state to again in an ionized state. The study of the Epoch of Reionization is essential as it bridges the early Universe, during the time at CMB, with the present Universe. It serves as a crucial link to understand the formation and evolution of the sources that participated in reionization, mainly the young first star forming galaxies and quasars. The next section discusses the formation of the first stars and galaxies.

1.2 First stars and galaxies

The formation of the first luminous sources began at the end of the dark ages. With time, the small perturbations present in the matter density during recombination began to grow under the influence of gravity. The regions that were slightly overdense became denser by pulling more matter and eventually collapsing under its own gravity. The collapsed matter formed the first bound structures known as dark matter haloes. These structures continue to grow by accreting more matter or by merging with other surrounding haloes. The dark matter haloes serve as a potential well in which baryonic matter falls. The baryonic gas falling into these haloes gains kinetic energy and heats up, whereas a large fraction of baryonic gas remains in the intergalactic medium (IGM). The ability of the gas to cool will determine whether star formation could occur. When cooling is efficient, the gas can condense and break down into smaller fragments. This further led to the formation of the first stars, marking the beginning of cosmic dawn.

Star formation in these early haloes depends on the ability of the gas to cool and lose energy. Gravity tries to pull the matter inward and drives the collapse of gas. During this process the temperature of the gas increases as a result of the conversion of gravitational potential energy into thermal energy. This creates a

thermal pressure that acts opposite to the gravitational pull, slowing further collapse. Therefore, cooling is necessary for star formation to proceed. In the early Universe, which consisted mainly of hydrogen and helium, cooling mechanisms were limited. In more massive haloes with mass $\gtrsim 10^8$ $M_\odot$, where temperatures exceed 10^4 K, cooling occurs through atomic transitions. In smaller haloes (minihaloes) with mass $\sim 10^4 - 10^5$ $M_\odot$ cooling is possible through molecular hydrogen, which allows the gas to collapse and form stars (Haiman 2000).

The first generation of stars are known as Population III stars, that formed in the minihaloes (Abel et al. 2002; Bromm & Larson 2004; Greif et al. 2011). These stars are formed from metal-free gas and are expected to be massive. They were also efficient producers of ionizing radiation with energies much higher than present day stars. The radiation emitted by Population III stars in the energy range $E_\gamma \sim 11.2 - 13.6$ eV falls into the Lyman - Werner band of molecular hydrogen H_2. These photons could not ionize hydrogen. However, they were able to dissociate molecular hydrogen, which is the main coolant responsible for star formation. As a result, the formation of subsequent stars was suppressed (Haiman 2000). The star formation rate of Population III stars in minihaloes reached a saturation level $\sim 10^{-5} - 10^{-4}$ $M_\odot$ year^{-1} cMpc^{-3} at redshifts $\sim 20 - 30$ (Trenti et al. 2009). Simulations performed by Abel et al. 2002 and Greif et al. 2011 showed that even though the Population III stars fall into the top-heavy stellar population, because of such a low star formation rate only a small-fraction of neutral hydrogen in the IGM is ionized. In addition, many of Polulation III stars end their lives in supernova explosions, which release heavy elements into the surrounding gas. This enrichment allows the gas to cool more efficiently and leads to the formation of later generations of stars, known as Population II stars (Woosley et al. 2002; Kulkarni et al. 2013). Studies by Barkana & A. Loeb 2001 and Bromm & Yoshida 2011 suggest that the first Galaxies formed at redshift ~ 10 in halos with masses $\gtrsim 10^8$ $M_\odot$. The James Webb Space Telescope (JWST) supports this by observing seven galaxies at redshifts $\sim 9 - 11$ (Napolitano et al. 2025). These halos in which the first galaxies formed were able to cool by atomic transitions and harbor more sustained star-formation. These galaxies play an important role in heating and ionizing the intergalactic medium.

1.3 Observational probes of Reionziation

The Epoch of Reionization (EoR) marks as an important phase in the evolution of the Universe, as the Universe makes a transition from neutral to ionized state. Since this process cannot be directly observed, we rely on observational probes. Since no single probe can help us develop an entire understanding of EoR, therefore we use diverse set of probes and perform a multi-wavelength study. The following section briefly discusses the observational probes of EoR, highlighting their origin, the constraints they place on the timing of EoR, and the physical insights they offer.

1.3.1 Cosmic Microwave Background (CMB)

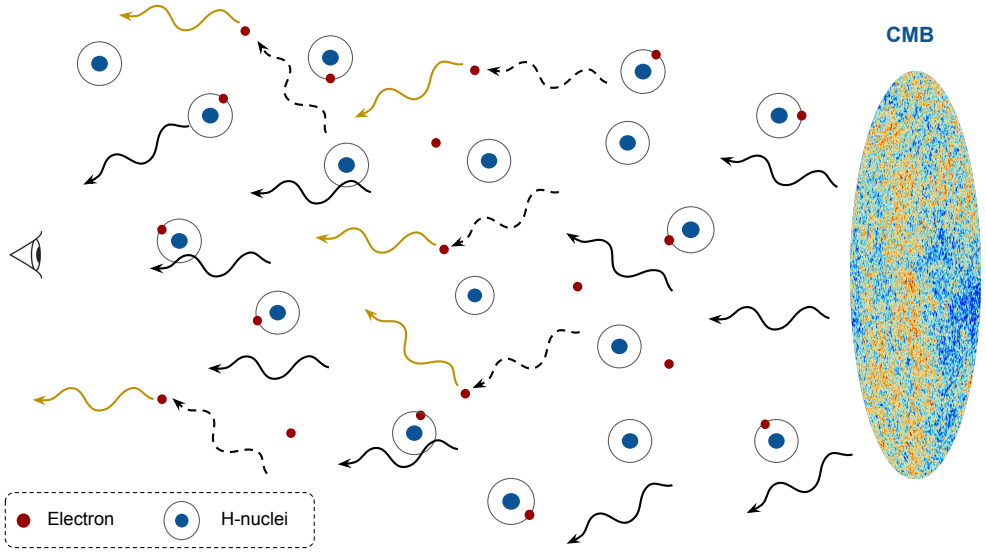


Figure 1.2: Schematic illustration of the Thompson scattering of CMB photons. The red dots represent free electrons and the blue dots with circle represent hydrogen nuclei. The dashed black curved arrows represent the incoming CMB photons and the yellow solid curved arrows represents the scattered CMB photons by free electrons. Image credits: Chakraborty & Tirthankar Roy Choudhury 2026

The Cosmic Microwave Background (CMB) is the radiation that had decoupled from baryonic matter during the Epoch of Recombination. This radiation has been propagating freely through the Universe until the Epoch of Reionization. During EoR, the ionization of neutral hydrogen by the first stars and galaxies also produced free electrons. The CMB photons are re-scattered by these electrons as they propagate through the IGM. This interaction leaves an imprint of the reionization on the temperature and polarization anisotropies of CMB photons, making it a powerful probe of the integrated ionization history of the Universe (Hu & White 1997; Zaldarriaga et al. 1997). The strength of this interaction depends on the column density of free electrons along the line of sight, which is measured by the electron scattering optical depth, denoted as τ_{el}, where

$$\tau_{\rm el} = c\,\sigma_T\,\bar{n}_H \int_{t_{\rm CMB}}^{t_0} dt\,\chi_{\rm He}(t)\,Q_{\rm HII}(t)\,a^{-3}(t). \tag{1.1}$$

In the above equation σ_T is the Thompson scattering cross-section, t_0 represents present time, $t_{\rm CMB}$ is the time at the origin of CMB, $\bar{n}_H$ is mean hydrogen density, $\chi_{\rm He}$ is helium correction factor, $Q_{\rm HII}$ is the ionized hydrogen filling factor, a is the cosmological scale factor. The combination $\bar{n}_H \chi_{\rm He}(t)\,Q_{\rm HII}(t)\,a^{-3}(t)$ represents the number density of free electrons. As CMB photons are scattered by free electrons, it damps the amplitude of primary CMB temperature and polarization anisotropies by a factor of $e^{-\tau_{el}}$. When a free electron interacts with CMB photon it produces a linearly polarized radiation called as E-mode polarization. This results in a an enhancement in the polarization power spectrum

at low multipoles, often referred to as the "reionization bump" and serves as signature of cosmic reionization. The first detection of "bump" came from the first-year observations by the WMAP satellite (Bennett et al. 2003). The electron scattering optical depth was measured to $\tau_{el} = 0.17 \pm 0.06$, corresponding to a mid-point of reionization $z_{\rm mid}$[1] $\approx 17 \pm 4$ (Spergel et al. 2003). The latest observations by the Planck satellite measured $\tau_{el} = 0.054 \pm 0.007$ which corresponds to a mid-point of reionization $z_{\rm mid} = 7.7 \pm 0.7$ (Planck Collaboration et al. 2020). These measurements suggest relatively late reionization compared to previous measurements by the Planck (Planck Collaboration et al. 2016) and WMAP (Bennett et al. 2013) missions.

Additional information regarding the morphology and timing of reionization can be obtained through the kinetic Sunyaev-Zeldovich (kSZ) effect (Sunyaev & Zeldovich 1980; J. P. Ostriker & Vishniac 1986). This phenomenon occurs when the electrons with a bulk motion relative to the CMB rest frame scatter the CMB photons, producing a Doppler shift in the scattered photons. The kSZ signal comprises two components, the homogeneous and patchy kSZ signal. The homogeneous signal arises due to spatial inhomogeneities in the baryonic density in the fully ionized Universe, while the patchy signal arises due to fluctuations in the ionization fraction during EoR. Several studies suggest that the patchy kSZ signal can be used not only to infer the mid-point and the duration of reionization but also to study the sources driving the process (for example, Nikolić et al. 2023; Jain et al. 2024).

1.3.2 The Lyα forest

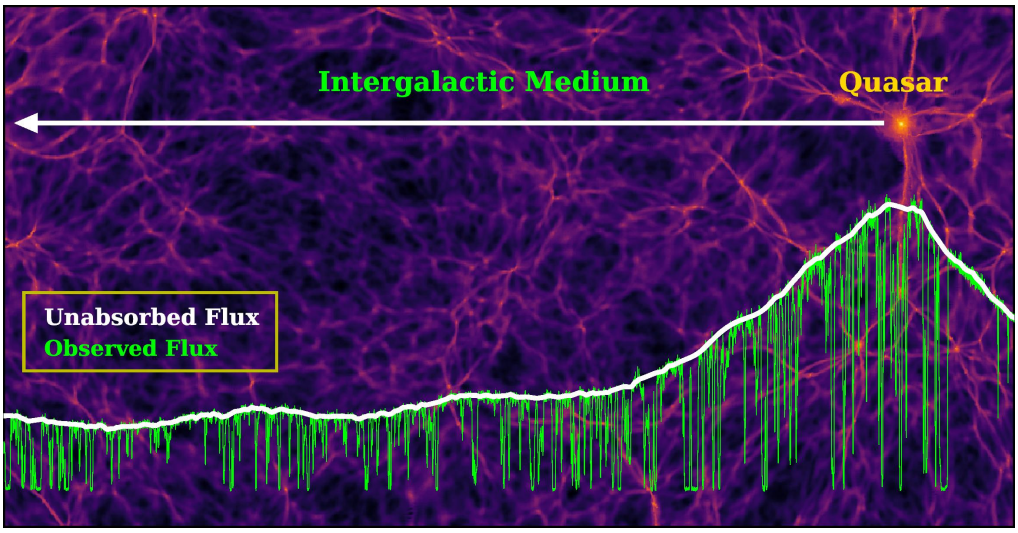


Figure 1.3: Schematic illustration of the Lyα forest. The bright source on top right corner represents a quasar whose intrinsic spectrum is shown in solid white curve. The Lyα absorption features are represented in the green lines. Image credit: Kavli Institute for Cosmology, Cambridge (KICC)

[1]The mid-point of reionization $z_{\rm mid}$ is defined as the redshift at which roughly half of the neutral hydrogen in the Universe is ionized.

The Lyα forest refers to a series of Lyα absorption lines in the intrinsic quasar spectrum, observed blueward of the rest frame wavelength of the Lyα emission line ($\lambda_{\rm Ly\alpha} \approx 1216$ Å). This line is associated with the transition of electron from 1s $\rightarrow$2p state in a neutral hydrogen. The reason for observing these series of lines is as follows. Suppose that photons from a distant quasar are traveling towards us. As the Universe expands the wavelength of the photons also increases along its way. Photons emitted with a wavelength shorter than Lyα wavelength ($\lambda_{\rm Ly\alpha} \approx 1216$ Å) will eventually get redshifted to the Lyα transition line. If this occurs in a region where there is substantial presence of neutral hydrogen, the photon will excite the electron from 1s $\rightarrow$2p state. During de-excitation of the electron the remitted photon is scattered in random directions. If the direction of the scattered photon is not along our line of sight, we observe an absorption feature in the intrinsic spectrum. The presence of multiple regions of neutral hydrogen at different redshifts produces a series of Lyα absorption lines, which we call the Lyα forest. The observable from a quasar spectrum in the transmitted flux is represented as $F(z) = e^{-\tau}$, where

$$\tau = \int \frac{c}{H(z)}\, \sigma_\alpha\, x_{\rm HI}\, {\rm n_H}\ \ (1+z)^3\, dz \tag{1.2}$$

is the Lyα optical depth. In the above equation, c is the speed of light, $H(z)$ is the Hubble parameter, σ_α is the Lyα absorption cross-section, $x_{\rm HI}$ is the fraction of neutral hydrogen, $\rm n_H$ is the number density of hydrogen, and z is the redshift.

The optical depth scales as $\tau_\alpha \propto f_{\rm HI}(1+z)^3$, making it very sensitive to even small amounts of neutral hydrogen. For example, a neutral hydrogen fraction of $x_{\rm HI} \sim\ 10^{-4}$, causes almost complete absorption of flux which makes $F(z) \rightarrow 0$. If access neutral hydrogen in present in the IGM then we observe a sharp drop in the transmitted flux across the Lyα emission line. This effect is known as the Gunn-Peterson effect (Gunn & Peterson 1965). At redshifts $\gtrsim 5$, we observe almost complete absorption of the transmitted Lyα flux blueward of the Lyα emission line, which is known as the Gunn-Peterson trough (Fan et al. 2001; Fan et al. 2006; G. D. Becker et al. 2015b). At redshifts $\lesssim 5$, the absence of the Gunn-Perterson trough in the observed Lyα flux suggests that the neutral hydrogen in IGM has mostly been ionized at these redshifts (references). This makes the Lyα forest a powerful probe to study the IGM at the end stages of hydrogen reionizaton.

Spectroscopic observations of quasars between $5 \lesssim z \lesssim 6$, show variation in the mean transmitted flux across different sight lines (references). These fluctuations were larger than those suggested by models with a uniform ionizing background and power law temperature-density relation. Following this, a number of other models were proposed to explain the fluctuations. For example, temperature fluctuations induced from inhomogeneous reionization (D'Aloisio et al. 2015), fluctuations in the background photoionization rate (Davies & Furlanetto 2016) and density distribution (Chardin et al. 2017), and a delayed end in reionization at $z \approx 5$ (Kulkarni et al. 2019; Nasir & D'Aloisio 2019).

A nearly model independent method was introduced by McGreer et al. 2011 that uses the fraction of "dark pixels" (pixels that show almost complete absorption in the Lyα forest) to estimate neutral hydrogen fraction ($x_{\rm HI}$) towards the

end of hydrogen reionization. This method gives an upper bound of $x_{\rm HI}$, as the residual neutral hydrogen in the ionized regions can also saturate the Lyα forest. The measured values of $x_{\rm HI}$ is $\lesssim 0.2$ at $z \lesssim 5.5$ which increases to $x_{\rm HI} < 0.8$ at $z = 6.1$. Subsequent measurements were performed using this method by McGreer et al. 2015 and Jin et al. 2023. The latest measurements by Davies et al. 2026 place an upper limit on the volume average neutral hydrogen fraction of $\langle x_{\rm HI} \rangle \leq \{0.030{+}0.048,\ 0.095{+}0.037,\ 0.191{+}0.056,\ 0.199{+}0.087\}$ at $\bar{z} = \{5.481,\ 5.654,\ 5.831,\ 6.043\}$

Another method is the study of "transmission spikes" that are observed in the spectrum of high redshift quasars. These spikes occur because of the presence of small highly ionized regions (Gnedin et al. 2017; Chardin et al. 2018; Garaldi et al. 2019; Nasir & D'Aloisio 2019) within largely neutral regions due to inhomogeneous reionization (G. D. Becker et al. 2015a; Bosman et al. 2018; Eilers et al. 2018). Studies have shown that the height and number of spikes are sensitive to the neutral fraction $x_{\rm HI}$, which is further dependent on the photo-ionization rate and the temperature of the gas in the ionized regions (for example, Gaikwad et al. 2020).

The reionization process also affects the temperature of IGM and hence the Lyα forest has also been used to measure the thermal parameters of the IGM at different redshifts (Schaye et al. 1999; Schaye et al. 2000; Theuns et al. 2000; Theuns et al. 2002b; McDonald 2003; Kim et al. 2004; Lidz et al. 2010; Garzilli et al. 2012; Bolton et al. 2014; Boera et al. 2014; Hiss et al. 2018; Telikova et al. 2019; Walther et al. 2019; Boera et al. 2019; Gaikwad et al. 2020; Gaikwad et al. 2021). Moreover, combined with simulations, the transmitted Lyα flux has also been used to estimate the HI photoionization rate $\Gamma_{\rm HI}$ (Rauch et al. 1997; Bolton & Haehnelt 2007; Faucher-Giguère et al. 2008; Calverley et al. 2011; G. D. Becker & Bolton 2013; Gaikwad et al. 2017a; Gaikwad et al. 2017b; Khaire & Srianand 2019; Gaikwad et al. 2023)

1.3.3 HI 21 cm emission

The HI 21 cm signal originates when the proton and electron in a neutral hydrogen atom makes a spin transition between the triplet (parallel) and singlet (anti parallel) states. This transition produces radiation at a rest frame wavelength of 21 cm (frequency, ν = 1420 MHz). Since the early Universe was filled with neutral hydrogen and its fraction evolves as reionization progresses, the 21 cm signal will serve as a probe to study different stages of reionization and structure formation. As this signal reaches us from the early Universe, it gets redshifted and falls in the radio regime and provides a direct probe of the neutral hydrogen distribution during reionization (Field 1958). Compared to other probes such as the CMB and the Lyα forest, which provide integrated or line-of-sight information, the 21-cm signal has the potential to map the IGM in three dimensions, offering a direct view of its spatial structure and evolution.

The key observable of this probe is the differential temperature brightness, defined as the contrast between the 21-cm brightness temperature and the background CMB radiation, along a given line of sight. The contrast is observed because the 21-cm signal is absorbed as well as emitted in the field of neutral hydrogen, while the CMB radiation acts as an uniform radiation field. The ob-

served signal therefore depends on whether the hydrogen spin temperature T_s is higher than the CMB temperature $T_{\rm CMB}$. If $T_s = T_{\rm CMb}$ we have thermal equilibrium. However, if $T_s \neq T_{\rm CMB}$ a contrast is developed. For the later case, if $T_s < T_{\rm CMB}$ hydrogen absorbs CMB photons producing an absorption signal, and for $T_s > T_{\rm CMB}$ the gas emits excess radiation producing an emission signal. Hence, the differential brightness temperature $\delta T_b(\nu)$ observed at a frequency $\nu_{\rm obs}$ along a line of sight $\hat{n}$ relative to the CMB can be expressed as,

$$\begin{aligned}\delta T_b(\nu) \approx 27\,{\rm mK}\; & x_{\rm HI}(\mathbf{x},z)\,[1+\delta(\mathbf{x},z)] \\ & \times \left(1-\frac{T_{\rm CMB}(z)}{T_S(\mathbf{x},z)}\right)\left(1+\frac{1}{H(z)}\frac{dv_p}{dr}\right)^{-1} \\ & \times \left(\frac{1+z}{10}\right)^{1/2}\left(\frac{Y_{\rm H}}{0.76}\right)\left(\frac{0.14}{\Omega_m h^2}\right)^{1/2}\left(\frac{\Omega_b h^2}{0.022}\right) \end{aligned} \tag{1.3}$$

In this expression, $\mathbf{x}$ is the comoving distance along the line of sight, $x_{\rm HI}$ is the neutral hydrogen fraction, δ represents the density contrast and $H(z)$ is the Hubble parameter. The quantity $\frac{dv_p}{dr}$ represents the gradient of the proper velocity along the line of sight. The spin temperature of neutral hydrogen in the IGM is denoted by T_S, while $T_{\rm CMB}(z) = 2.73\,(1+z)\,{\rm K}$ corresponds to the CMB brightness temperature at redshift z. The terms $Y_{\rm H}$, $\Omega_{\rm m}$, Ω_b, represents the hydrogen fraction in the Universe, matter density parameter, and the baryon density parameter, respectively.

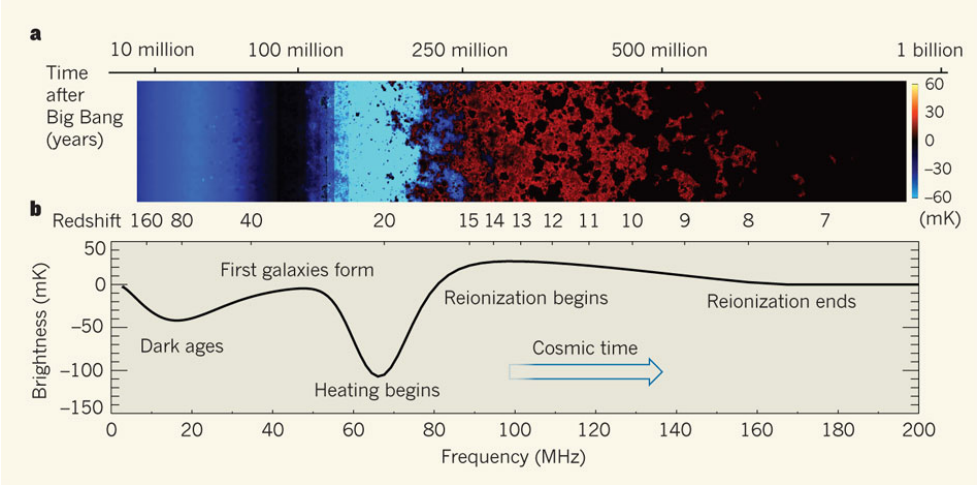


Figure 1.4: Figure shows the evolution of brightness temperature of the 21 cm signal relative to CMB temperature. The upper panel shows the slice from simulation of the evolution in the spatial fluctuations in the 21 cm brightness temperature. The lower panel shows the sky-average global 21 cm signal. Image credits: Pritchard & Abraham Loeb 2012.

There are two main observational techniques for detecting the cosmological 21 cm signal from the Epoch of Reionization. (i) Global 21 cm signal, which involves measuring the average intensity of 21 cm radiation across the entire sky as a function of frequency (Bowman et al. 2018; Singh et al. 2018; de Lera Acedo et al. 2022), (ii) Intensity mapping, which involves detection of variations in the intensity of 21 cm radiation over a large region of the sky. The later method aims to generate 3D maps of the 21 cm signal coming from the IGM during EoR using statistical tools like power spectrum or bispectrum (Gehlot et al. 2019; Mertens et al. 2020). The main in detecting the 21 cm line is that the cosmological signal is that it is embedded with astrophysical foreground signal arising from galactic and extra-galactic synchrotron and free-free emissions. Several different techniques have been proposed to remove or avoid these foregrounds and extract the underlying signal (for example, Liu et al. 2009; Petrovic & Oh 2011; Bonaldi 2018; Makinen et al. 2021).

At present a number of interferometric telescope are working on measuring the power spectrum of the 21 cm signal, for example, Low Frequency Array (LOFAR) (Gehlot et al. 2019; Mertens et al. 2020) Murchison Widefield Array (MWA) (Barry et al. 2019; Trott et al. 2020), Precision Array for Probing the Epoch of Reionization (PAPER) (Parsons et al. 2010; Abdurashidova et al. 2022) and Hydrogen Epoch of Reionization Array (HERA) (Kolopanis et al. 2019), are focused on detecting the power spectrum of 21 cm fluctuations. In addition, there are experiments that aim to measure the global 21 cm signal over a broad range spanning both Epoch of Reionizaiton and Cosmic Dawn, including Shaped Antenna measurement of the background Radio Spectrum (SARAS) (Singh et al. 2018), Experiment to Detect the Global EoR Signature (EDGES) (Bowman et al. 2018), and Radio Experiment for the Analysis of Cosmic Hydrogen (REACH) (de Lera Acedo et al. 2022). With its exceptionally high resolution and sensitivity, the forthcoming Square Kilometer Array (SKA) telescope (Koopmans et al. 2015) will probably transform 21 cm cosmology by giving us a thorough 3D tomographic image of the IGM during reionization

1.4 Research Objectives

The Epoch of Reionization mainly affects the ionization state and the thermal state of the IGM. Several studies have shown that the reionization process was extended and inhomogeneous in nature. The overdense regions in the IGM collapsed first, forming stars and galaxies and ionizing the surrounding neutral regions. However, less dense regions remained neutral till longer periods. Thus, different regions were ionized at different times, depending on their proximity to the ionizing sources. As a result, the early ionized regions started to cool first and attained a lower temperature, while the late ionized regions had a comparatively higher temperature, producing temperature fluctuations during the end stages and shortly after hydrogen reionization. The focus of this thesis is to investigate the temperature fluctuations that persist in the IGM shortly after hydrogen reionization.

We use the Lyα forest as a probe to detect and measure temperature fluctuations in the IGM. Synthetic Lyα forest are generated in the redshift range

$4 \leq z \leq 5$ for different reionization models that have controlled temperature fluctuations. The temperature of the gas affects the amplitude, width, and small-scale structures of the absorption features. Therefore, we aim to study how these absorption features change in different temperature fluctuation models. We also investigate the impact of temperature fluctuations on the Lyα statistics across different velocity scales. This analysis will be used to distinguish between different reionization models. Detecting and characterizing these temperature fluctuations would be a signature of inhomogeneous reionization. It would also help us better understand the nature of ionizing sources. In addition, it can place tighter constraints on the morphology and timing of the reionization process.

1.5 Outline

This thesis is organized as follows. In Chapter 2, we introduce the theoretical framework. We discuss concepts such as the reionization equation of the IGM, photoionization equilibrium and photoheating, We also discuss the thermal evolution and temperature density relation of the IGM. Chapter 3 focuses on the simulations used in this work. We describe the cosmological hydrodynamical simulation and the radiative transfer codes. We describe the parameters that are varied to produce different reionization histories and temperature fluctuation models. In Chapter 4, we present our methodology. We first explain how the synthetic Lyα forest spectrum is generated incorporating temperature fluctuations in the IGM. We then discuss the effects of temperature on the Lyα absorption features. Finally, we introduce the Lyα statistics used in this work, including the 1D flux power spectrum and wavelet statistics, which are used to probe IGM temperature fluctuations induced by different models. Chapter 5 presents the results of our analysis. In Chapter 6, we summarize the main findings of this thesis and discuss the possible directions for our future work.

CHAPTER 2

Physics of the intergalactic medium

2.1 Heating of the IGM

During the epoch of reionization, the neutral gas in the IGM experiences gradual heating due to the ionization fronts (*I-fronts*) that expand radially outward from the ionizing sources. The *I-fronts* are like a boundary that separates the neutral and the ionized content in the IGM, where the gas falling within the boundaries of the *I-fronts* is partially ionized while that outside is still neutral. In addition to the ionizing photons, the shocks generated by the gravitational collapse of overdense regions also contribute to the heating of the IGM gas. The combined effect of heating from *I-fronts* and shocks leads to a rise in the temperature of the gas in the IGM. We next briefly discuss photoionization heating and shock heating.

2.1.1 Photoionization heating

As discussed earlier, radiation from the first star-forming galaxies and quasars ionizes the neutral gas in the intergalactic medium (IGM) through photoionization. When a photon with an energy greater than 13.6 eV interacts with a neutral hydrogen atom, it ejects an electron, and the excess photon energy is converted into the kinetic energy of that electron. As many electrons are produced by ionization, the cumulative kinetic energy of electrons heats the IGM to higher temperatures. If photoionization is the only heating process, the total heating rate $\mathscr{H}$ (H. Mo et al. 2010; Gaikwad et al. 2019) is given as

$$\mathscr{H} = \mathrm{n_{H_I}}\, \varepsilon_{\mathrm{H_I}} + \mathrm{n_{He_I}}\, \varepsilon_{\mathrm{He_I}} + \mathrm{n_{He_{II}}}\, \varepsilon_{\mathrm{He_{II}}} \tag{2.1}$$

with

$$\varepsilon_i = \int_{\nu_i}^{\infty} \frac{4\pi J(\nu)}{h_{\mathrm{P}}\nu}\, \sigma_i(\nu) h_{\mathrm{P}}(\nu - \nu_i) d\nu, \tag{2.2}$$

where $\mathrm{n_{HI}}$, $\mathrm{n_{HeI}}$, $\mathrm{n_{HeII}}$ represents the number density of neutral hydrogen, neutral helium, and singly ionized helium, respectively. ν_i is the frequency of the ionization threshold of species i, $\sigma_i(\nu)$ is the photoionization cross-section, $J(\nu)$ is the intensity of the background UV radiation field, and h_{P} is Planck's constant. Heating due to ionizing photons typically raises the IGM temperature to a few 10^4 K. If additional heating sources raise the temperature above 10^4 K

at $z > z_{\rm comp}$ ($z_{\rm comp} \sim 6$)[1] (H. Mo et al. 2010), Compton cooling dominates and reduces the temperature to approximately 3×10^4 K (H. Mo et al. 2010). Thereafter, the temperature gradually decreases because of cosmic expansion. However, if heating occurs later ($z < z_{\rm comp}$), the Hubble expansion becomes the main cooling mechanism, where the IGM remains at a higher temperature above 10^4 K.

2.1.2 Shock Heating

Apart from photoionization, the IGM can also be heated by shocks produce due to the gravitatinal collapse of overdense regions. During structure formation, collapsing density perturbations heat the gas to the virial temperature of the forming structures. The collapse of the overdense regions proceeds aspherically, first forming sheets, then filaments, and finally virialized halos. This leads to shock heating of the gas with temperatures $10^5 \lesssim T \lesssim 10^6$ K (H. J. Mo et al. 2005). For example, D'Aloisio et al. 2019 in Figure 9 compares the temperature fluctuation fields produced by his model, which does not incorporate shock heating, with full RadHydro simulations. The simulations with full RadHydro produces filaments that have very high temperature because of shock heating, which is not observed in his model. At $z \gtrsim 2$, the shock heated gas can cool in Hubble time, but at $z \gtrsim 2$ the cooling time exceeds the Hubble time, resulting in a net heating of the IGM. Hydrodynamical simulations that include the effect of shock heating show that at $z \sim 2$, around 30 - 40 % of IGM is heated up to temperatures $T \sim 10^5 - 10^7$ K. Such regions are referred to as warm hot intergalactic medium (WHIM), that are distributed in the filaments and sheets (Cen & Jeremiah P. Ostriker 1999; Davé et al. 2001).

2.2 Physics of reionization

In this section, we describe the equations that are involved in the reionization process. This includes the reionization equation, the temperature evolution equation of the IGM, and the photoionization equilibrium equations.

While the reionization process is going on, to track the evolution of the volume filling factors of ionized hydrogen $Q_{\rm HII}$ as a function of cosmic time, the reionization equation Madau et al. 1999; Haardt & Madau 2012; Madau & Fragos 2017 is used, which is given as

$$\frac{dQ_{\rm H_II}}{dt} = \frac{\dot{n}_{\rm ion}}{\langle n_H \rangle} - \frac{Q_{\rm H_II}}{\langle t_{\rm rec} \rangle}, \tag{2.3}$$

where, the first term on the RHS represents the number of ionizing photons emitted per hydrogen atom by all radiation sources that were present at earlier times. The second term represents the number of radiative recombinations per ionized hydrogen atom. In the above equation, $\langle n_{\rm H} \rangle$ is the average number density of hydrogen, $\langle t_{\rm rec} \rangle$ is the volume averaged hydrogen recombination time scale. The term $\dot{n}$ is the rate of production of ionizing photons, expressed as

[1] The cooling time period against CMB photons is approximated as $\frac{t_{\rm CMB}}{t} \approx 350\, \Omega_{m,0}^{1/2}\, h\, (1+z)^{5/2}$. The ratio $\frac{t_{\rm CMB}}{t} \to 1$ for $z = z_{\rm comp} \sim 6$, considering $h = 0.7$ and $\Omega_{m,0} = 0.3$.

$$\dot{n}_{\rm ion}(t) = \int_{\nu_L}^{\infty} \frac{\langle f_{\rm esc} \rangle}{h\nu}\, \epsilon_\nu(t)\, d\nu \tag{2.4}$$

where $\langle f_{\rm esc} \rangle$ is the escape fraction of the ionizing photons, ν is the frequency of the photon, ϵ_ν is the emissivity of the ionizing source as a function of time, and h is Planck's constant.

The Eq. 2.3 assumes that the mean free path of the ionizing photons is much smaller than the horizon scale. This means that the photons will be absorbed before getting redshifted below the ionization edge. In case where the ionizing source is a quasars, the source term includes only those photons that are above the Lyα limit (wavelength ~ 912 Å and that escape into the IGM. In case of quasars $f_{\rm esc} = 1$. In the very early stages of reionization, when the ionization fronts from individual ionizing sources have just begun to propagate in the IGM, the factor $Q_{\rm HII} \ll 1$. This is known as the "pre-overlap" phase, in which the ionizing bubbles produced by the sources in the neighborhood have not yet overlapped. As the ionization process progresses, the bubbles start to overlap and the value of the hydrogen filling factor increases. Finally, when $Q_{\rm HII} = 1$, it indicates the end of the reionization process. All regions with low density become highly ionized.

The reionization process causes the gas to heat up. The modeling of temperature (T) of the gas in the IGM is performed using thermal evolution equation (Hui & Gnedin 1997; Upton Sanderbeck et al. 2016; Gaikwad et al. 2017a; Gaikwad et al. 2018; Gaikwad et al. 2019) given as,

$$\frac{dT}{dt} = -2HT + \frac{2T}{3\Delta}\frac{d\Delta}{dt} + \frac{dT_{\rm shock}}{dt} - \frac{T}{n_{tot}}\frac{dn_{tot}}{dt} + \frac{2}{3k_B n_{tot}}\frac{dQ}{dt}, \tag{2.5}$$

where H is the Hubble parameter, Δ is the density in terms of the mean baryon density ($\Delta = \frac{\rho_b}{\bar{\rho}_b}$), n_{tot} is the total baryon number density, $T_{\rm shock}$ is the shock temperature, Q represents the net heat exchange and k_B is the Boltzmann constant. The first five terms in the RHS account for adiabatic cooling due to Hubble expansion, adiabatic evolution of overdensities, shock heating due to structure formation, change in the internal energy, and photoheating and other cooling processes including inverse Compton cooling, Bremsstrahlung, collisional excitation, collisional ionization, recombination, and dielectric cooling. In order to solve the last two terms in Eq. 2.5, we further have to solve a set of photoionization equations Madau & Fragos 2017 given as

$$\begin{aligned}
\alpha_{\rm HII}\, n_e\, f_{\rm HII} - f_{\rm HI}\, (\Gamma^{\gamma}_{\rm HI} + \Gamma^{e}_{\rm HI}) &= \frac{df_{\rm HI}}{dt}, \\
\alpha_{\rm HeII}\, n_e\, f_{\rm HeII} - f_{\rm HeI}\, (\Gamma^{\gamma}_{\rm HeI} + \Gamma^{e}_{\rm HeI}) &= \frac{df_{\rm HeI}}{dt}, \\
-\alpha_{\rm HeIII}\, n_e\, f_{\rm HeIII} + f_{\rm HeII}\, (\Gamma^{\gamma}_{\rm HeII} + \Gamma^{e}_{\rm HeII}) &= \frac{df_{\rm HeIII}}{dt}.
\end{aligned} \tag{2.6}$$

In the above set of equations, $\Gamma^{\gamma}_{X_i}$ is the photoionization rate, $\Gamma^{e}_{X_i}$ is the collisional ionization rate, $\alpha_{\rm x_i}(T)$ is the recombination rate, $f_{\rm x_i}$ is fraction of the element $\rm x_i$, and n_e is the number density of free electrons. The set of equations in 2.6 satisfies the condition

$$
\begin{aligned}
f_{\rm HI} \; + \; f_{\rm HII} &= 1, \\
f_{\rm HI} \; + \; f_{\rm HeII} \; + \; f_{\rm HeIII} &= y, \\
f_{\rm HI} \; + \; f_{\rm HeII} \; + \; f_{\rm HeIII} &= f_e,
\end{aligned}
\tag{2.7}
$$

where $y = \mathrm{Y_{He}} \frac{\mathrm{m_H}}{\mathrm{m_{He}\ (1-Y_{He})}}$ is the abundance of He by number, $\mathrm{m_H}$, and $\mathrm{m_{He}}$ are the atomic masses of hydrogen and helium, f_e is the fraction of free electrons, and $\mathrm{Y_{He}}$ is the fractional abundance of helium by mass.

2.3 IGM temperature density relation (TDR)

Describing the thermal state of the IGM using a single temperature is a very challenging task. Several studies in the past have shown that there is a strong correlation between temperature and density because of the balance between processes of adiabatic heating and cooling, adiabatic compression and expansion, and photoheating and cooling (Hui & Gnedin 1997; Theuns et al. 1998; Valageas et al. 2002).

Solving Eq. 2.5 for a low density IGM ($\Delta \lesssim 10$), considering a homogeneous reionization scenario, i.e., all regions in the IGM are ionized simultaneously, gives a power-law temperature-density relation (TDR) (Hui & Gnedin 1997)

$$
T = T_{\rm o}\ \Delta^{\gamma-1},
\tag{2.8}
$$

where $T_{\rm o}$ is the IGM temperature at the mean cosmic density ($\Delta = 1$) and γ is the slope of the TDR. Using simulations the temperature density relation for IGM has been studied for both the equilibrium and the non-equilibrium cases (Puchwein et al. 2015; Puchwein et al. 2019; Gaikwad et al. 2019; Gaikwad et al. 2023). For calculating $T_{\rm o}$ and γ from the simulation at a given redshift z, we follow the procedure given in Gaikwad et al. 2019, described below.

- Compute $\log(T)$ and $\log(\Delta)$ using the extracted fields T and Δ from the simulation at a given redshift, z.
- Divide $\log(\Delta)$ into bins with centers $-0.375,\ -0.125,\ 0.125,$ and 0.375 and a bin width 0.25, and assign $\log(T)$ to the bins, respectively. The choice of bin center is motivated by the fact that the TDR deviates from the power-law below $\log(\Delta) \leq -0.5$ for inhomogeneous reionization. (Refer to Figure 3 from Gaikwad et al. 2019)
- Calculate the median temperature $\log(T)$ for all particles in each $\log(\Delta)$ bin.
- Obtain best-fit values for $T_{\rm o}$ and γ by fitting a linear fit to the relation $\log(T) = \log(T_{\rm o}) + (\gamma - 1)\log(\Delta)$, using the median $\log(T)$ and $\log(\Delta)$ bin centers calculated in the previous steps.

Figure 2.1 compares the TDR of a cold (panel A) and a hot (panel B) IGM at $z = 5.8$. The models have a uniform photoionization background, producing homogeneous reionization. The hot and cold models are optically thin models

taken from the Sherwood-Relics simulation Puchwein et al. 2023. The color scheme in the plot shows the density of points. For $\log(\Delta)$ between -1 to 1, a large density of points are settled in a narrow region, showing a linear relation between $\log(T)$ and $\log(\Delta)$. For a optically thin IGM and given that $\Delta \lesssim \frac{1}{10}$, the temperature and the density of the gas follows TDR in Eq. 2.8. The dashed black line represents the best-fit relation calculated using the procedure discussed above. The hot model has a higher T_0 and the slope of the TDR is flat. By construction hot model has more heating of the gas. Since a large fraction of cells are heated up to large temperature at the same time, this causes isothermal heating of the gas. The temperature becomes almost independent of the density, giving a flat slope to the TDR.

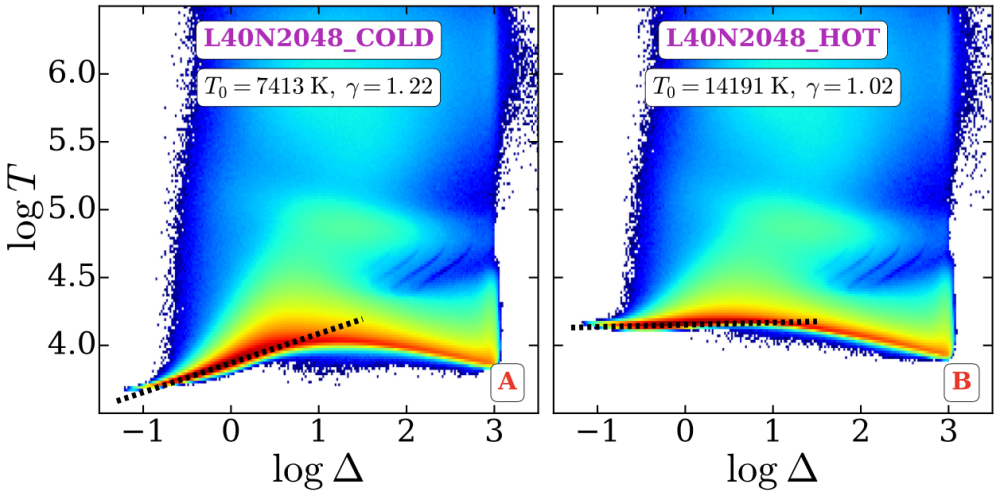


Figure 2.1: Comparison of the temperature density relation between cold (panel A) and hot (panel B) IGM at $z = 5.8$. In both the models the best fit obtained using the TDR relation from Eq. 2.8 is shown by dashed black line. The color scheme represents the density of particle from the simulation box. High heating makes the temperature almost independent of density, giving the hot model a flat slope with higher T_0. The values (T_0, γ) calculated for hot and cold model are (7413 K, 1.22) and (14191 K, 1.02), respectively. Figure credit: Gaikwad et al. 2020

CHAPTER 3

Simulation

The fact that we only have one realization of the Universe means that we are bound to have a limited number of observations. This creates difficulty in separating real physical effects from cosmic variations. In addition, the signals we observe may have a weak amplitude and can be affected by various noise sources, for example, instrumental effects, foreground contamination, thermal noise, etc. This poses challenges in analyzing the observed signals. Moreover, the parameters of interest may not be measured directly from the observables. Often, there is also degeneracy between two or more parameters, where their combinations can produce similar results. This makes interpretation of the data very challenging. Simulations help overcome these problems by allowing us to create controlled models of the Universe, where we know the underlying physics and can change parameters one at a time. They also allow us to generate synthetic data and then compare it with observations. In this way, simulations act as a bridge between theory and observation. This further helps to study the underlying physics and place constraints on cosmological and astrophysical parameters

3.1 Cosmological hydrodynamical simulation

The cosmological hydrodynamical simulations used in this work are based on the Sherwood simulation suite (Bolton et al. 2017). These are state-of-the-art simulations of the IGM. The simulation box volume vary from $10^3 - 160^3\ h^{-3}$ cMpc^3. The simulations are designed to address a wide range of problems. For example, the study of IGM during hydrogen reionization at $z \geq 6$, constraining the matter power spectrum with the Lyα forest at $z \simeq 4$, mapping the 3D structure of the IGM with quasars at $2 < z < 3$, and investigating the properties of the Lyα forest at $z < 1$. The Sherwood simulations are performed using the P-GADGET-3 code, which is an updated version of the GADGET-2 code (Springel 2005). In this code, the gas and dark matter are treated as particles. The dark matter particles are treated as collision free, and they interact only through gravity. Their evolution is performed using the N-body solvers implemented in the P-GADGET-3 code. The gas particles are treated as fluid, and their evolution is performed in a Lagrangian approach using a smoothed-particle hydrodynamics (SPH) scheme (Springel & Hernquist 2002). In SPH, each particle does not represent a point value; instead, they have a spread which is computed using a smoothing kernel. The kernel assigns weights to neighbouring particles depend-

ing on their distance. Nearby particles have more weight, and distant particles have less weight. The SPH method computes the fluid quantities, such as pressure and density, by smoothing over neighbouring particles. The evolution of the fluid element is done by solving the standard set of equations including the continuity equation, Euler equation, Poisson equation, and the equation of state. Each of the dark matter and gas particles has a mass, position, and velocity. The mass of both dark matter and gas particles is fixed. However, under the influence of gravity, cosmic expansion and pressure, the position, velocity, and density of a region of the simulation box may change over time.

The P-GADGET-3 code also has the facility to perform the radiative transfer. The code uses a spatially uniform ionizing background model (Haardt & Madau 2012) and solves the photoionization and photoheating of the hydrogen and helium gas. The gas here is considered to be optically thin and in ionization equilibrium. This is a good approximation for post-hydrogen reionization $z \lesssim 5$, when hydrogen is highly ionized and the mean free path of the ionizing photons is greater than the distance between ionizing sources (Worseck et al. 2014). The output of the Sherwood simulations includes fields of density (Δ), peculiar velocity ($v_{\rm pec}$), temperature (T), and neutral hydrogen fraction ($f_{\rm HI}$). It also provides dark matter halo catalogues. These fields are used to produce the Lyα forest.

3.2 Modelling of temperature fluctuations in the IGM

In this work, we are interested in studying the large-scale temperature fluctuations that are induced in the IGM because of inhomogeneous reionization. However, the radiative transfer performed in the Sherwood simulations assumes a spatially uniform ionizing background, homogeneous reionization model. Hence, we perform radiative transfer as a post-processing step to incorporate the effects of inhomogeneous reionization. To execute this, we use the EXtended reionization using Code for Ionization and Temperature Evolution (EX-CITE) (Gaikwad et al. 2023), which is an updated version of the CITE code (Gaikwad et al. 2019).

The temperature of the gas just after the passing of the *I-front* is referred to as the reionization temperature $T_{\rm reion}$. D'Aloisio et al. 2019 shows that $T_{\rm reion}$ depends on the velocity of the ionization fronts $v_{\rm IF}$ and on the spectral index α, of the background ionizing sources. As the reionization process progresses, the hot gas eventually cools by means of radiative cooling and Hubble expansion. By the time reionization process ends, we have variations in the temperature of the IGM gas at different regions. This is because of the difference in the redshift at which a certain region is ionized. The gas that is ionized earlier, for example at $z \sim 10$ would start to and achieve a lower temperature compared to the recently ionized gas at $z \sim 6$. The differences timing of ionization produces spatial temperature fluctuations in the IGM.

The modeling of temperature fluctuations in the IGM in case of inhomogeneous reionization is performed using the EX-CITE code. The code follows the same procedure discussed in D'Aloisio et al. 2019 to generate the IGM temperature fluctuations. First, we start by calculating $v_{\rm IF}$ at each pixel in the simulation box using the reionization redshift maps. These maps store the redshift at which

$f_{\rm HI}$ at each pixel falls below 50 % for the first time. (see Figure 5.2). To compute $v_{\rm IF}$ from these maps, we use the relation

$$v_{\rm IF}(\mathbf{x}) = \frac{a}{|\nabla z_{\rm reion}|}\frac{dz}{dt}\,\hat{n}, \tag{3.1}$$

where $\mathbf{x}$ is the comoving coordinate, a is the cosmological scale factor, and $\hat{n} = \frac{\nabla z_{\rm reion}}{|\nabla z_{\rm reion}|}$ is the unit vector normal to the I-front.

Next, to compute $T_{\rm reion}$, we use a fitting relation between $v_{\rm IF}$ and $T_{\rm reion}$ given as

$$\ln(T_{\rm reion}) = \sum_{n=0}^{4} C_n \left[\ln\left(\frac{v_{\rm IF}}{\rm km/s}\right)\right]^n \tag{3.2}$$

which is based on the assumption that the spectral index of the ionizing sources is $\lesssim 1.5$ (D'Aloisio et al. 2019). In the above equation C_0, C_1, C_2, C_3, and C_4 are 9.5432, -1.6441×10^{-2}, -9.8010×10^{-3}, 4.1664×10^{-3}, and -2.2710×10^{-4}, respectively. The $T_{\rm reion}$ determined using the above relation is accurate to within 2% over the range $v_{\rm IF} = 1\times10^4 - 7\times10^4$ km s^{-1}. Finally, we set $T_{\rm reion}$ obtained from Eq. 3.2 as an initial temperature in 2.5. We calculate the temperature at later times for each pixel in the simulation box.

3.3 Reionization Models

In this work, we consider three reionization histories, early, mid and late, characterized by their respective mid-point of reionization $z_{\rm mid}$. The midpoint of reionization $z_{\rm mid}$ is defined as the redshift at which the volume average of the neutral hydrogen fraction $f_{\rm HI}$ in the simulation box falls below 50 % for the first time. The values of $z_{\rm mid}$ are $\approx$ 8.35, 7.2 and 6.15 for the early, mid, and late models, respectively. We treat $z_{\rm mid}$ as a free parameter in our simulation. The choice of the specified values of $z_{\rm mid}$ comes from the constraints on the mid-point of reionization from CMB measurements (Planck Collaboration et al. 2020; Planck Collaboration et al. 2016), the quasar damping wing measurements (Greig et al. 2017; Bañados et al. 2018; Davies et al. 2018; Mason et al. 2018; Mason et al. 2019; Greig et al. 2019; Wang et al. 2020; Yang et al. 2020b) and the Lyα Forest (Fan et al. 2006; G. D. Becker & Bolton 2013; McGreer et al. 2015; Yang et al. 2020a; T. Roy Choudhury et al. 2021; Bosman et al. 2022; Zhu et al. 2022). Figure 3.1 shows the evolution of volume averaged $f_{\rm HI}$ in the simulation box for the early (dashed blue), mid (dashed green), and late (dashed red) models.

Cosmological hydrodynamical simulations are based on the Sherwood simulation suite that are performed using the P-GADGET-3 code (Springel 2005; Bolton et al. 2017). The simulations have a box size of 80 h^{-1}cMpc, with 2×2048^3 dark matter and gas particles. The size of the box size is selected such that it is able to capture large scale temperature fluctuations, while also preserving the fluctuations at the small-scales. The simulations follow a simple star-formation scheme, where particles with an overdensity of $\Delta > 1000$ and temperature $T < 10^5$ K are converted into collisionless star particles (Viel et al. 2004). The simulations do not incorporate galaxy formation processes such as

stellar and AGN feedback and metal enrichment. Although this limits realism, it allows one to fairly capture the properties of the intergalactic medium (IGM). In addition to $z_{\rm mid}$, we treat $T_{\rm reion}$ as the second free parameter in our simulation. For each of the early, mid, and late models, we vary $T_{\rm reion}$ from 5000 to 50,000 K in steps of 500 K. For this work, we produce a total of 273 (3×91) reionization models. The combination T_{reion} and z_{mid} produces different temperature fluctuations at the end of the reionization event. The simulation outputs are stored at $z = 12.6, 11.6, ..$ up to 4.0 in step of $\Delta z \approx 0.1$. As the main objective of this study is to investigate temperature fluctuations in the IGM post hydrogen reionization, we only deal with the simulation outputs between $4 \leq z \leq 5$. All of our simulations use a flat CDM cosmology with $\Omega_m = 0.308$, $\Omega_b = 0.0482$, $\Omega_\lambda = 0.692$, $h = 0.678$, $Y = 0.24$, $n_s = 0.961$, and $\sigma_8 = 0.829$ (Planck Collaboration et al. 2014). The symbols $'c'$ and $'p'$ are used in the prefix to represent the comoving and physical distances.

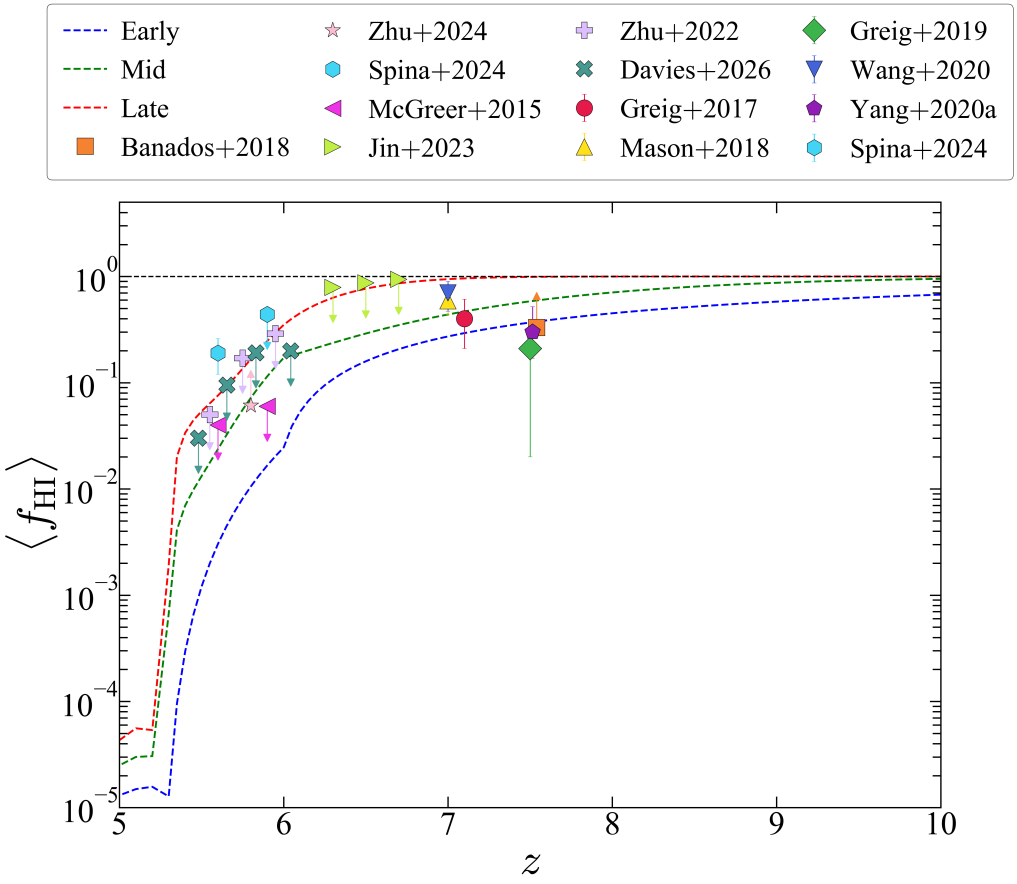


Figure 3.1: Figure shows the evolution of the volume-averaged neutral hydrogen fraction $\langle f_{\rm HI} \rangle$ for the early (dashed blue), mid (dashed green), and late (dashed red) models from redshift 10 to 4. The y-axis shows the neutral fraction in log-scale. The different markers represent the constraints on $f_{\rm HI}$ from measurements the Lyα forest (McGreer et al. 2015; Zhu et al. 2022; Jin et al. 2023; Davies et al. 2026; Spina et al. 2024; Zhu 2024) and damping wing analysis of QSO proximity regions (Greig et al. 2017; Bañados et al. 2018; Mason et al. 2018; Greig et al. 2019; Wang et al. 2020; Yang et al. 2020b)

CHAPTER 4

Method

4.1 Generating Lyα forest

The Lyα line is associated with the transition of an electron between states 1s and 2p in a neutral hydrogen atom. The wavelength of the photon associated with this transition is $\approx$ 1216 Å. Suppose that a bunch of photons with wavelength less than that of Lyα emission are traveling towards us. The wavelength of these photons will eventually get redshifted to the Lyα transition line due to the expansion of the Universe. If it occurs in a region with substantial neutral hydrogen, these photons will be absorbed and remitted. Due to scattering, some photons will deviate from our line of sight, which will cause a drop in the Lyα flux measured. The extinction of incoming radiation due to absorption or scattering is measured by optical depth, represented by the symbol τ. The optical depth for Lyα is mathematically expressed as

$$\tau(z_{abs}) = \frac{c^2 I_\alpha}{b\sqrt{\pi}} \int n_{HI} I_\alpha V(a,x) \frac{1}{H(z)(1+z)} dz, \tag{4.1}$$

where z_{abs} is the redshift where Lyα photon is being absorbed, $I_\alpha = 4.45 \times 10^{-18}$ cm^{-2}, is related to the Lyα absorption cross section, $b = \sqrt{\frac{2k_B T}{m_p}}$ km s^{-1} is the Doppler parameter, c is the speed of light, $H(z)$ is the Hubble parameter, n_{HI} (cm^{-3}) is the number density of neutral hydrogen, and $V(a,x)$ is the known as Voigt profile. The Voigt profile given in Eq. 4.4 is obtained by the convolution of a Lorentzian (see Eq. 4.2) with a Gaussian (see Eq. 4.3) profile.

$$\phi(\nu) \equiv \frac{1}{\pi} \frac{\gamma}{(\nu - \nu_\alpha)^2 + \gamma^2}, \tag{4.2}$$

where $\gamma = \frac{A_{21}}{\pi}$, and A_{21} is Einstein's coefficient for transition between states 2 to 1.

$$P(v)\, dv = \frac{1}{\pi^{1/2} b} \exp\left(-\frac{v^2}{b^2}\right) dv, \tag{4.3}$$

The Voigt profile is expressed below

$$V(a,x) = \frac{a}{\pi} \int_{-\infty}^{\infty} \frac{\exp\left(-y^2\right)\, dy}{(x-y)^2 + a^2}, \tag{4.4}$$

$$a \equiv \frac{c}{\Gamma_\alpha}\frac{\nu_\alpha}{4\pi b}, \qquad x \equiv \frac{c}{b}\frac{\nu-\nu_\alpha}{\nu_\alpha}, \qquad y \equiv \frac{v_{pec}}{b}, \tag{4.5}$$

where x is the Doppler shift in the frequency component due to the peculiar motion of the gas along the line of sight , ν_α is the frequency of the radiation associated with the Lyman alpha transition, Γ_α is the mean lifetime of the Lyman alpha transition and a quantifies the relative strength between damping and thermal broadening.

In Eq. 4.4 the Lorentzian profile is associated with the natural broadening of the Lyα transition line. This phenomenon occurs because of the finite lifetime of an electron in an excited state. Hence, the energy associated with a transition cannot be exact, as governed by the Heisenberg principle. Therefore, we observe a natural broadening associated with any emission or absorption line. The Gaussian profile arises due to the thermal motion of the gas. Atoms in a gas will have random velocities because of their temperature. These velocities follow a Maxwell–Boltzmann distribution. This distribution has a Gaussian component that depends on the temperature of the gas. The thermal velocity distribution, which is characterized by the Doppler parameter b. In addition to thermal velocity the gas element also has a peculiar velocity. Along our line of sight some gas element would be traveling towards us and some way from us. This causes a shift in the observed frequency of the radiation emitted by the gas atoms. The Doppler shift in the frequency of the incoming radiation given as $\nu_{\rm obs} - \nu_{\rm abs} = -\frac{v}{c}\nu_{\rm abs}$, where $\nu_{\rm obs}$ and $\nu_{\rm abs}$ are the frequencies received by the observer and during absorption, respectively.

To obtain $\rm n_{HI}$ field mentioned in Eq. 4.4, we first by calculating neutral hydrogen fraction $f_{\rm HI}$, using the photoinization equilibirum equation,

$$f_{\rm HI} = \frac{\mu_e\,\mu_p\,{\rm n_H}\,\alpha}{\Gamma_{\rm HI}}, \tag{4.6}$$

where $\mu_e = \frac{4}{4-3Y_{\rm He}}$ is the mean molecular weight per electron, $\mu_p = \frac{2}{2-Y_{\rm He}}$ is the mean molecular weight per proton, which are calculated considering the IGM gas to have fully ionized hydrogen and singly ionized helium atoms. $Y_{\rm He} \approx 0.24$ is the Helium mass fraction in baryonic matter. Here, $\rm n_H$ is the total hydrogen density ($\rm n_H = n_{HI} + n_{HII}$), α is the recombination rate, and $\Gamma_{\rm HI} \approx 10^{-12}$ s^{-1} is the HI photoionization rate. Due to uncertainty in the emissivity of the ionizing sources that participated in reionization, we vary $\Gamma_{\rm HI}$ to match with the mean flux in observations (G. D. Becker & Bolton 2013). Following reionization, the low density IGM achieves photionization equilibrium. Given this, varying photoionzation rate is a good approximation.

Next, we compute total hydrogen number density $\rm n_H$ expressed as

$$\begin{aligned} n_{\rm H} &= Y_{\rm H}\frac{\Omega_{\rm B}\rho_{\rm c}}{m_{\rm p}}\,\Delta\,(1+z)^3 \\ &\approx 1.9\times10^{-7}\,\Delta\,(1+z)^3, \end{aligned} \tag{4.7}$$

where, $Y_{\rm H} \approx 0.75$ is the hydrogen mass fraction, $\Omega_{\rm B}$ is the baryonic density parameter given as $\Omega_B = \frac{\rho_{\rm B}}{\rho_{\rm c}}$. The critical density $\rho_{\rm c}$ has an expression $\rho_{\rm c} = \frac{3H_o^2}{8\pi G}$. Solving the expression $Y_{\rm H}\frac{\Omega_{\rm B}\rho_{\rm c}}{m_{\rm p}}$ by substituting values $\rho_c = 1.88\times10^{-29}\,h^2$ cm^{-3}, $\Omega_{\rm B} = 0.048$, $\mu_{\rm B} = \frac{4}{4-3Y} = 1.22$, we get the value 1.9×10^{-7} cm^{-3}.

The number density of neutral hydrogen n_{HI} is obtained using expression,

$$\begin{aligned} n_{HI} &= n_H * f_{HI} \\ &= 1.9 \times 10^{-7}\, f_{HI}\, \Delta\, (1+z)^3 \end{aligned} \tag{4.8}$$

In the expression of f_{HI}, $a = 7.982 \times 10^{-11}$, $b = 0.7480$, $T_0 = 3.148$ K, and $T_1 = 7.036 \times 10^5$ K. The recombination rate (α) is expressed as

$$\alpha = a \left[\left(\frac{T}{T_0}\right)^{1/2} \left(1 + \left(\frac{T}{T_0}\right)^{(1-b)/2} \left(1 + \left(\frac{T}{T_1}\right)^{(1+b)/2}\right)\right)\right]^{-1} \tag{4.9}$$

and the values for T_0, T_1, a, and b are taken from Lukić et al. 2015.

To generate Lyα forest spectrum, the expression for Lyα optical depth in Eq. 4.1 is used. The temperature (T), overdensity (Δ), neutral hydrogen fraction (f_{HI}) and velocity (v) fields, were extracted by shooting random sight lines through the simulation box. For each reionization model (inhomogeneous and homogeneous), we generate Lyα optical depth for 1024 skewers. The transmitted transmitted Lyα flux is obtained using the simple relation $F(z) = e^{-\tau(z)}$. We produce the normalized Lyα forest in the range $4 \leq z \leq 5$. The effects of instrumental broadening, S/N, and metal line contamination are not added to the generated Lyα forest spectra.

Figure 4.1 shows the simulated Lyα optical depth and flux in the redshift range $4.0 \leq z \leq 4.4$ for T_o = 10,000 K and γ = 1.6.

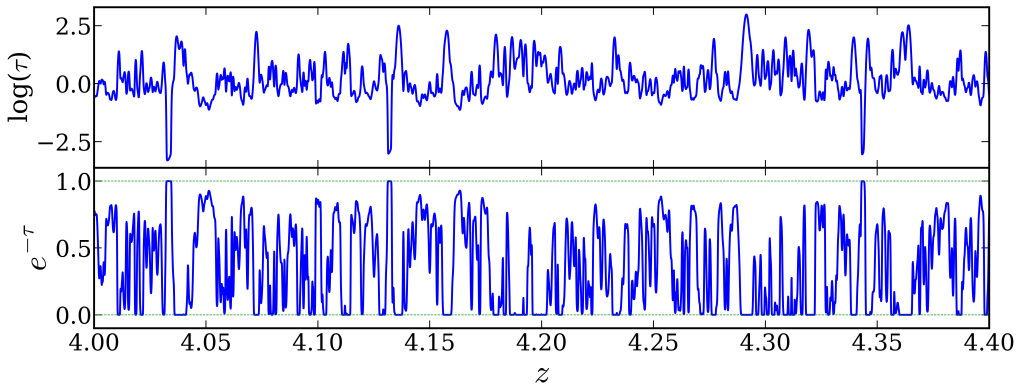


Figure 4.1: Sample of generated Lyα forest spectrum in the redshift range $4.0 \leq z \leq 4.4$ with a mean redshift of $\bar{z} = 4.2$. The upper panel shows the Lyα optical depth profile and the lower panel shows the corresponding normalized Lyα flux profile generated for T_o = 10,000 K and $\gamma = 1.6$.

4.2 Effects of temperature on Lyα absorption features

The heating of the IGM influences the Lyα absorption features in three primary ways. First, an increase in temperature enhances the thermal motion of the gas particles resulting in broadening of the absorption features (Schaye et al. 2000; Lidz et al. 2010; G. D. Becker et al. 2011).This is characterized by the Doppler

parameter, $b = \sqrt{\frac{2k_BT}{m_p}}$. Second, heating the gas increases the thermal pressure (Gnedin & Hui 1998; Peeples et al. 2010; Kulkarni et al. 2015; Lukić et al. 2015; Rorai et al. 2017; Maitra et al. 2019), which causes it to expand and smooth out small-scale density fluctuations. This is known as Jeans smoothing, which reduces the contrast in density fluctuations. The effects on the absorption features are that sharp features and fluctuations smooth out. The third effect is on the amount of neutral hydrogen (Rauch et al. 1997; Bolton & Haehnelt 2007; G. D. Becker & Bolton 2013; Khaire & Srianand 2019). A hot IGM will have a reduced recombination rate α, as it depends on the temperature as $\alpha \propto T^{-0.7}$, giving a smaller neutral hydrogen content. A higher temperature means fewer recombinations and a smaller fraction of neutral hydrogen. This results in reduced absorption producing shallow features. The combined effect of the three effects results in a flux spectrum with fewer fluctuations, broader and shallow absorption features.

Figure 4.2, shows the sensitivity of Lyα absorption features on temperature and neutral hydrogen. Instead of directly using these two parameters, the Doppler parameter b and neutral hydrogen column density N_{HI} are used. In the right panel, N_{HI} is fixed at 10^{13} cm^{-2}. The blue and the red profile are for $b = 1 \times 10^6$ and 2×10^6 cm s^{-1}, respectively. As discussed, on increasing temperature the features become broader and shallower. In the left panel b is fixed at 1×10^6 cm s^{-1}. The blue and red curves are for $N_{HI} = 10^{13}$ and 10^{18} cm^{-2}, respectively. On increasing N_{HI}, causes more absorption in the Lyα flux, eventually causing a wide spreading of the absorption profile, called as damping wing feature.

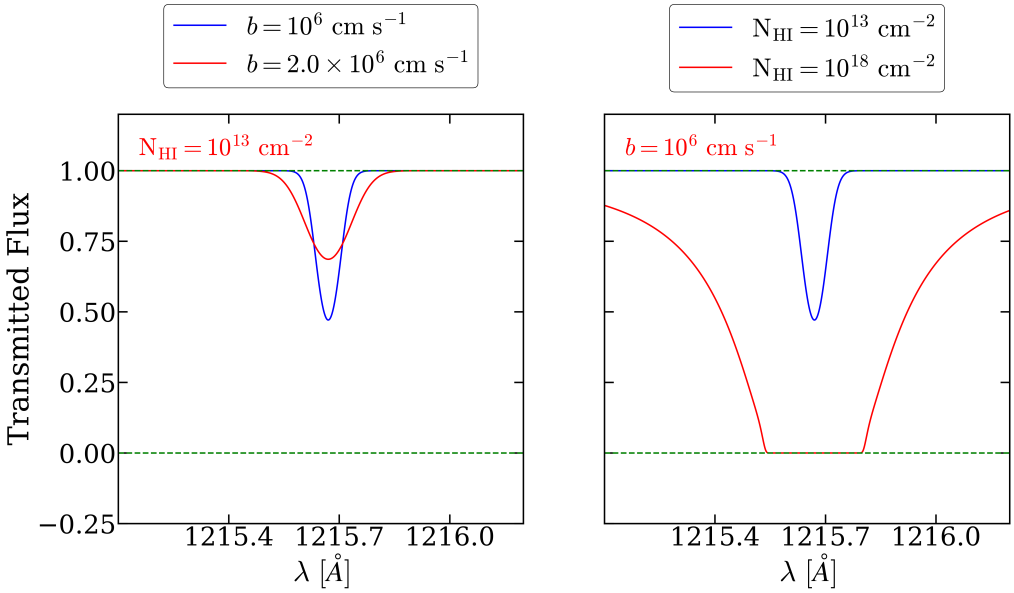


Figure 4.2: Figure illustrates the sensitivity of the Lyα absorption feature on the Doppler parameter (b) and neutral hydrogen column density (N_{HI}). In the right panel, N_{HI} is fixed at 10^{13} cm^{-2}. The blue and the red profile are for $b = 1 \times 10^6$ and 2×10^6 cm s^{-1}, respectively. In the left panel b is fixed at 1×10^6 cm s^{-1}. The blue and red curves are for $N_{HI} = 10^{13}$ and 10^{18} cm^{-2}, respectively.

4.3 Lyα Statistics

4.3.1 1D Flux Power Spectrum

The flux power spectrum is the variance of the flux contrast $\delta_F = \frac{F-\langle F\rangle}{\langle F\rangle}$ computed over each k mode in Fourier space. F is the transmitted flux of single spectrum and $\langle F\rangle$ is the average flux of all spectra. Flux power is mathematically expressed as

$$P_F(k) = \langle \delta_F(k)^\dagger \, \delta_F(k)\rangle = |\delta_F(k)|^2, \tag{4.10}$$

where $\delta_F(k)$ is the Fourier transform of $\delta_F(v)$ defined as

$$\delta_F(k) = \frac{1}{2\pi}\int_{-\infty}^{+\infty} \delta_F(v) e^{ikv} dv \tag{4.11}$$

Several studies have suggested that reionization process is extended and inhomogeneous in nature. Simulations performed by D'Aloisio et al. 2019 show that patchy reionization produces large scale temperature fluctuations. Several studies find that these temperature fluctuations will increase the power on large scales (Keating et al. 2018; D'Aloisio et al. 2019; Wu et al. 2019; Molaro et al. 2022). Hence, we study the effects of temperature fluctuations produced by different models on the shape power spectrum at different scales. Moreover, our analysis also focuses on detecting the large scale enhancement in the power as done by previous studies. The detection of the imprints of large scale temperature fluctuations on the power spectrum can provide valuable insights regarding the timing and morphology of the reionization process.

To compute the 1D flux power spectrum, we begin by taking the Fourier transform of the flux contrast $\delta_F(v) \rightarrow \delta_F(k)$ for each Lyα forest spectra, where v and k are related as $v = \frac{2\pi}{k}$. Here, v is the relative velocity due to Hubble expansion for an individual pixel along the line of sight in the Lyα forest with respect to the starting pixel. The velocity grid v is calculated using the relation $\Delta v = \frac{c}{1+z}\,\Delta z$. This relation can be easily derived by taking the first order time derivative of the relation $r = a(t)\chi$, and using the relation $\chi = \int \frac{c}{H(z)} dz$, where r and χ are the physical and co-moving separation between two objects, respectively. $H(z)$ is the Hubble parameter and $a(t)$ is the cosmological scale factor.

The quantity $\langle F\rangle$ is the mean flux, computed by taking the average of transmitted Lyα flux over 1024 skewers. When computing $\langle F\rangle$ we scale the optical depth (τ) so that $\langle F(z)\rangle$ matches the observations (G. D. Becker et al. 2013). For a single sight line the power $P_F(k)$ is obtained by taking the square of the modulus of $\delta_F(k)$, which is then divided into k_n number of logarithmic bins. The power computed for 1024 sight lines is divided into 64 groups. We calculate the mean power at every bin center represented as $k_{\rm cen}$. In this work, we take $k_{\rm cen}$ (km^{-1}s) ranging from 10^{-3} to 0.2 with a logarithmic bin spacing of $\Delta \log(k) = 0.1$ km^{-1}s. We do not go to higher k modes > 0.2 km^{-1} s, because the Lyα forest is more prone to noise at these scales, corresponding to a velocity separation between the absorption features $v \lesssim 30$ km s^{-1}. The error bars are obtained by taking the standard deviation of the mean powers for 64 groups.

To compute the power spectrum, we produce the normalized Lyα forest in redshift bins $z = 4.2,\ 4.4,$ and 4.6 with the bin width $\Delta z \approx 0.088$. The choice of specified redshift bins and bin width is motivated by the fact that that we want to compare the results of the power spectrum computed from our models with Molaro et al. 2022, where they calculate the power in the redshift bins $z = 4.2,\ 4.4,$ and 4.6 using transmitted Lyα flux extracted from the simulations with a box size of 40 $h^{-1}cMpc$, which corresponds to $\Delta z \approx 0.088$. We recommend the reader to refer to 5 for further details.

4.3.2 Wavelet statistics

The wavelet filter is a sinusoidal function damped by Gaussian. The filter is characterized by a wavelet filter scale $\mathrm{s_n}$ ($\mathrm{km\,s^{-1}}$). This is the velocity scale of interest to probe fluctuations in the Lyα absorption spectrum, in a Fourier mode $\mathrm{k_o}$ that is related to $\mathrm{s_n}$ as $k_o = \frac{2\pi}{s_n}$. The filter is mathematical expressed as,

$$\Psi(x) = \mathrm{A\ exp(ik_o x)\ exp}\left[\frac{-\mathrm{x}^2}{2\mathrm{s}_\mathrm{n}^2}\right], \tag{4.12}$$

where A is the amplitude of the filter. Generally, A is treated as a normalization constant such that it satisfies the condition $\int_{-\infty}^{\infty} |\Psi|^2 dx = 1$.

The wavelet filter has been used in several works to extract the scales in the transmitted Lyα flux that are sensitive to a given combination of T_o and γ (Zaldarriaga 2002; Theuns et al. 2002a; Lidz et al. 2010; Garzilli et al. 2012; Gaikwad et al. 2021). The key feature of this filter is that it is localized both in real and in Fourier space, allowing one to use the wavelet to study fluctuations in the transmitted Lyα flux at a specific velocity scale with a corresponding Fourier mode. From Figure 5.13, we see that the difference in the power between the patchy models is present at scales, $s_n \lesssim 100\ \mathrm{km\,s^{-1}}$. Studying the transmitted Lyα flux at these scales using wavelet analysis would allow us to understand the nature of temperature fluctuations in different models.

Taking the convolution of the transmitted Lyα flux with the filter returns a complex quantity $\mathrm{a_n}$. The absolute value of $\mathrm{a_n}$ gives us the wavelet amplitude $\mathrm{A_n}$ given in Eq. 4.13. The n in the subscript defines the velocity scale of interest. This value is the standard deviation (s_n) of the Gaussian component in the wavelet filter.

$$A_n(x) = |a_n(x)|^2 \tag{4.13}$$

Since in this work we are comparing A_n between different models, we have the freedom to select the value of A, and so we adopt the value of $\mathrm{A} = 1$.

The wavelet amplitude A_n is a measure of fluctuations in the transmitted transmitted Lyα flux. The higher is the wavelet amplitude, the more fluctuations in the transmitted Lyα flux. As discussed in Section 4.2 the IGM temperature characterizes the absorption features in the Lyα forest. For a hot (cold) IGM, we have a comparatively smooth (rapidly varying) flux. This results in small (large) A_n values for a hot (cold) IGM. Therefore we can use the wavelet amplitude (A_n) as an indicator of the IGM temperature. Previous works, for example, Lidz et al. 2010 and Gaikwad et al. 2021 have used the probability distribution function (PDF) of A_n to constrain the thermal parameters of the IGM, T_o and γ.

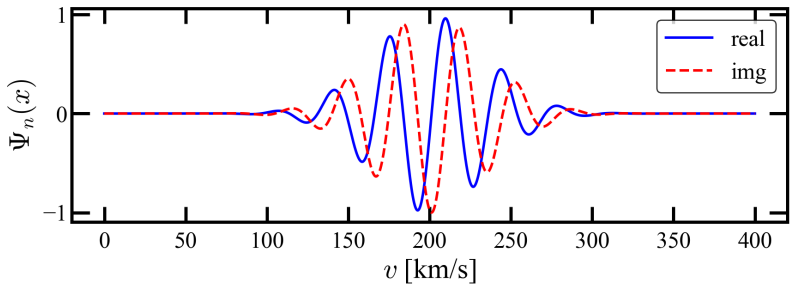


Figure 4.3: Figure shows the Morlet wavelet filter for $s_{\rm n} = 35$ km s^{-1}. The solid blue and the dashed red curves show the real and the imaginary part of the filter.

In this work, we use wavelet analysis to probe the temperature fluctuations from different reioization models at small scales $k \gtrsim 0.06$ km^{-1}s, corresponding to a velocity separation of $v \lesssim 100$ km s^{-1}. To perform wavelet analysis, we generate the Lyα forest spectrum for inhomogeneous models in the redshift bin $z = 4.4$, considering a bin width of $\Delta z \approx 0.4$. We restrict ourselves to the scales $35 \lesssim s_n \lesssim 100$ km s^{-1}, because below 35 km s^{-1} the instrumental broadening and S/N affects the Lyα forest spectrum, affecting our analysis. We perform the wavelet analysis at smoothing scales, $s_{\rm n} = 35,\ 50,$ and 100 km s^{-1}.

CHAPTER 5

Results

This chapter presents the main results of the thesis. The objective is to highlight the impact of different reionization histories and temperature on the thermal state of the intergalactic medium and the Lyα forest. First we show the slices of density field and reionization redshift maps from the simulations. Next, temperature fluctuation maps from different models are shown and discussed in detail. We then compare the absorption features in transmitted Lyα flux between early and late models at different reionization temperatures. Finally, we present the results of using the flux power spectrum and wavelet statistics on the Lyα forest spectrum from different models.

5.1 Density, reionization redshift, and temperature maps

In this section, we present the slice through the simulation box of density, reionization redshift, and temperature fluctuations maps at $z = 4$.

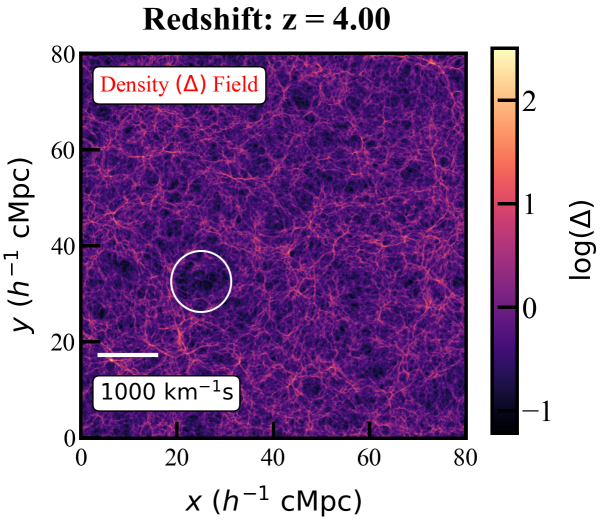


Figure 5.1: Slice of the density field from Sherwood simulations at $z = 4$. The region highlighted in the white circle shows a cosmic void with $\Delta \lesssim \frac{1}{10}$.

5.1.1 Density and reionization redsift maps

Figure 5.1 shows a slice of the density (Δ) field from Sherwood simulations at $z = 4$. The x and y axes have a length of 80 h^{-1}cMpc. The color bar shows the log density values. The region highlighted in the white circle represents a low density region with $\Delta \lesssim \frac{1}{10}$. Such regions in the IGM are called cosmic voids. Late ionization of such regions and high heating by the *I-fronts* show a large temperature as we shall see in the upcoming discussion.

In Figure 5.2 a slice through the reionization redshift z_{reion} maps is shown for the early (left panel), mid (center panel), and late (right panel) models. The blue (red) patches represent early (late) ionized regions. Moving from blue to red, the redshift at which a cell is ionized increases from $z_{\rm reion} \sim 5 - 8$. As expected, we see comparatively a higher number of red patches in the early model, suggesting an early ionization of all those regions. In all three panels, the region shown in the white circle has been ionized at $5 \lesssim z \lesssim 6$.

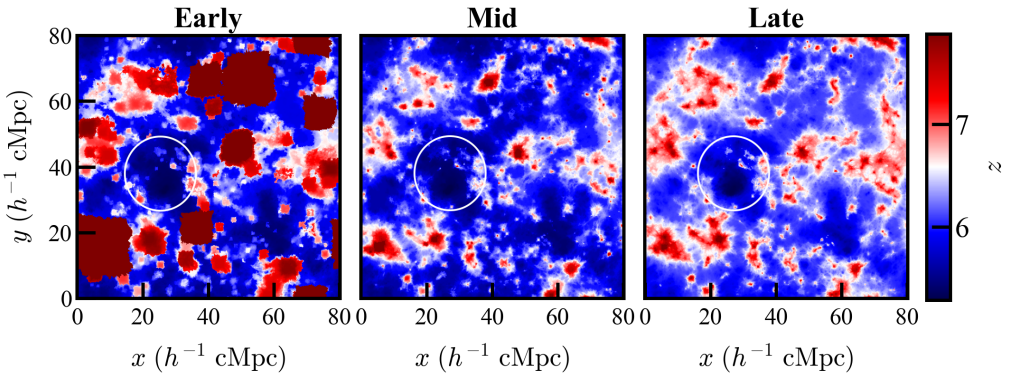


Figure 5.2: Figure shows slice through the reionization redshift z_{reion} maps for the early (left panel), mid (center panel), and late (right panel). The blue (red) patches represent early (late) ionized regions. In all three panels the region shown in white circle is ionized at $5 \lesssim z \lesssim 6$.

5.1.2 Temperature fluctuations in inhomogeneous reionization models at $z = 4$

We now show the temperature maps obtained after performing the radiative transfer on the density fields using the EX-CITE code. We compare the temperature fluctuations produced in the IGM by the early, mid, and late models for different values of $T_{\rm reion}$. Figure 5.3 shows different slices through the temperature field at $z = 4$. Along the row, from upper to lower panel, $T_{\rm reion}$ increases from 10,000 K to 30,000 K. Meanwhile, along the column, from left to right, the reionization history changes from early to late. In the upper panel, for constant value of $T_{\rm reion} = 10{,}000\,\mathrm{K}$, the temperature fields of the three models exhibit similar fluctuations. This is due to the relatively low heating, which allows the gas to cool efficiently. Note that $T_{\rm reion}$ is the temperature of the cell when it is ionized. However, the plots are shown at $z = 4$. In contrast, the lower panel, with $T_{\rm reion} = 30{,}000\,\mathrm{K}$, shows pronounced differences between the early and late models. We observe a larger number of hot regions in the late model. These

variations arise from the difference in timing when a cell is ionized in both models. For example, in the late model, a relatively large fraction of regions have been ionized recently (refer to reionization redshift maps shown in Figure 5.2). Moreover, the ionized regions are set to have a high temperature of 30,000 K. Hence, due to high heating and recent ionization of the cells, the late model shows relatively uniform temperature with more hot regions compared to the early model.

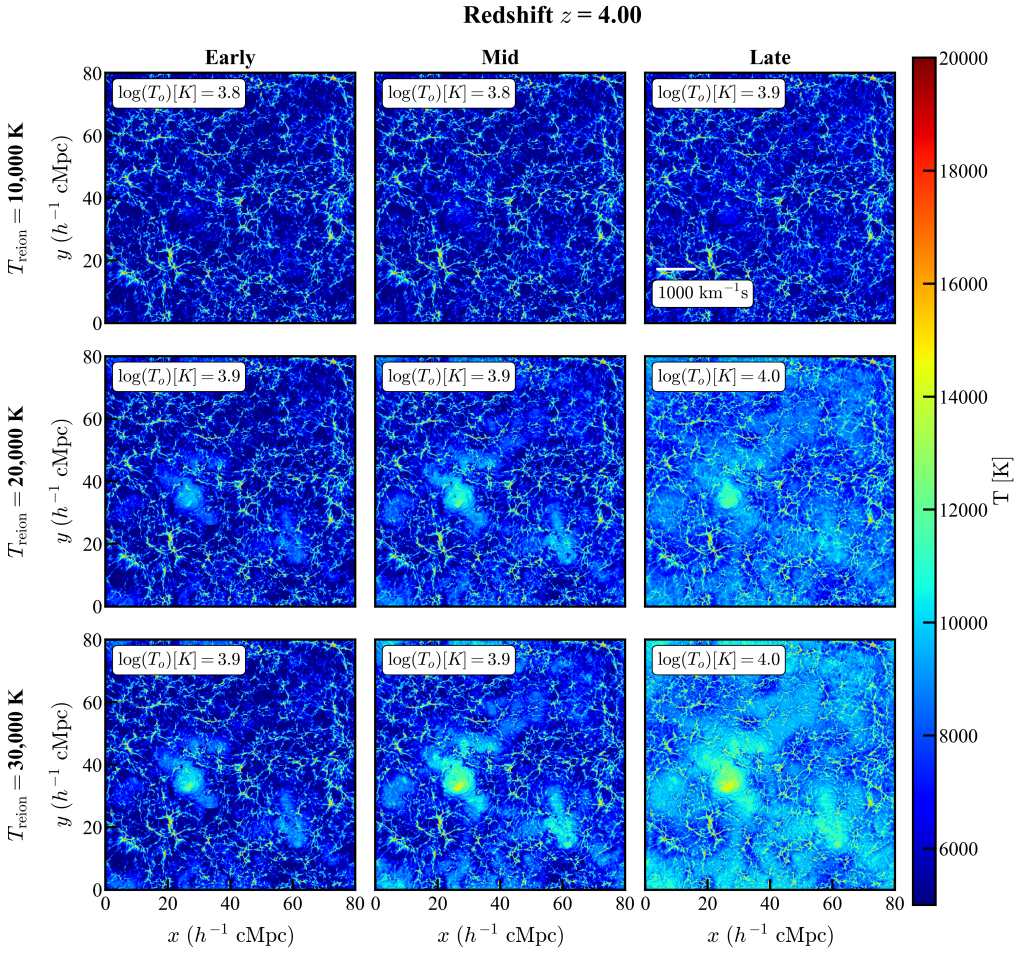


Figure 5.3: Figure shows slices of temperature field from the simulation at $z = 4$. From left to right, the panels correspond to early, mid, and late reionization histories. From upper to lower the reionization temperature T_{reion} increases from 10,000 K, 20,000 K , and 30,000 K. On the upper-left corner of each panel the mean IGM temperature $\log(T_{\rm o})$ is indicated. With $T_{\rm reion}$ the difference in spatial temperature fluctuations in the early and late models increases. The hot region present systematically in the lower panel for a constant $T_{\rm reion}$ = 30,000 K) for all models are due to recent heating of cosmic voids.

Changing $T_{\rm reion}$ also affects the mean IGM temperature, $T_{\rm o}$. For each model, we calculate $T_{\rm o}$ using TDR relation given in Eq 2.8, following the method described in Section 2.3. The differences in the value of $T_{\rm o}$ between the two extreme cases, i.e., early model with $T_{\rm reion}$ = 10,000 K and the late model with $T_{\rm reion}$ = 30,000 K, is $\Delta\, T_{\rm o} \approx 3700$ K. In the lower panels with $T_{\rm reion}$ = 30,000 K, the region in $20 - 40\ h^{-1}$cMpc (for both x and y axes) is systematically hot for all

three models because of its under density (see Figure 5.1) and recent ionization (see Figure 5.2). As discussed previously this region is a cosmic void $\Delta \lesssim \frac{1}{10}$. The dominant cooling mechanism for voids is cosmic expansion. Furthermore, voids are the last regions to get ionized, since they do not host an ionizing source. Since cosmic voids do not have enough cooling time after reionization, these regions are maintained at a higher temperature.

5.2 Temperature Density Relation for inhomogeneous reionization models

We now discuss the temperature density relation for inhomogeneous models. Figure 5.4 shows TDR for the early (left panel), mid (center panel), and late (right panel) models at $z = 4.2$ and $T_{\rm reion}$ = 20,000 K. The best fit in each panel is represented by a dashed black line. The stars in green represent the median temperature corresponding to each $\log(\Delta)$ bin. As expected, the early model shows more scatter in temperature because of the difference in the reionization redshift of difference cells. As we saw earlier in Figure 5.2 some of the regions in the early model are ionized at very high redshift $z \sim 8$, which cool with the expansion of the Universe. Whereas, some are recently ionized $z \sim 5$ providing less time to cool down. The reionization histories also affect the mean IGM temperature measured at a given redshift. The value of $T_{\rm o}$ systematically increases as we go from the early to late model due to an increase in the fraction of pixels with a higher temperature (refer to Figure 5.3). The slope of TDR also becomes flat going from early to late model. This is observed because in late model large fraction of cells are ionized and heated at the same time due to same $z_{\rm reion}$. So heating become isothermal in nature or density independent. The values of ($T_{\rm o}$, γ) calculated for the early, mid, and late models are (7314 K, 1.27), (7977 K, 1.21) and (9516 K, 1.12), respectively.

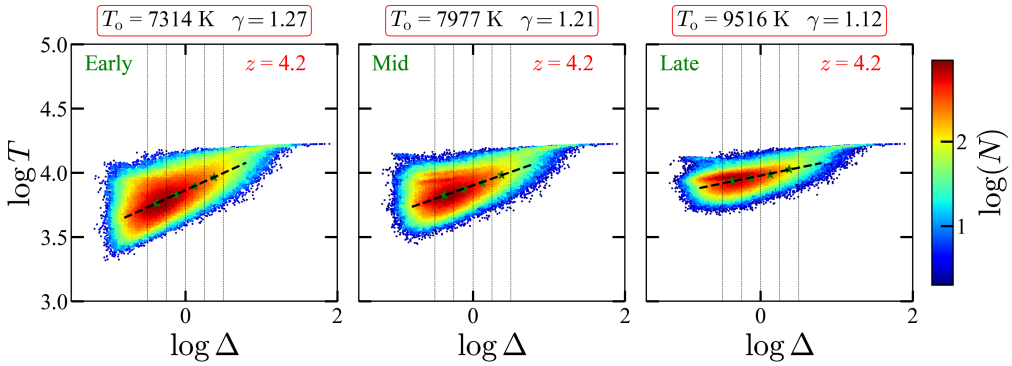


Figure 5.4: Comparison between temperature-density relation (TDR) between the early (left panel), mid (center panel), and late (right panel) models at $z = 4.2$ and $T_{\rm reion}$ = 20,000 K. The best fit in each panel is represented by a dashed black line. The stars in green represent the median temperature corresponding to each $\log(\Delta)$ bin. The mean IGM temperature $T_{\rm o}$ and the slope of the TDR, γ, is indicated on the upper right corner of each panel. The scatter in the temperature reduces as the difference in the reionization redshift for different cell decreases.

In Figure 5.5, we compare the TDR for the mid model with $T_{\rm reion}$ = 20,000 K at z; 4.2 (left panel), 4.6 (middle panel) and 5.0 (right panel). The scatter in temperature decreases as we go towards lower redshift, because the temperature fluctuations fade away as the IGM cools after reionization. The values of ($T_{\rm o}$, γ) calculated $z = 4.2$, 4.6, and 5.0 are (7977 K, 1.21), (8535 K, 1.19) and (9112 K, 1.16), respectively. The fading of temperature fluctuations yields a lower value of $T_{\rm o}$ at lower redshifts.

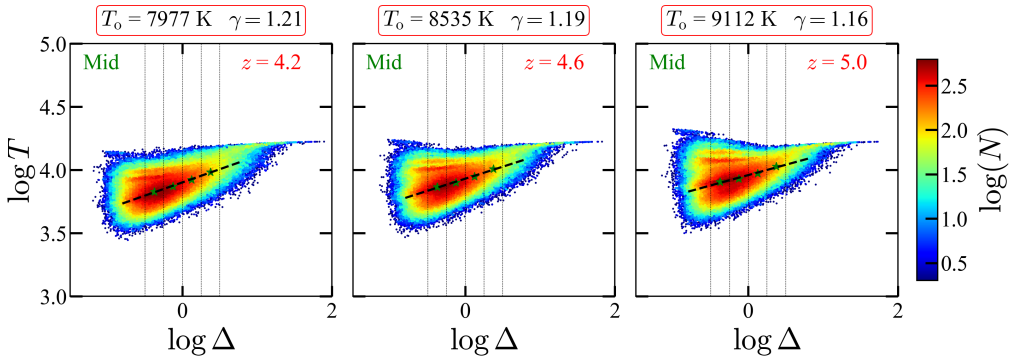


Figure 5.5: Comparison between temperature-density relation (TDR) for the mid model with $T_{\rm reion}$ 20,000 K at z; 4.2 (left panel), 4.6 (mid panel), and 5.0 (right panel). The best fit in each panel is represented by a dashed black line. The stars in green represent the median temperature corresponding to each log(Δ) bin. The mean IGM temperature $T_{\rm o}$ and the slope of the TDR, γ, is indicated on the upper right corner of each panel. The less scatter in temperature as we move to lower redshifts can be attributed to fading of temperature fluctuations due to cosmic expansion.

5.3 Evolution of $T_{\rm o}$

In this section, we discuss the evolution of $T_{\rm o}$ as a function of redshift for inhomogeneous models. The parameters, $T_{\rm o}$ and γ, are computed for the early, mid, and late models, at each redshift bin specified in Section 3.3. The reionization temperature, $T_{\rm reion}$, is varied from 5000 to 50,000 K in steps of 500 K. While calculating $T_{\rm o}$ from temperature maps at a given redshift, temperature of both ionized as well as neutral regions is included. In Figure 5.6, we observe that temperature evolution for all three models shows a steep increment in the temperature at certain redshifts. For example, for the early model, it is near to $z = 8$, and for the late model it is near $z = 6$. This redshifts are close to the mid-point of reioization of these models. For a given model, large fraction of the cells in the simulation box are ionized at redshifts close to the mid-point of reionization. Due to the heating of large number of cells at a similar time, we see a sudden rise in the $T_{\rm o}$ value. From the figure, $T_{\rm o}$ for the late model at $z = 4$. This is because of recent ionization of large fraction of cells in the late model, due to which the ionized cells will have more temperature due to lack of enough cooling time compared to the mid and the early model. At $z = 4$, the minimum value of $T_{\rm o}$ attained by the early, mid, and late models are $\approx$ 6700 K, 6600 K, and 6400 K, respectively. Similarly, the maximum $T_{\rm o}$ attained are $\approx$ 7200 K, 8100 K, and 9700 K.

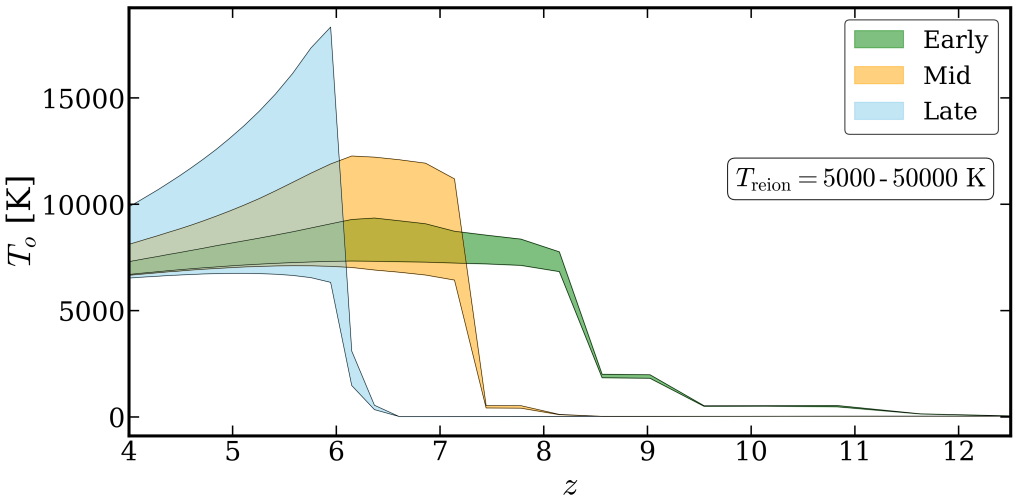


Figure 5.6: Figure shows the evolution of the temperature at cosmic mean density ($\Delta = 1$), $T_{\rm o}$, as a function of redshift for the early, mid, and late reionization models. The green, orange, and blue shaded areas indicate the $T_{\rm o}$ values foe the early, mid, and late models, calculated at each redshift bin specified in Section 3.3 by varying the reionization temperature $T_{\rm reion}$ from 5000 to 50,000 K in steps of 500 K.

Table 5.1: Mean IGM temperature T_0 and slope γ at $z = 4.2$

	$T_{\rm reion} = 10000$ K		$T_{\rm reion} = 20000$ K		$T_{\rm reion} = 30000$ K	
Model	$T_{\rm o}$ (K)	γ	$T_{\rm o}$ (K)	γ	$T_{\rm o}$ (K)	γ
Early	6918	1.30	7244	1.27	7413	1.26
Mid	7244	1.28	7943	1.21	8318	1.19
Late	7586	1.24	9550	1.12	10233	1.09

Table 5.2: Mean IGM temperature T_0 and slope γ at $z = 4.6$

	$T_{\rm reion} = 10000$ K		$T_{\rm reion} = 20000$ K		$T_{\rm reion} = 30000$ K	
Model	$T_{\rm o}$ (K)	γ	$T_{\rm o}$ (K)	γ	$T_{\rm o}$ (K)	γ
Early	7244	1.31	7586	1.26	7726	1.25
Mid	7586	1.27	8511	1.19	8913	1.16
Late	8128	1.21	10715	1.09	11482	1.05

Table 5.3: Mean IGM temperature T_0 and slope γ at $z = 5.0$

	$T_{\rm reion} = 10000$ K		$T_{\rm reion} = 20000$ K		$T_{\rm reion} = 30000$ K	
Model	$T_{\rm o}$ (K)	γ	$T_{\rm o}$ (K)	γ	$T_{\rm o}$ (K)	γ
Early	7413	1.31	7943	1.26	8128	1.24
Mid	7762	1.26	9120	1.16	9550	1.13
Late	8511	1.18	11749	1.05	12882	0.99

5.4 Effects of temperature fluctuations on the absorption features of the Lyα forest

Figure 5.7 illustrates the effect of the hot and cold IGM model on Lyα absorption features. The hot model (solid red) and the cold model (solid blue) have ($T_{\rm o}$, γ) equal to (20,000 K, 1.3) and (10,000 K, 1.3), respectively. As expected, the absorption features in the hot model are broader and shallower. The Lyα forest for the present case is generated considering a homogeneous ionization scenario, where we use the TDR (see Eq. 2.8) to compute the temperature grid along line of sight. Next, we present the effect of temperature fluctuations induced from the early and late reionization models on the Lyα absorption features.

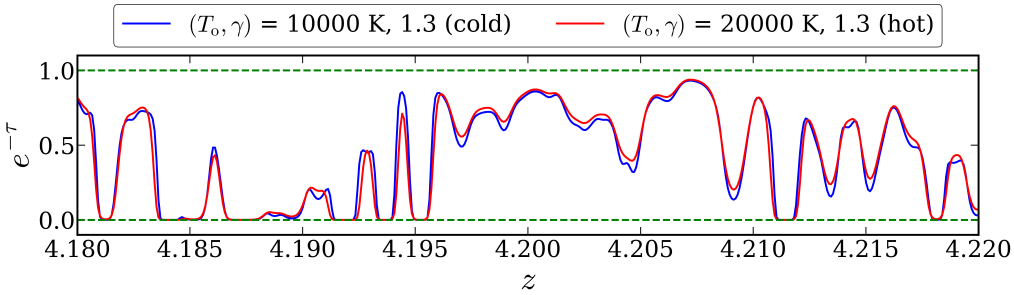


Figure 5.7: Comparison of the Lyα absorption features for hot (solid red) and cold (solid blue) IGM model. The values for ($T_{\rm o}$; γ) for hot and cold model are (20,000 K; 1.3) and (10,000 K; 1.3), respectively.

In Figure 5.8, we compare the absorption features of the early (top panel) and late (bottom panel) models for two reionization temperature; (i) $T_{\rm reion}$ = 10,000 K (solid blue curve) and (ii) $T_{\rm reion}$ = 30,000 K (dashed red curve). In both cases, going from $T_{\rm reion}$ of 10,000 to 30,000 K, the absorption features become shallower, because as we increase $T_{\rm reion}$ IGM attains a higher $T_{\rm o}$. The absorption features of the early model show more difference compared to the late model. This is beacause the early model has more fluctuations in the temperature compared to the late model. In Section 5.6.1, we also compare the absorption features of the early and late models for $T_{\rm reion}$ equal to 30,000 K (see the upper panel of Figure 5.14) and 10,000 K (see the upper panel of Figure 5.15).

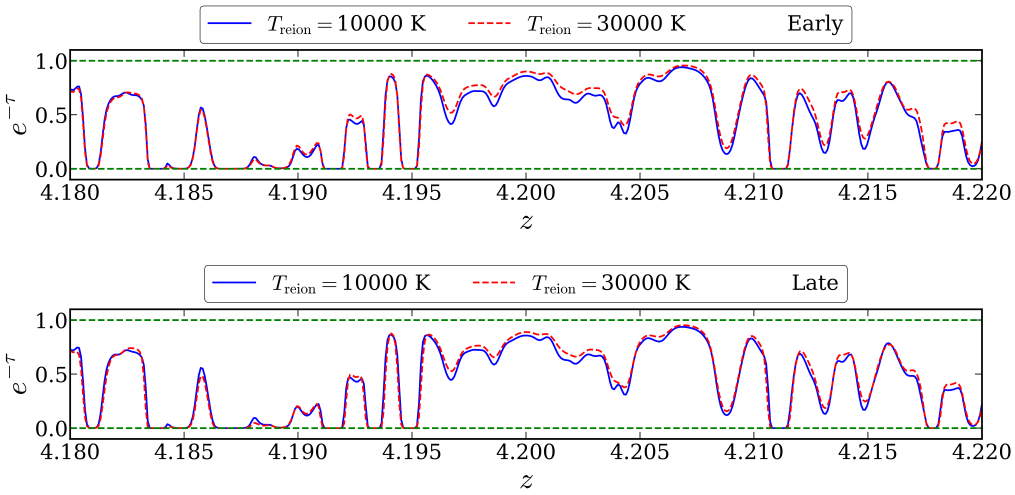


Figure 5.8: Comparison of the Lyα absorption in the early (top panel) and late (bottom panel) reionization models, shown for two reionization temperatures: $T_{\rm reion}$ = 10,000 K (solid blue curve) and $T_{\rm reion}$ = 30,000 K (dashed red curve).

5.5 1D flux power spectrum

In this section, we first investigate the impact of mean IGM temperature on the shape of the flux power spectrum. Following this, we will see how temperature fluctuations affect the flux power of the Lyα forest of different reionization models.

5.5.1 Sensitivity of 1D flux power spectrum to $T_{\rm o}$ and γ

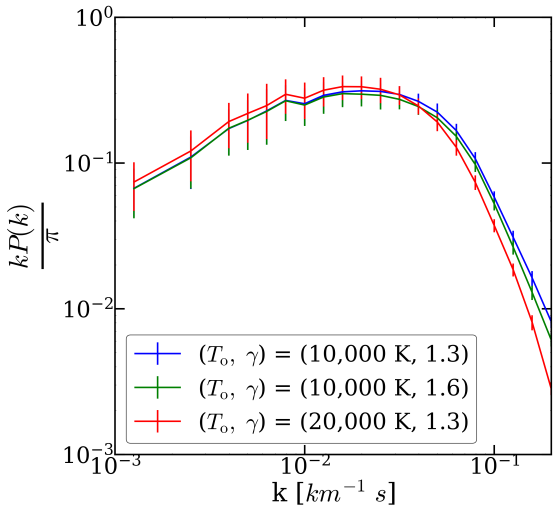


Figure 5.9: The figure illustrates the effect of varying T_0 and γ on the flux power spectrum (FPS). The power spectra are computed for three parameter combinations: $(T_0, \gamma) = (10{,}000\,\mathrm{K},\ 1.3)$, $(10{,}000\,\mathrm{K},\ 1.6)$, and $(20{,}000\,\mathrm{K},\ 1.3)$, shown by the solid blue, green, and red curves, respectively. The parameters $T_{\rm o}$ and γ mainly affects the power spectrum at scales $k \gtrsim 10^{-2}\mathrm{km}^{-1}\mathrm{s}$.

In Figure 5.9, we show the effect of changing T_o and γ on the flux power. We compute the power spectrum for three combinations of (T_o, γ); (10,000 K, 1.3), (10,000 K, 1.6) and (20,000 K, 1.3), shown in solid blue, green, and red lines. The variation in T_o and γ affects the power spectrum on small velocity scales (large k modes). Increasing T_o from 10,000 to 20,000 K increases the broadens the absorption features, causing Lyα flux to smooth out (refer to Section 4.2). This leads to a drop in power at (k (km^{-1}s) $> 10^{-2}$). Reducing γ from 1.6 to 1.3 enhances the power at k (km^{-1}s) $> 10^{-2}$.

5.5.2 Effects of temperature fluctuations on the flux power spectrum

Figure 5.10 illustrates the effect of changing $T_{\rm reion}$ on power spectrum for the early (solid blue), mid (solid green) and late (solid red) models at redshift $z = 4.2$. From left to right panel $T_{\rm reion}$ take values 10,000, 20,000 and 30,000 K. The FPS does not show any significant variation for the three models (early, mid, and late) across the $T_{\rm reion}$ values. This is due to the fact that even though the ionized regions are set to high reinoization temperature, but observing at $z = 4.2$, because of Hubble cooling the temperature fluctuations fade out and the mean IGM temperature T_o does not vary enough across the models to change the shape of the power spectrum. For example, at $z = 4.2$, the maximum difference for T_o and γ obtained between the early and late models is for $T_{\rm reion}$ = 30,000 K, where $\Delta T_o \sim 2800$ K and $\Delta\gamma = 0.17$ (refer to Table 5.1).

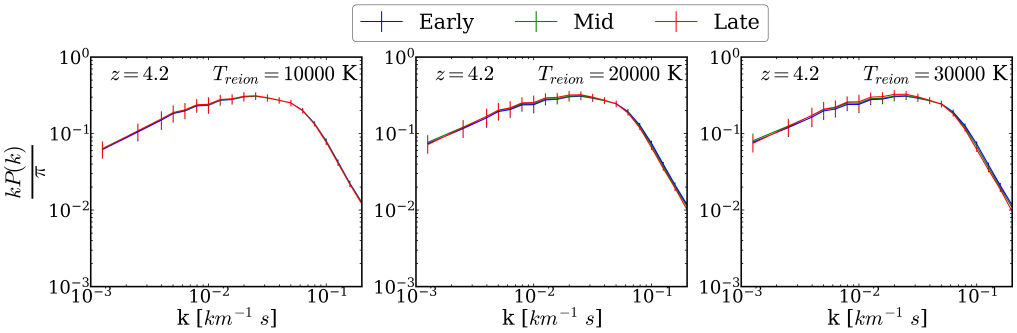


Figure 5.10: The figure shows the 1D flux power spectrum for inhomogeneous models at $z = 4.2$ for different $T_{\rm reion}$ values. The power for the early, mid, and late models are represented in solid blue, green, and red lines. From left to right panel the reionization temperature $T_{\rm reion}$ is varied from 10,000 K to 30,000 K.

Figure 5.11 shows the evolution of the FPS for the early (solid blue), mid (solid green), and late (solid red) models with redshift. The reionization temperature, $T_{\rm reion}$ is set to 20,000 K. From left to right panel the redshift increases as $z = 4.2$ (left), 4.6, (center), 5.0 (right). The peak of the FPS for all three models shifts to higher value as we go to higher redshift because at early times the spatial fluctuations in the temperature are prominent, which slowly fade out as the universe evolves. In addition, we also observe an enhancement in the FPS on large scales (k (km^{-1}s) $< 10^{-2}$), because of an increment in the spatial fluctuations in the neutral hydrogen at large scales, as we go towards higher redshifts. Similarly to Figure 5.10, in each panel, we do not see much variation in

the FPS across three models because for the same reason that there is no significant change in the values of $T_{\rm o}$ and γ. The conclusion from FPS (Figures 5.10 and 5.11) is that it is extremely difficult to distinguish between inhomogeneous reioniozation models using FPS working in the range $10^{-3} \lesssim k(\mathrm{km}^{-1}s) \lesssim 0.2$. In order to address this problem, we take the ratio of power between the inhomogeneous and homogeneous models. We refer the reader to Section 5.5.3 for more details.

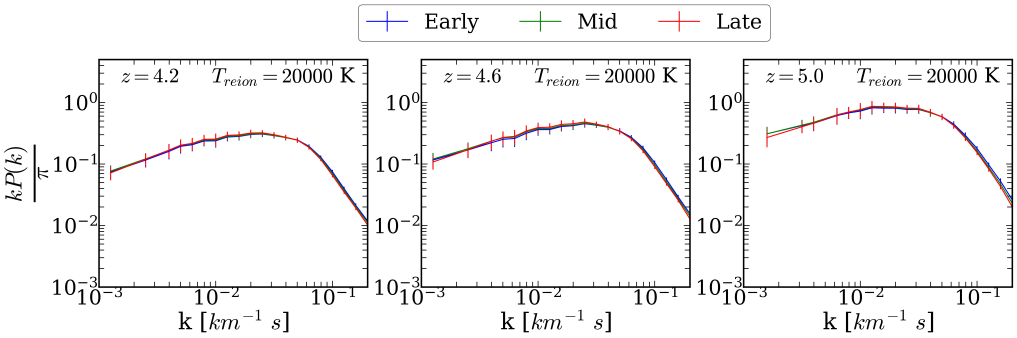


Figure 5.11: The figure shows the evolution of FPS for the early (solid blue), mid (solid green), and late (solid red) models with redshift. The reionization temperature, $T_{\rm reion}$ is set to 20,000 K. From left to right panel the redshift increases as $z = 4.2$ (left), 4.6, (center), 5.0 (right).

5.5.3 Large Scale Power Enhancement

In this section, we plot the ratios of power $R(k, z)$, inhomogeneous to homogeneous models to verify whether our inhomogeneous models produce the enhancement in power at large scales ($\log_{10}\left(\frac{k}{\mathrm{km}^{-1}\,\mathrm{s}}\right) \lesssim -2$) as observed by Wu et al. 2019 and Molaro et al. 2022. The power spectrum ratio $R(k)$ is defined as

$$R(k, z) = \frac{P_{\rm inhomog}(k, z)}{P_{\rm homog}(k, z)}, \tag{5.1}$$

where $P_{\rm inhomog}(k, z)$ and $P_{\rm homog}(k, z)$ are the power computed for the inhomogeneous and homogeneous reionization models, respectively. In order to compute power for the homogeneous model, we first obtain $T_{\rm o}$ and γ using the temperature fields from inhomogeneous reionization model, at a given redshift, using the method discussed in Section 2.3. Thereafter, using the computed values of $T_{\rm o}$ and γ we produce the temperature field using the TDR equation (see Eq. 2.8). We then produce the Lyα forest spectrum using the new generated temperature, density, and neutral hydrogen fraction field. The EX-CITE code executes the radiative transfer in the post processing phase to compute the temperature fluctuations, and hence the Lyα flux produced for the inhomogeneous models uses the same density Δ and velocity v fields as in the homogeneous models.

In Figure 5.12, we compare the ratio of the power, $R(k)$, for the early, mid, and late models shown in solid blue, green, and blue curves, respectively, at $z = 4.2$, for three reionization temperatures; (i) $T_{\rm reion}$ = 10,000 K (left panel), 20,000 K (center panel) and (iii) $T_{\rm reion}$ = 30,000 K (right panel). In the center and right panel, we see an increase in power on large scales k (km^{-1} s) $\lesssim 10^{-2}$. This

is due to spatial fluctuations in the neutral hydrogen fraction induced by inhomogeneous reionization (Molaro et al. 2022). The early model gives more power compared to the late model because the temperature fluctuations in the early model have more contrast arising because of the larger differences in the cooling period for the early and recently ionized regions. The difference in power between the early and late models increases with $T_{\rm reion}$. This is because as we increase the reionization temperature, the recently ionized regions will have a higher temperature due to high heating, but the early ionized regions will not have much difference in their temperature due to Hubble cooling. Comparing the power of the early versus the mid model at $T_{\rm reion}$ = 20,000 and 30,000 K, we see that the mid model shows slightly higher power. This behavior can be attributed to the fading of temperature fluctuations in the early model on large scales as the universe cools due to Hubble expansion. As a larger fraction of the regions are ionized at early times in the early model compared to the mid model, we get comparatively less contrast in the temperature fluctuations in the early model at $z = 4.2$, resulting in less power. For $T_{\rm reion}$ = 30,000 K, the power on large scales is increased by 20 %. On the other hand, on small scales k (km^{-1} s) $\sim 10^{-1}$, we do not see any enhancement or suppression of power. This is because the Lyα Forest simulated for inhomogeneous and homogeneous reionization uses the same density and peculiar velocity field. This is discussed in Figure 3 from Molaro et al. 2022, where the green curve represents the ratio of power after replacing the peculiar velocity field in their mid RT-hybrid model with that of the homogeneous model. In Figure 5.10, we see that using FPS we cannot distinguish between reionization models. Figure 5.12 suggests that inhomogeneous reioization enhances flux power on large scales. Moreover, taking the power ratio $R(k)$ for early, mid, and late models, we see a different level of power enhancement due to the distinct nature of temperature fluctuations. Hence, the enhancement of power on large scales can be used to distinguish between reionization models.

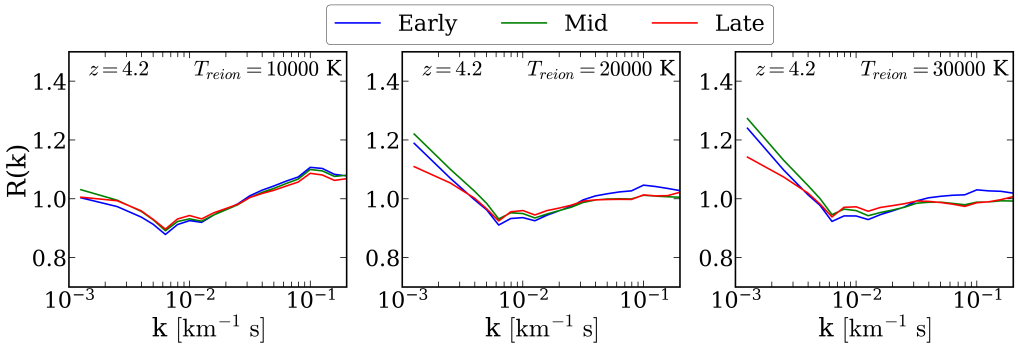


Figure 5.12: Comparison of the ratio of the power, $R(k)$, computed for the early (solid blue curve), mid (solid green curve), and late (solid red curve) models at $z = 4.2$, for three reionization temperatures; (i) $T_{\rm reion}$ = 10,000 K (left panel), (ii) $T_{\rm reion}$ = 20,000 K (center panel), and (iii) $T_{\rm reion}$ = 30,000 K (right panel).

5.5.4 Flux power spectrum on small velocity scales

The FPS calculated in the previous section was ranging between k-modes $0.001 \leq k$ (km^{-1} s) ≤ 0.2. This corresponds to a physical velocity separation of $30 \lesssim v$ (km s^{-1}) $\lesssim 6200$. In this section, we calculate the FPS for our models, probing velocity scales below 30 (km^{-1} s). This is study the effect of temperature fluctuations present on the small scales on the small scale structures of the Lyα forest absorption features.

Figure 5.13 compares the FPS for the early (blue solid) and the late (red solid) models calculate for $T_{\rm reion}$ 30,000 K at at $z = 4.2$. The k-modes range between $0.01 \leq k$ (km^{-1} s) ≤ 0.9. The FPS of both the model show considerable differences at k values $\gtrsim 0.01$ (km^{-1}s). As we to higher k modes the early model shows a higher power because of the rapidly varying absorption features arising from strong temperature fluctuations compared to the late model. However, this feature cannot assist us to differentiate between two model with confidently. This due to the fact that small velocity scale the absorption features are affected instrumental noise, S/N, thermal noise, etc, will reduce the difference between FPS at small scales. Hence, we need other method to quantify the effect temperature has on the small scale structures of the Lyα forest. In the next section, we will discuss how wavelet statistics will help overcome this problem.

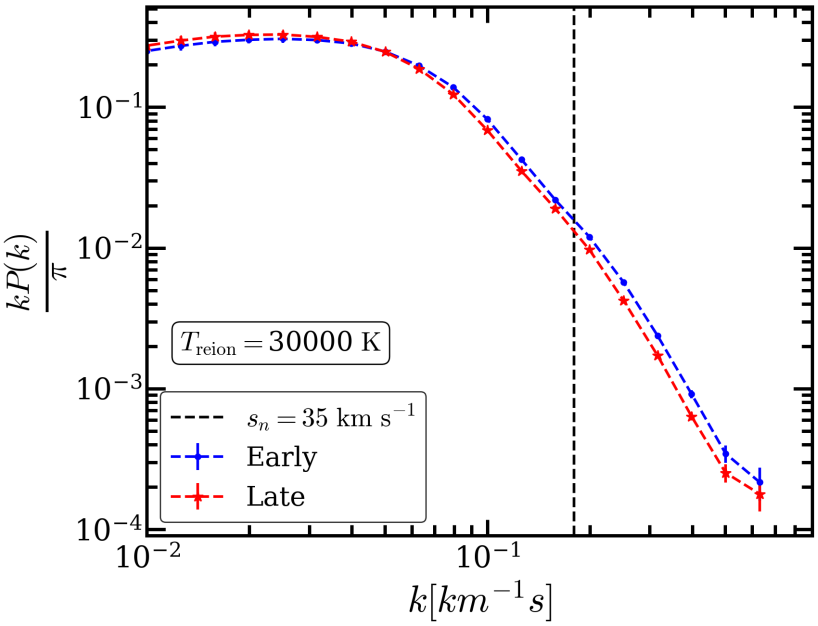


Figure 5.13: Comparison between FPS of the early (blue solid) and late (red solid) model at $z = 4.2$ for $T_{\rm reion}$ = 30,000 K. The dashed black solid line represents a velocity separation of $v = 35$ km s^{-1}. At $k \gtrsim 0.1$ km^{-1} s the early model shows a higher power because of the rapidly varying absorption features arising from strong temperature fluctuations compared to the late model.

5.6 Wavelet Amplitude (A_n)

This section shows the sensitivity of the wavelet amplitude to the temperature fluctuations in the IGM. We compute the wavelet amplitude for smoothing scales,

s_n = 35, 50, and 100 km s^{-1} and $T_{\rm reion}$ 10,000 K and 30,000 K.

5.6.1 Effects of temperature fluctuations on the wavelet amplitude

Figure 5.14 shows the variation in the Lyα flux (top panel) and the log wavelet amplitude, log($A_{\rm n}$) (bottom panel), for the early (solid blue) and late (dashed red) models for $T_{\rm reion} = 30{,}000$ K at $z = 4.4$. The smoothing scale adopted for the wavelet filter is $s_{\rm n} = 35$ km s^{-1}. Due to a high $T_{\rm reion}$ and less cooling time in the case of the late model, we see a uniform temperature field with a larger fraction of hot regions (see the figure 5.3). This also increases the mean IGM temperature for the late model. As a result, the absorption features in the late model are broader and shallower, giving a smooth flux field. This results in giving a systematically lower value to the wavelet amplitude (see the dashed red curve), as shown in the bottom panel.

In Figure 5.15, we reduce the reionization temperature, setting up $T_{\rm reion} = 10{,}000$ K. Because of a lower $T_{\rm reion}$ the ionized regions can cool down quickly, giving temperature fluctuations similar to those in the early model. Because of this, the difference in the Lyα flux between the early and late models is reduced. Moreover, the values of the wavelet amplitude attained by the two models are very similar.

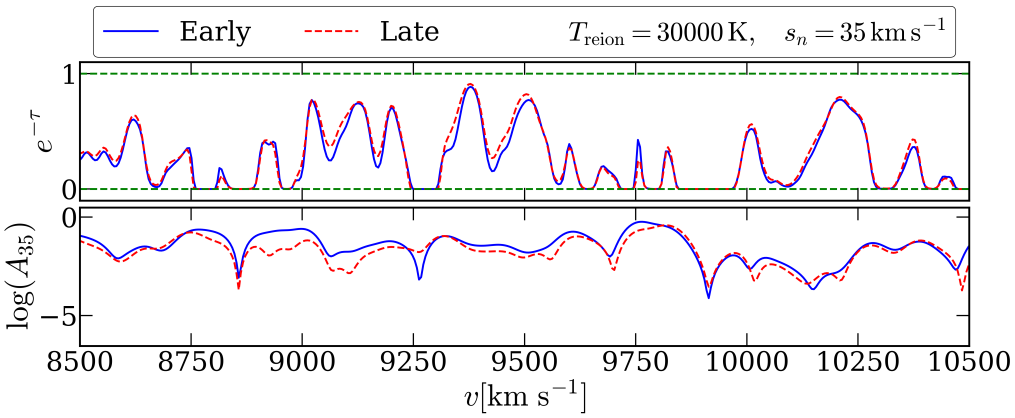


Figure 5.14: Figure shows the variation in the Lyα flux (top panel) and the log wavelet amplitude, log($A_{\rm n}$) (bottom panel), for the early (solid blue) and late (dashed red) models for $T_{\rm reion} = 30{,}000$ K at $z = 4.4$. The smoothing scale adopted for the wavelet filter is $s_{\rm n} = 35$ km s^{-1}

In Figure 5.16, we compare log($A_{\rm n}$) for the early (solid blue) and late (dashed red) reionization models at three smoothing scales: (i) $s_{\rm n} = 35$ km s^{-1} (top panel), (ii) $s_{\rm n} = 50$ km s^{-1} (middle panel), and (iii) $s_{\rm n} = 100$ km s^{-1} (bottom panel). In all panels, the reionization temperature is fixed at $T_{\rm reion} = 30{,}000$ K. At small smoothing scales ($s_{\rm n} = 35$ km s^{-1}), there is a clear difference in the wavelet amplitudes between the early and late models. This is because small smoothing scales are sensitive to fine structures in the Lyα forest, which are strongly affected by temperature fluctuations in the intergalactic medium.

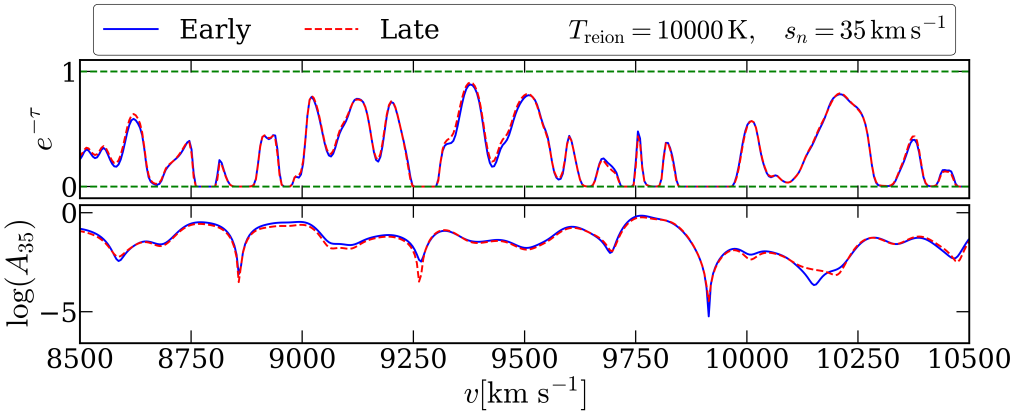


Figure 5.15: Similar to figure 5.14, instead for $T_{\rm reion} = 10{,}000$ K.

As the smoothing scale increases to 50 and 100 km s^{-1}, these small-scale differences are progressively smoothed out. Larger smoothing scales average over finer details in the flux, making the wavelet amplitude less sensitive to temperature differences between the models. As a result, the distinction between the early and late reionization scenarios becomes weaker at larger $s_{\rm n}$.

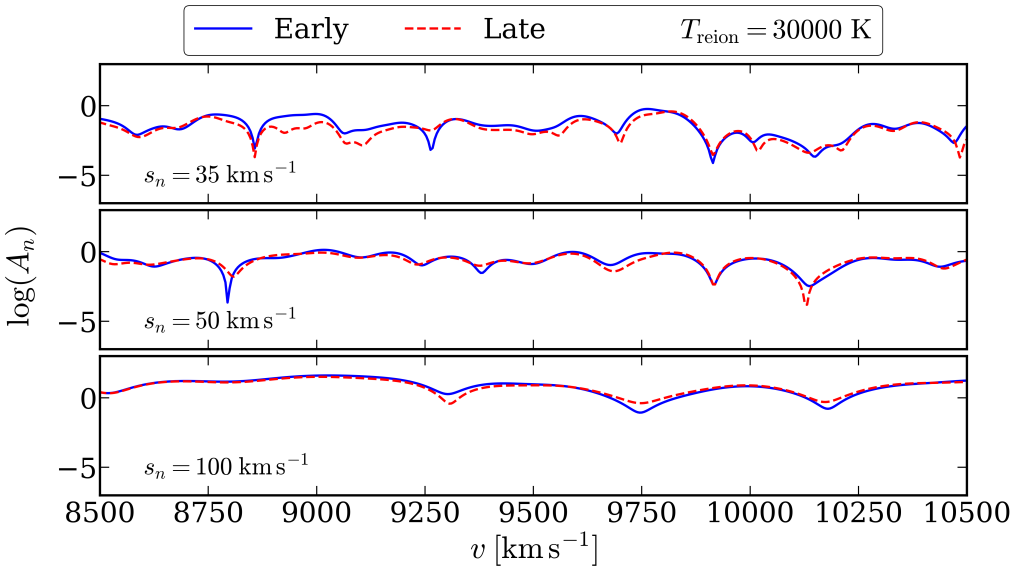


Figure 5.16: Comparison for $\log(A_{\rm n})$ between the early (blue solid) and late (dashed red) models for three smoothing scales. (i) $s_{\rm n} = 35$ km s^{-1} (top panel), (ii) $s_{\rm n} = 50$ km s^{-1} (middle panel), and (iii) $s_{\rm n} = 100$ km s^{-1} (bottom panel). For all the panels the reionization temperature is set at $T_{\rm reion} = 30,000$ K.

5.6.2 Probability distribution function (PDF) of $\langle log(A_{\rm n})\rangle$

In Figure 5.15 and Figure 5.14 we have shown the effect on varying $T_{\rm reion}$ on the wavelet amplitude. Moreover, Figure 5.16 shows the effect of varying s_n on the wavelet amplitude. Now, we use produce the PDF of mean of the log of wavelet amplitude ($\langle log(A_{\rm n})\rangle$) to compare between the temperature fluctuations in different models at small velocity scales ($v \lesssim 100$ km s^{-1}). The quantity $\langle A_n\rangle$ is the mean of the log wavelet amplitude, computed a single sight line.

For a given reionization model, we construct the PDF for $\langle log(A_n)\rangle$ over 1024 skewers. We compare the PDF of $\langle log(A_{\rm n})\rangle$ between the early and late models at $z = 4.4$ for different values of $T_{\rm reion}$ and s_n.

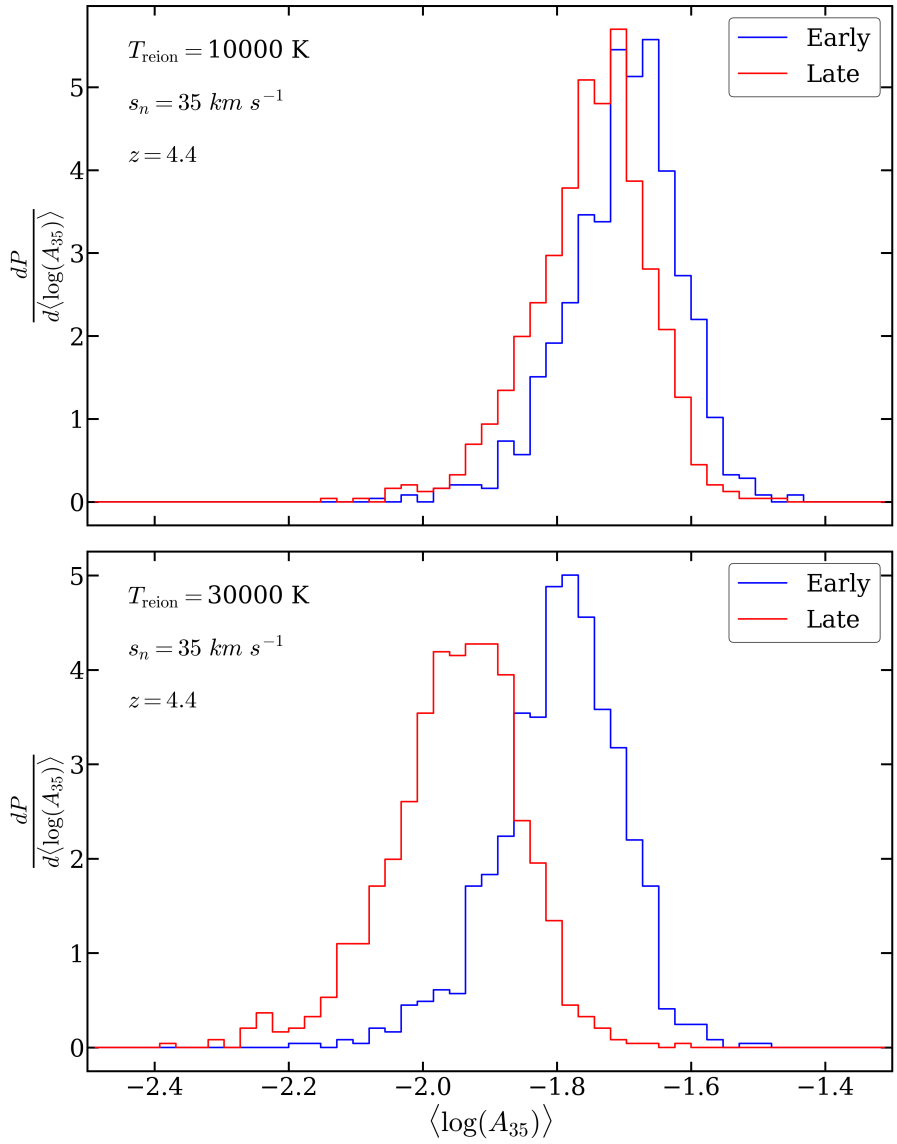


Figure 5.17: Comparison of the PDF of $\log(A_{\rm n})$ between the early (blue solid) and late (dashed red) models for two $T_{\rm reion}$ values. (i) $T_{\rm reion}$ = 10,000 K (upper panel) and (ii) $T_{\rm reion}$ = 30,000 K (lower panel). The wavelet filter scale s_n is fixed at 35 km s^{-1}.

Figure 5.17 shows the comparison of the PDF of $\log(A_{\rm n})$ between the early (blue solid) and late (dashed red) models for two $T_{\rm reion}$ values. (i) $T_{\rm reion}$ = 10,000 K (upper panel) and (ii) $T_{\rm reion}$ = 30,000 K (lower panel). The wavelet filter scale s_n is fixed at 35 km s^{-1}. In both the panels the PDF distribution for the early model is centered at a higher value of A_n. This result is expected, because the early model produces more temperature fluctuations compared to the late model which results into a higher wavelet amplitude. (refer to Figure 5.14 & 5.15). As $T_{\rm reion}$ increases from 10,000 to 30,000 K, the centers of the distributions move further apart. This is because as $T_{\rm reion}$ increases the the small scale features in

the Lyα forest spectrum shows more fluctuations. This further can be explained from the fact that there is more difference between the temperature fields of the early and late models when $T_{\rm reion}$ = 30,000 K compared to $T_{\rm reion}$ = 10,000 K (refer to Figure 5.3).

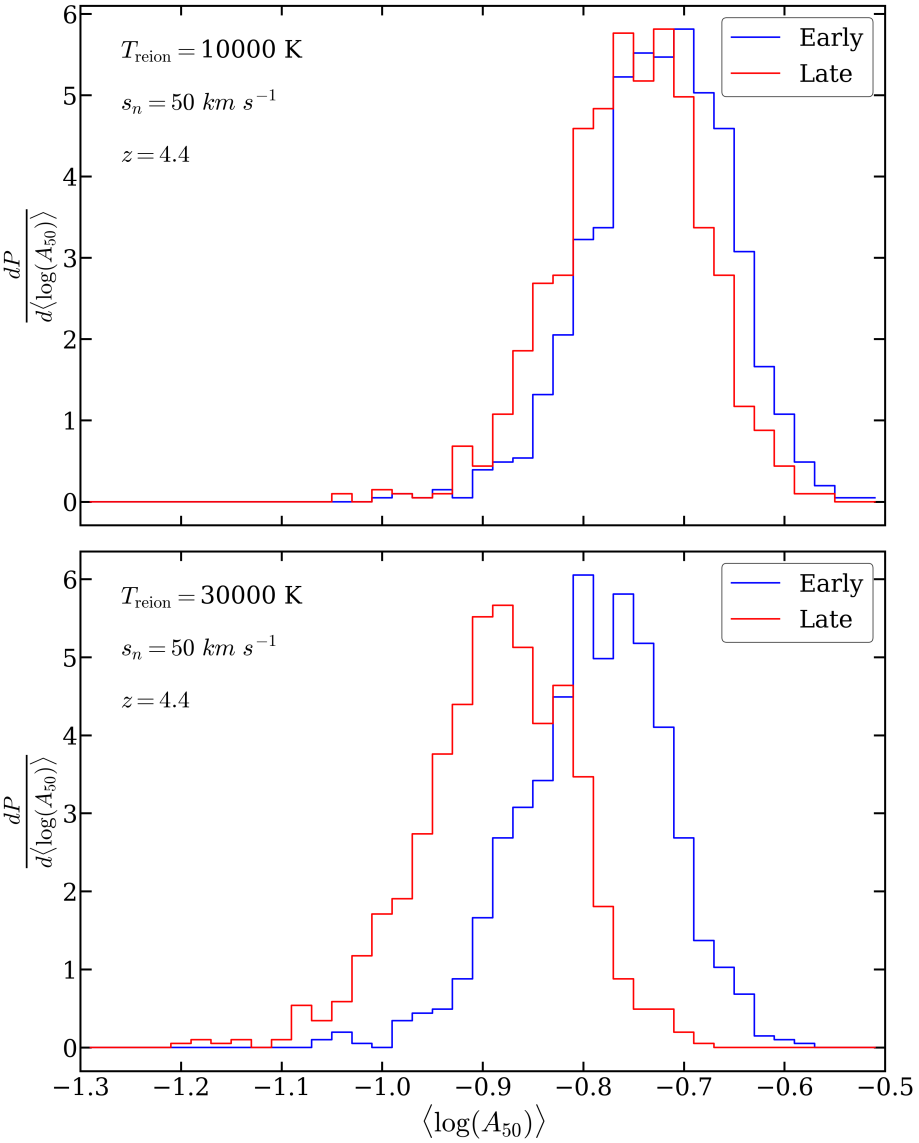


Figure 5.18: Comparison of the PDF of $\log(A_{\rm n})$ between the early (blue solid) and late (dashed red) models for two $T_{\rm reion}$ values. (i) $T_{\rm reion}$ = 10,000 K (upper panel) and (ii) $T_{\rm reion}$ = 30,000 K (lower panel). The wavelet filter scale s_n is fixed at 50 km s^{-1}.

In Figure 5.18, we increase s_n = 50 km s^{-1}, and compare the PDF for the early and late model for $T_{\rm reion}$ = 10,000 and 30,000 K. For s_n = 50 km s^{-1}, the PDF's for both models is systematically shifted to higher A_n. This is because of a higher variance in the Lyα flux contrast (δ_F). The same behavior is also observed in the 1D flux power spectrum. Going towards larger velocity scales (smaller k-modes) the power increases. Next, we discuss the difference in the wavelet amplitude between early and the late model. Compared to the previous case, the separation between the distributions have slightly decreased. This is

due to similar variations in the Lyα flux at larger velocity scales.

In Figure 5.19, we increase s_n to 100 km s^{-1}. The distributions are shifted to even higher A_n values. Moreover, the separations in the distributions have further reduced, and they almost overlap. This makes it very difficult to distinguish them.

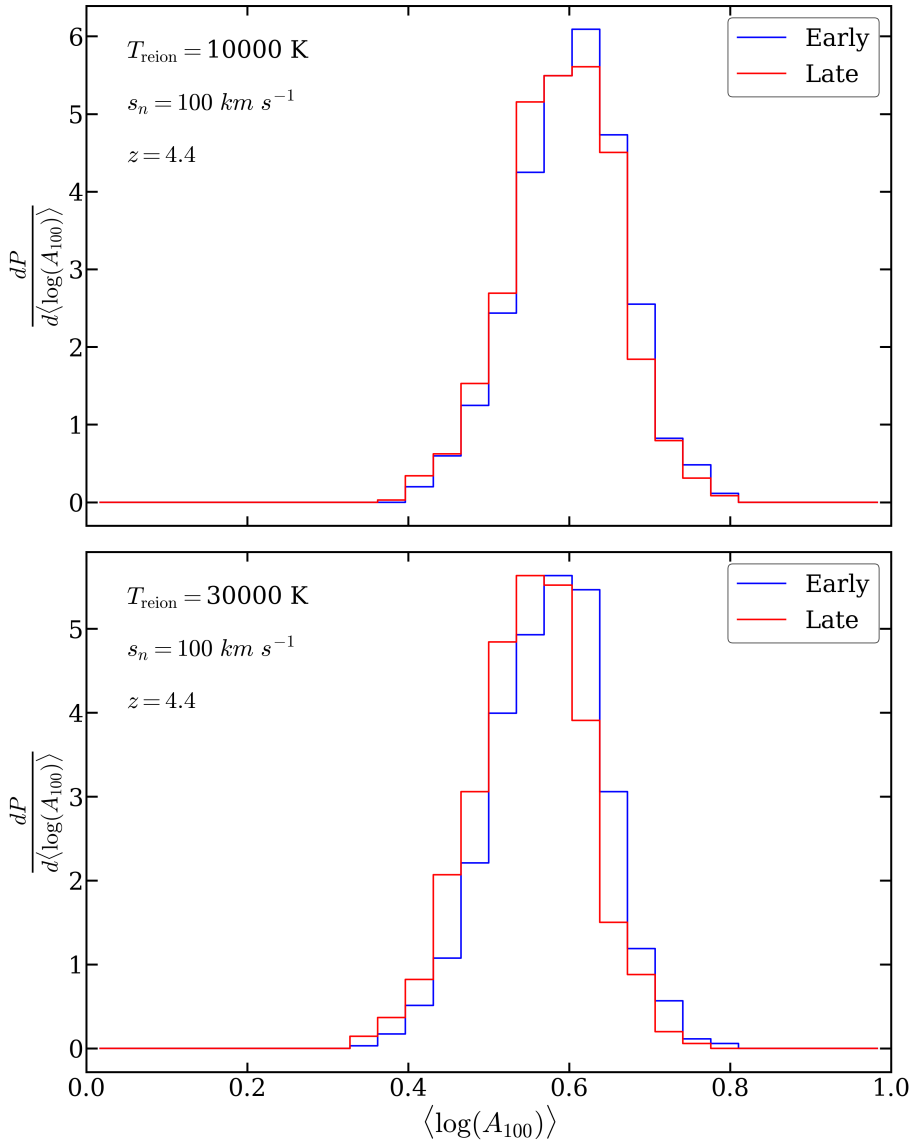


Figure 5.19: Comparison of the PDF of $\log(A_{\rm n})$ between the early (blue solid) and late (dashed red) models for two $T_{\rm reion}$ values. (i) $T_{\rm reion}$ = 10,000 K (upper panel) and (ii) $T_{\rm reion}$ = 30,000 K (lower panel). The wavelet filter scale s_n is fixed at 100 km s^{-1}.

From our analysis of wavelet amplitude and their distributions, we have learned that the PDF of $\langle log(A_{\rm n})\rangle$ is sensitive to the IGM temperature at small velocity scales. For s_n = 35 and 50 km s^{-1} the distributions of the early and the late model are clearly distinguishable. This indicates that the wavelet filter is very well able to capture and differentiate the temperature fluctuations from two different models at small velocity scales. This result can be useful to distinguish between inhomogeneous reionization models.

CHAPTER 6

Summary and Future Scope

In this chapter, we summarize the main findings of the thesis. We further discuss the implications, limitations, and improvements in our work.

6.1 Summary

The objective of this thesis was to constrain the temperature fluctuations present in the intergalactic medium, shortly after hydrogen reionizaton, using Lyα forest. For this, we worked with a large set of simulations, where the cosmological hydrodynamical simulation is based on the Sherwood simulation suite performed using the P-GADAGET-3 code. The radiative transfer was performed in a post processing step using the EX-CITE code that solves set of equilibrium photoionization equations (see Eq 2.6), photoheating equation (see Eq. 2.1 & 2.2) and thermal evolution equation of the IGM (see Eq. 2.5), producing spatial fluctuations in the hydrogen photoionization rate ($\Gamma_{\rm HI}$) to simulate a inhomogeneous reionization scenario. Because of inhomogeneous reionization, spatial temperature fluctuations are induced in the IGM, that evolve as reionization process continues. Our simulations have $z_{\rm mid}$ and $T_{\rm reion}$ as a free parameter and their combination is used to produce different reionization models. In this work, we consider three reionization histories "early", "mid", and "late" having mid-point $z_{\rm mid} \approx$ 8.35, 7.2, and 6.15, respectively. Moreover, $T_{\rm reion}$ varies from 5000 to 50,000 K in steps of 500 K. The combination of these two parameters are used to produce a total of 273 reionization models. Out of all models, we mainly work with a set of 9 models. For each early, mid, and late model, we vary $T_{\rm reion}$ as 10,000 K, 20,000 K, and 30,000 K. Next, using the density, temperature, velocity, and neutral hydrogen fraction fields from simulation outputs, we produce 1024 skewers of the Lyα forest spectrum for the above specified nine models. Following this, we study the impact of temperature variations on the Lyα forest and apply Lyα statistics in order to quantify these effects.

First, we perform a qualitative analysis of the temperature fields produced by our reionization models. We compare the temperature fluctuations produced by the early, mid, and late models for $T_{\rm reion}$ 10,000 K, 20,000 K, and 30,000 K (see Figure 5.3). We find that on increasing $T_{\rm reion}$ the difference in the spatial distribution of temperature between the early and the late model increase. For $T_{\rm reion}$ = 30,000 K, the late model shows more uniform temperature with a larger fraction of hot regions. Whereas, the temperature of the early model has more

contrast showing more spatial fluctuations. This behavior is attributed to the high heating and difference in the timing of reionization of different cells in both these models. We also find that some regions are systematically hot in all the three models. This is because of high heating and recent ionization of under dense regions called "cosmic voids", with $\Delta \lesssim \frac{1}{10}$.

We, next study the temperature density relation of the IGM for inhomogeneous reionization. In Figure 5.4, we compare the TDR between the early, mid, and late models at $z = 4.2$ for $T_{\rm reion}$ = 20,000 K. We find that the scatter in the temperature decreases from early to the late model. This is because of large fraction of cells being ionized and heated up at the same time in the late model making the temperature independent of density. We compute $T_{\rm o}$ and γ using the method described in the Section 2.3 for the three models and find $T_{\rm o}$ to be increasing from early to late model. The obtained ($T_{\rm o}$, γ) are (7314 K, 1.27), (7977 K, 1.21) and (9516 K, 1.12) for the early, mid, and late models, respectively. In Figure 5.5, we show the evolution of TDR for the mid model with redshift increasing z from 4.2 to 4.6. The scatter in the temperature less at $z = 4.2$, because of the fading of the temperature fluctuations due to the adiabatic cooling of ionized regions from the cosmic expansion. The values of ($T_{\rm o}$, γ) calculated $z =$ 4.2, 4.6, and 5.0 are (7977 K, 1.21), (8535 K, 1.19) and (9112 K, 1.16), respectively. The fading of temperature fluctuations yields a lower value of $T_{\rm o}$ at lower redshifts.

In Figure 5.6, we show the evolution of $T_{\rm o}$ from $z = 12$ up to $z = 4$ for all our models. We get a higher $T_{\rm o}$ for the late model at $z = 4$. This is because of recent ionization of cells in the late model, which causes the cell to be still hot compared to the mid and the early model where cells starting ionizing at much earlier redshifts. At $z = 4$, the minimum value of $T_{\rm o}$ attained by the early, mid, and late models are $\approx$ 6700 K, 6600 K, and 6400 K, respectively. Similarly, the maximum $T_{\rm o}$ attained are $\approx$ 7200 K, 8100 K, and 9700 K. The Table 5.1, 5.2, and 5.3 summarizes $T_{\rm o}$ and γ computed at $z = 4.2$, 4.6, and 5.0, respectively, for the early, mid, and late models for $T_{\rm reion}$ 10,000, 20,000 and 30,000 K.

Next, we study the impact of the IGM temperature and temperature fluctuations on the absorption features of Lyα forest. We first compare the effect hot and cold IGM with ($T_{\rm o}$, γ) equal to (20,000 K, 1.3) and (10,000 K, 1.3) on the Lyα absorption features shown in Figure 5.7. We find the features to be broader and shallower for the hot IGM. This is due to smoothing of small scale structures in the Lyα forest and reduced recombination rate. Next, we vary $T_{\rm reion}$ between 10,000 and 30,000 K and compare the absorption features of the early and the late model in Figure 5.8. The early more shows comparatively rapidly varying features, because of more temperature fluctuations present in the early model. With increasing $T_{\rm reion}$ this differences between the early and late model also increases.

Following this, we employ two Lyα statistics, namely, 1D flux power spectrum and wavelet to quantify the effects of IGM temperature fluctuations on the Lyα forest in the redshift range $4 \leq z \leq 5$. First, we compute the 1D flux power spectrum for the Lyα forest at redshift bins $z = 4.2$, 4.6, and 5.0 with a bin width 0.088. The choice of the specified bins and bin width comes from the power spectrum computed by Molaro et al. 2022. In Figure 5.9 we study the sensitivity of the power spectrum to the parameters $T_{\rm o}$ and γ. We compute

the power spectrum for three combinations of (T_o, γ); (10,000 K, 1.3), (10,000 K, 1.6) and (20,000 K, 1.3). The variation in T_o and γ mainly affects the power spectrum on small velocity scales (large k modes). Increasing T_o broadens the absorption features, causing Lyα flux to smooth out and leads to a drop in power at (k (km^{-1}s) $> 10^{-2}$).

Next, we study the effects of temperature fluctuations the power spectrum. In Figure 5.11, we the evolution of the FPS for the early, mid, and late models with redshift increasing from 4.2 to 5.0. We fix $T_{\rm reion}$ at 20,000 K. We observe that the peak of the FPS for all three models shifts to higher value as we go to higher redshift because of the evolution of the IGM. In addition, we also observe an enhancement in the FPS on large scales (k (km^{-1}s) $< 10^{-2}$), because of an increment in the spatial fluctuations in the neutral hydrogen at large scales, as we go towards higher redshifts. However, we at each redshift we do not see any significant difference between the power spectrum of the three models. Thus we find that it is extremely difficult to distinguish between inhomogeneous reionization models using FPS in the range $10^{-3} \lesssim k(\mathrm{km}^{-1}s) \lesssim 0.2$. To address this problem, we further take the ratio of power R(k) between the inhomogeneous and homogeneous models.

In Figure 5.12, we compare the ratio of the power, R(k), for the early, mid, and late models respectively, at $z = 4.2$, for three reionization temperatures; at $T_{\rm reion}$ = 10,000 , 20,000 , 30,000 K. We find a large scale enhancement (for $k \lesssim 10^{-2}$ km^{-1} s) in the power for all the models. This is due to the spatial variations in the neutral hydrogen fraction present in the IGM. In addition, we observe that this enhancement increases with $T_{\rm reion}$ giving up to 20 % enhancement to the power. This is because the strength of temperature fluctuations also increase with $T_{\rm reion}$. We find that plotting R(k), a clearly distinction between the early and the late models at k modes $\lesssim 10^{-2}$ km^{-1} s. However, at higher k-modes $k \sim 10^{-1}$ km^{-1} s, the models cannot be distinguished easily. Moreover, since our models inhomogenous and homogeneous models uses the same peculiar velocity fields, our power spectrum ratio R(k) is does not show the suppression in the power at k modes $\sim 10^{-1}$ km^{-1} s, as observed by Molaro et al. 2022. To address this issue, we further use wavelet statistics.

The wavelet filter is sensitive to the fluctuations in the transmitted Lyα flux at a given filter scale s_n. Using this property of the filter, we compute the wavelet amplitude (A_n) of the Lyα forest, for different combination of s_n and $T_{\rm reion}$. In Figure 5.15 and 5.14, we keep s_n fixed at 35 km s^{-1} and see how $T_{\rm reion}$ affects A_n. We find A_n to be relatively large for the early model and the difference increases with $T_{\rm reion}$. This is because of the stronger temperature fluctuations produced in the early model. In Figure 5.16, we show that increasing s_n, shifts overall A_n, but suppresses variations at small velocity scales.

Finally, in Figures 5.17, 5.18, and 5.19, we compare the probability distributions of $\langle log(A_{\rm n})\rangle$ of the early and late models for different combination of s_n and $T_{\rm reion}$. We find the PDFs of the early and late models to have clearly distinct centers. The separation is higher for higher $T_{\rm reion}$ and reduces as we increase s_n from 35 to 100 km s^{-1}.

From our overall analysis, we find that the early model gives rise to stronger temperature fluctuation compared to the other two models. The effect of this is reflected in absorption features of the Lyα forest. Performing analysis using

FPS, we find that it is extremely difficult to separate two models. This problem can be resolved by taking ratio of the power spectrum, R(K), of the inhomogeneous and homogeneous models. Plotting the R(k), we find an enhancement in the power at large velocity scales. This is a signature of inhomogeneous reionization, increasing power up to 20 % at k modes $\lesssim 10^{-2}$ km^{-1} s. Furthermore, due to different nature of temperature fluctuations produced by the early, mid, and late models, we are able to distinguish between these models at k modes $\lesssim 10^{-2}$ km^{-1} s. For higher k modes (k $\sim 10^{-1}$ km^{-1} s), the PDF of $\langle log(A_{\rm n})\rangle$ can be used to differentiate reionization models.

6.2 Future Scope

From the work done so far, we can establish that the temperature fluctuations differ significantly between the early and late reionization models. The results of the flux power spectrum, wavelet statistics, indicates the early model to have stronger temperature fluctuations in $4 \leq z \leq 5$. To further improve upon our findings in future, we plan to extend the analysis on a box size of 40 h^{-1}cMpc also verify with our present results. Since our present analysis does not include any instrumental effects and noise, we also plan to carry out analysis after incorporating noise from various sources, including instrumental broadening, signal-to-noise ratio (S/N), and continuum fitting uncertainties to make the data more realistic. Moreover, we will carry out our analysis on the $Ly\alpha$ forest observations working with the high resolution data from quasar spectroscopic surveys, such as KODIAQ (Keck Observatory Database of Ionized Absorption toward Quasars) and SQUAD (UVES Spectral Quasar Absorption Database). Comparing both the results from observations and simulation would help to detect the first observational detection of large-scale temperature fluctuations in the IGM.

The analysis that we perform for probing temperature fluctuations from H_I reionization can also be extended to probe the temperature fluctuation due to He_{II} reionization. Since quasars are the main sources that drive this process, this can be helpful to study quasar properties. The expansion rate of the Universe within $2 \leq z \leq 5$ can be measured by recording the redshift drift in the Lyα forest of distant quasars caused due to Hubble expansion. This method is known as Sandage-Loeb (SL) test. However, due to the presence of temperature fluctuations present in the IGM in the same redshift range, it becomes very difficult to carry out accurate measurements of the drift. Modeling the temperature fluctuations in the IGM at this redshift range can further help resolve this problem. Last but not least, with upcoming surveys such as Dark Energ Spectroscopic Instrument (DESI), WHT Enhanced Area Velocity Explorer (WEAVE), and Thirty Meter Telescope, will provide perform large survey of high resolution quasar spectra across broad wavelength range. This data will significantly improve the measurements of the small scale features of the Lyα forest. This would improve characterization of temperature fluctuations and help to develop a better understanding of the thermal history of the Universe.

References

Abdurashidova, Zara et al. (Feb. 2022). “First Results from HERA Phase I: Upper Limits on the Epoch of Reionization 21 cm Power Spectrum”. In: 925.2, 221, p. 221. doi: 10.3847/1538-4357/ac1c78. arXiv: 2108.02263 [astro-ph.CO].

Abel, Tom et al. (Jan. 2002). “The Formation of the First Star in the Universe”. In: *Science* 295.5552, pp. 93–98. doi: 10.1126/science.1063991. arXiv: astro-ph/0112088 [astro-ph].

Albrecht, A. & P. J. Steinhardt (Apr. 1982). “Cosmology for Grand Unified Theories with Radiatively Induced Symmetry Breaking”. In: 48.17, pp. 1220–1223. doi: 10.1103/PhysRevLett.48.1220.

Alpher, R. A. et al. (Apr. 1948). “The Origin of Chemical Elements”. In: *Phys. Rev.* 73 (7), pp. 803–804. doi: 10.1103/PhysRev.73.803. url: https://link.aps.org/doi/10.1103/PhysRev.73.803.

Bañados, Eduardo et al. (Jan. 2018). “An 800-million-solar-mass black hole in a significantly neutral Universe at a redshift of 7.5”. In: 553.7689, pp. 473–476. doi: 10.1038/nature25180. arXiv: 1712.01860 [astro-ph.GA].

Barkana, R. & A. Loeb (July 2001). “In the beginning: the first sources of light and the reionization of the universe”. In: 349.2, pp. 125–238. doi: 10.1016/S0370-1573(01)00019-9. arXiv: astro-ph/0010468 [astro-ph].

Barry, N. et al. (Oct. 2019). “Improving the Epoch of Reionization Power Spectrum Results from Murchison Widefield Array Season 1 Observations”. In: 884.1, 1, p. 1. doi: 10.3847/1538-4357/ab40a8. arXiv: 1909.00561 [astro-ph.IM].

Becker, George D. & James S. Bolton (Dec. 2013). “New measurements of the ionizing ultraviolet background over 2 < z < 5 and implications for hydrogen reionization”. In: 436.2, pp. 1023–1039. doi: 10.1093/mnras/stt1610. arXiv: 1307.2259 [astro-ph.CO].

Becker, George D. et al. (Jan. 2011). “Detection of extended He II reionization in the temperature evolution of the intergalactic medium”. In: 410.2, pp. 1096–1112. doi: 10.1111/j.1365-2966.2010.17507.x. arXiv: 1008.2622 [astro-ph.CO].

Becker, George D. et al. (Apr. 2013). “A refined measurement of the mean transmitted flux in the Lyα forest over $2 < z < 5$ using composite quasar spectra”. In: 430.3, pp. 2067–2081. doi: 10.1093/mnras/stt031. arXiv: 1208.2584 [astro-ph.CO].

Becker, George D. et al. (Mar. 2015a). “Evidence of patchy hydrogen reionization from an extreme Lyα trough below redshift six”. In: 447.4, pp. 3402–3419. doi: 10.1093/mnras/stu2646. arXiv: 1407.4850 [astro-ph.CO].

Becker, George D. et al. (Dec. 2015b). “Reionisation and High-Redshift Galaxies: The View from Quasar Absorption Lines”. In: 32, e045, e045. doi: 10.1017/pasa.2015.45. arXiv: 1510.03368 [astro-ph.CO].

Becker, Robert H. et al. (Dec. 2001). “Evidence for Reionization at z$\sim$6: Detection of a Gunn-Peterson Trough in a z=6.28 Quasar”. In: 122.6, pp. 2850–2857. doi: 10.1086/324231. arXiv: astro-ph/0108097 [astro-ph].

Bennett, C. L. et al. (Sept. 2003). “First-Year Wilkinson Microwave Anisotropy Probe (WMAP) Observations: Foreground Emission”. In: 148.1, pp. 97–117. doi: 10.1086/377252. arXiv: astro-ph/0302208 [astro-ph].

Bennett, C. L. et al. (Oct. 2013). “Nine-year Wilkinson Microwave Anisotropy Probe (WMAP) Observations: Final Maps and Results”. In: 208.2, 20, p. 20. doi: 10.1088/0067-0049/208/2/20. arXiv: 1212.5225 [astro-ph.CO].

Boera, Elisa et al. (July 2014). “The thermal history of the intergalactic medium down to redshift z = 1.5: a new curvature measurement”. In: 441.3, pp. 1916–1933. doi: 10.1093/mnras/stu660. arXiv: 1404.1083 [astro-ph.CO].

Boera, Elisa et al. (Feb. 2019). “Revealing Reionization with the Thermal History of the Intergalactic Medium: New Constraints from the Lyα Flux Power Spectrum”. In: 872.1, 101, p. 101. doi: 10.3847/1538-4357/aafee4. arXiv: 1809.06980 [astro-ph.CO].

Bolton, James S. & Martin G. Haehnelt (Nov. 2007). “The observed ionization rate of the intergalactic medium and the ionizing emissivity at z >= 5: evidence for a photon-starved and extended epoch of reionization”. In: 382.1, pp. 325–341. doi: 10.1111/j.1365-2966.2007.12372.x. arXiv: astro-ph/0703306 [astro-ph].

Bolton, James S. et al. (Mar. 2014). “A consistent determination of the temperature of the intergalactic medium at redshift z = 2.4”. In: 438.3, pp. 2499–2507. doi: 10.1093/mnras/stt2374. arXiv: 1308.4411 [astro-ph.CO].

Bolton, James S. et al. (Jan. 2017). “The Sherwood simulation suite: overview and data comparisons with the Lyman α forest at redshifts $2 \leq z \leq 5$”. In: 464.1, pp. 897–914. doi: 10.1093/mnras/stw2397. arXiv: 1605.03462 [astro-ph.CO].

Bonaldi, Anna (May 2018). “EoR imaging with the SKA: the challenge of foreground removal”. In: *Peering towards Cosmic Dawn*. Ed. by Vibor Jelić & Thijs van der Hulst. Vol. 333. IAU Symposium, pp. 269–273. doi: 10.1017/S1743921317010985.

Bosman, Sarah E. I. et al. (Sept. 2018). “New constraints on Lyman-α opacity with a sample of 62 quasarsat z > 5.7”. In: 479.1, pp. 1055–1076. doi: 10.1093/mnras/sty1344. arXiv: 1802.08177 [astro-ph.GA].

Bosman, Sarah E. I. et al. (July 2022). “Hydrogen reionization ends by z = 5.3: Lyman-α optical depth measured by the XQR-30 sample”. In: 514.1, pp. 55–76. doi: 10.1093/mnras/stac1046. arXiv: 2108.03699 [astro-ph.CO].

Bowman, Judd D. et al. (Mar. 2018). “An absorption profile centred at 78 megahertz in the sky-averaged spectrum”. In: 555.7694, pp. 67–70. doi: 10.1038/nature25792. arXiv: 1810.05912 [astro-ph.CO].

Bromm, Volker & Richard B. Larson (Sept. 2004). "The First Stars". In: 42.1, pp. 79–118. doi: 10.1146/annurev.astro.42.053102.134034. arXiv: astro-ph/0311019 [astro-ph].

Bromm, Volker & Naoki Yoshida (Sept. 2011). "The First Galaxies". In: 49.1, pp. 373–407. doi: 10.1146/annurev-astro-081710-102608. arXiv: 1102.4638 [astro-ph.CO].

Calverley, Alexander P. et al. (Apr. 2011). "Measurements of the ultraviolet background at 4.6 < z < 6.4 using the quasar proximity effect". In: 412.4, pp. 2543–2562. doi: 10.1111/j.1365-2966.2010.18072.x. arXiv: 1011.5850 [astro-ph.CO].

Cen, Renyue & Jeremiah P. Ostriker (Mar. 1999). "Where Are the Baryons?" In: 514.1, pp. 1–6. doi: 10.1086/306949. arXiv: astro-ph/9806281 [astro-ph].

Chakraborty, Anirban & Tirthankar Roy Choudhury (2026). "Reionization and its sources". In: *Encyclopedia of Astrophysics*. Vol. 4, pp. 433–452. doi: 10.1016/B978-0-443-21439-4.00088-2.

Chardin, Jonathan et al. (Mar. 2017). "Large-scale opacity fluctuations in the Lyα forest: evidence for QSOs dominating the ionizing UV background at z $\sim$ 5.5-6?" In: 465.3, pp. 3429–3445. doi: 10.1093/mnras/stw2943. arXiv: 1606.08231 [astro-ph.CO].

Chardin, Jonathan et al. (Jan. 2018). "A tale of seven narrow spikes and a long trough: constraining the timing of the percolation of H II bubbles at the tail end of reionization with ULAS J1120+0641". In: 473.1, pp. 765–775. doi: 10.1093/mnras/stx2362. arXiv: 1707.03841 [astro-ph.CO].

Choudhury, T. Roy et al. (Mar. 2021). "Studying the Lyman α optical depth fluctuations at z 5.5 using fast semi-numerical methods". In: 501.4, pp. 5782–5796. doi: 10.1093/mnras/stab045. arXiv: 2003.08958 [astro-ph.CO].

D'Aloisio, Anson et al. (Nov. 2015). "Large Opacity Variations in the High-redshift Lyα Forest: The Signature of Relic Temperature Fluctuations from Patchy Reionization". In: 813.2, L38, p. L38. doi: 10.1088/2041-8205/813/2/L38. arXiv: 1509.02523 [astro-ph.CO].

D'Aloisio, Anson et al. (Apr. 2019). "Heating of the Intergalactic Medium by Hydrogen Reionization". In: 874.2, 154, p. 154. doi: 10.3847/1538-4357/ab0d83. arXiv: 1807.09282 [astro-ph.CO].

Davé, Romeel et al. (May 2001). "Baryons in the Warm-Hot Intergalactic Medium". In: 552.2, pp. 473–483. doi: 10.1086/320548. arXiv: astro-ph/0007217 [astro-ph].

Davies, Frederick B. & Steven R. Furlanetto (Aug. 2016). "Large fluctuations in the hydrogen-ionizing background and mean free path following the epoch of reionization". In: 460.2, pp. 1328–1339. doi: 10.1093/mnras/stw931. arXiv: 1509.07131 [astro-ph.CO].

Davies, Frederick B. et al. (Mar. 2018). "A New Method to Measure the Post-reionization Ionizing Background from the Joint Distribution of Lyα and Lyβ Forest Transmission". In: 855.2, 106, p. 106. doi: 10.3847/1538-4357/aaaf70. arXiv: 1703.10174 [astro-ph.CO].

Davies, Frederick B. et al. (Jan. 2026). "Updated dark pixel fraction constraints on reionization's end from the Lyman-series forests of XQR−30". In: 545.2,

staf1862, staf1862. doi: 10.1093/mnras/staf1862. arXiv: 2510.25829 [astro-ph.CO].

de Lera Acedo, E. et al. (July 2022). "The REACH radiometer for detecting the 21-cm hydrogen signal from redshift z ≈ 7.5-28". In: *Nature Astronomy* 6, pp. 984–998. doi: 10.1038/s41550-022-01709-9. arXiv: 2210.07409 [astro-ph.CO].

Eilers, Anna-Christina et al. (Sept. 2018). "The Opacity of the Intergalactic Medium Measured along Quasar Sightlines at z˜ 6". In: 864.1, 53, p. 53. doi: 10.3847/1538-4357/aad4fd. arXiv: 1807.04229 [astro-ph.GA].

Fan, Xiaohui et al. (Dec. 2001). "A Survey of z>5.8 Quasars in the Sloan Digital Sky Survey. I. Discovery of Three New Quasars and the Spatial Density of Luminous Quasars at z∼6". In: 122.6, pp. 2833–2849. doi: 10.1086/324111. arXiv: astro-ph/0108063 [astro-ph].

Fan, Xiaohui et al. (July 2006). "Constraining the Evolution of the Ionizing Background and the Epoch of Reionization with z∼6 Quasars. II. A Sample of 19 Quasars". In: 132.1, pp. 117–136. doi: 10.1086/504836. arXiv: astro-ph/0512082 [astro-ph].

Faucher-Giguère, Claude-André et al. (Jan. 2008). "Numerical Simulations Unravel the Cosmic Web". In: *Science* 319.5859, p. 52. doi: 10.1126/science.1151476. arXiv: 0803.0147 [astro-ph].

Field, George B. (Jan. 1958). "Excitation of the Hydrogen 21-CM Line". In: *Proceedings of the IRE* 46, pp. 240–250. doi: 10.1109/JRPROC.1958.286741.

Gaikwad, Prakash et al. (Apr. 2017a). "Intergalactic Lyman continuum photon budget in the past 5 billion years". In: 466.1, pp. 838–860. doi: 10.1093/mnras/stw3086. arXiv: 1605.02738 [astro-ph.CO].

Gaikwad, Prakash et al. (May 2017b). "VoIgt profile Parameter Estimation Routine (viper): H I photoionization rate at z < 0.5". In: 467.3, pp. 3172–3187. doi: 10.1093/mnras/stx248. arXiv: 1610.06572 [astro-ph.CO].

Gaikwad, Prakash et al. (Feb. 2018). "Efficient adiabatic hydrodynamical simulations of the high-redshift intergalactic medium". In: 474.2, pp. 2233–2258. doi: 10.1093/mnras/stx2859. arXiv: 1705.05374 [astro-ph.CO].

Gaikwad, Prakash et al. (Dec. 2019). "Effect of non-equilibrium ionization on derived physical conditions of the high-z intergalactic medium". In: 490.2, pp. 1588–1604. doi: 10.1093/mnras/stz2692. arXiv: 1812.01016 [astro-ph.CO].

Gaikwad, Prakash et al. (June 2020). "Probing the thermal state of the intergalactic medium at z > 5 with the transmission spikes in high-resolution Ly α forest spectra". In: 494.4, pp. 5091–5109. doi: 10.1093/mnras/staa907. arXiv: 2001.10018 [astro-ph.CO].

Gaikwad, Prakash et al. (Sept. 2021). "A consistent and robust measurement of the thermal state of the IGM at $2 \leq z \leq 4$ from a large sample of Ly α forest spectra: evidence for late and rapid He II reionization". In: 506.3, pp. 4389–4412. doi: 10.1093/mnras/stab2017. arXiv: 2009.00016 [astro-ph.CO].

Gaikwad, Prakash et al. (Nov. 2023). "Measuring the photoionization rate, neutral fraction, and mean free path of H I ionizing photons at $4.9 < z < 6.0$ from

a large sample of XShooter and ESI spectra". In: 525.3, pp. 4093–4120. doi: 10.1093/mnras/stad2566. arXiv: 2304.02038 [astro-ph.CO].
Gamow, G. (Oct. 1946). "Expanding Universe and the Origin of Elements". In: *Phys. Rev.* 70 (7-8), pp. 572–573. doi: 10.1103/PhysRev.70.572.2. url: https://link.aps.org/doi/10.1103/PhysRev.70.572.2.
Garaldi, Enrico et al. (May 2019). "Constraining the Tail End of Reionization Using Lyα Transmission Spikes". In: 876.1, 31, p. 31. doi: 10.3847/1538-4357/ab12dc. arXiv: 1902.07713 [astro-ph.CO].
Garzilli, A. et al. (Aug. 2012). "The intergalactic medium thermal history at redshift z = 1.7-3.2 from the Lyα forest: a comparison of measurements using wavelets and the flux distribution". In: 424.3, pp. 1723–1736. doi: 10.1111/j.1365-2966.2012.21223.x. arXiv: 1202.3577 [astro-ph.CO].
Gehlot, B. K. et al. (Sept. 2019). "The first power spectrum limit on the 21-cm signal of neutral hydrogen during the Cosmic Dawn at z = 20-25 from LOFAR". In: 488.3, pp. 4271–4287. doi: 10.1093/mnras/stz1937. arXiv: 1809.06661 [astro-ph.IM].
Gnedin, Nickolay Y. & Lam Hui (May 1998). "Probing the Universe with the Lyalpha forest - I. Hydrodynamics of the low-density intergalactic medium". In: 296.1, pp. 44–55. doi: 10.1046/j.1365-8711.1998.01249.x. arXiv: astro-ph/9706219 [astro-ph].
Gnedin, Nickolay Y. et al. (May 2017). "Cosmic Reionization on Computers: Properties of the Post-reionization IGM". In: 841.1, 26, p. 26. doi: 10.3847/1538-4357/aa6c24. arXiv: 1605.03183 [astro-ph.CO].
Greif, Thomas H. et al. (Aug. 2011). "Simulations on a Moving Mesh: The Clustered Formation of Population III Protostars". In: 737.2, 75, p. 75. doi: 10.1088/0004-637X/737/2/75. arXiv: 1101.5491 [astro-ph.CO].
Greig, Bradley et al. (Apr. 2017). "Are we witnessing the epoch of reionisation at z = 7.1 from the spectrum of J1120+0641?" In: 466.4, pp. 4239–4249. doi: 10.1093/mnras/stw3351. arXiv: 1606.00441 [astro-ph.CO].
Greig, Bradley et al. (Apr. 2019). "Constraints on reionization from the z = 7.5 QSO ULASJ1342+0928". In: 484.4, pp. 5094–5101. doi: 10.1093/mnras/stz230. arXiv: 1807.01593 [astro-ph.CO].
Gunn, James E. & Bruce A. Peterson (Nov. 1965). "On the Density of Neutral Hydrogen in Intergalactic Space." In: 142, pp. 1633–1636. doi: 10.1086/148444.
Guth, Alan H. (Jan. 1981). "Inflationary universe: A possible solution to the horizon and flatness problems". In: 23.2, pp. 347–356. doi: 10.1103/PhysRevD.23.347.
Haardt, Francesco & Piero Madau (Feb. 2012). "Radiative Transfer in a Clumpy Universe. IV. New Synthesis Models of the Cosmic UV/X-Ray Background". In: 746.2, 125, p. 125. doi: 10.1088/0004-637X/746/2/125. arXiv: 1105.2039 [astro-ph.CO].
Haiman, Zoltan (Jan. 2000). "The Radiative Feedback from the First Stars and Quasars and the End of the Dark Age". In: *The First Stars*. Ed. by Achim Weiss et al., p. 219. doi: 10.1007/10719504_42.
Hiss, Hector et al. (Sept. 2018). "A New Measurement of the Temperature-density Relation of the IGM from Voigt Profile Fitting". In: 865.1, 42, p. 42. doi: 10.3847/1538-4357/aada86. arXiv: 1710.00700 [astro-ph.CO].

Hu, Wayne & Martin White (Apr. 1997). "The Damping Tail of Cosmic Microwave Background Anisotropies". In: 479.2, pp. 568–579. doi: 10.1086/303928. arXiv: astro-ph/9609079 [astro-ph].

Hui, Lam & Nickolay Y. Gnedin (Nov. 1997). "Equation of state of the photoionized intergalactic medium". In: 292.1, pp. 27–42. doi: 10.1093/mnras/292.1.27. arXiv: astro-ph/9612232 [astro-ph].

Jain, Divesh et al. (May 2024). "Probing the physics of reionization using kinematic Sunyaev-Zeldovich power spectrum from current and upcoming cosmic microwave background surveys". In: 530.1, pp. 35–51. doi: 10.1093/mnras/stae748. arXiv: 2311.00315 [astro-ph.CO].

Jin, Xiangyu et al. (Jan. 2023). "(Nearly) Model-independent Constraints on the Neutral Hydrogen Fraction in the Intergalactic Medium at z 5-7 Using Dark Pixel Fractions in Lyα and Lyβ Forests". In: 942.2, 59, p. 59. doi: 10.3847/1538-4357/aca678. arXiv: 2211.12613 [astro-ph.CO].

Keating, Laura C. et al. (July 2018). "Spatial fluctuations of the intergalactic temperature-density relation after hydrogen reionization". In: 477.4, pp. 5501–5516. doi: 10.1093/mnras/sty968. arXiv: 1709.05351 [astro-ph.CO].

Khaire, Vikram & Raghunathan Srianand (Apr. 2019). "New synthesis models of consistent extragalactic background light over cosmic time". In: 484.3, pp. 4174–4199. doi: 10.1093/mnras/stz174. arXiv: 1801.09693 [astro-ph.GA].

Kim, T. -S. et al. (Jan. 2004). "The power spectrum of the flux distribution in the Lyman α forest of a large sample of UVES QSO absorption spectra (LUQAS)". In: 347.2, pp. 355–366. doi: 10.1111/j.1365-2966.2004.07221.x. arXiv: astro-ph/0308103 [astro-ph].

Kolopanis, Matthew et al. (Oct. 2019). "A Simplified, Lossless Reanalysis of PAPER-64". In: 883.2, 133, p. 133. doi: 10.3847/1538-4357/ab3e3a. arXiv: 1909.02085 [astro-ph.CO].

Koopmans, L. et al. (Apr. 2015). "The Cosmic Dawn and Epoch of Reionisation with SKA". In: *Advancing Astrophysics with the Square Kilometre Array (AASKA14)*, 1, p. 1. doi: 10.22323/1.215.0001. arXiv: 1505.07568 [astro-ph.CO].

Kulkarni, Girish et al. (Aug. 2013). "Chemical Enrichment of Damped Lyα Systems as a Direct Constraint on Population III Star Formation". In: 772.2, 93, p. 93. doi: 10.1088/0004-637X/772/2/93. arXiv: 1301.4201 [astro-ph.CO].

Kulkarni, Girish et al. (Oct. 2015). "Characterizing the Pressure Smoothing Scale of the Intergalactic Medium". In: 812.1, 30, p. 30. doi: 10.1088/0004-637X/812/1/30. arXiv: 1504.00366 [astro-ph.CO].

Kulkarni, Girish et al. (May 2019). "Large Ly α opacity fluctuations and low CMB τ in models of late reionization with large islands of neutral hydrogen extending to z < 5.5". In: 485.1, pp. L24–L28. doi: 10.1093/mnrasl/slz025. arXiv: 1809.06374 [astro-ph.CO].

Lidz, Adam et al. (July 2010). "A Measurement of Small-scale Structure in the 2.2 <= z <= 4.2 Lyα Forest". In: 718.1, pp. 199–230. doi: 10.1088/0004-637X/718/1/199. arXiv: 0909.5210 [astro-ph.CO].

Linde, A. D. (Feb. 1982). "A new inflationary universe scenario: A possible solution of the horizon, flatness, homogeneity, isotropy and primordial monopole

problems". In: *Physics Letters B* 108.6, pp. 389–393. doi: 10.1016/0370-2693(82)91219-9.

Liu, Adrian et al. (Sept. 2009). "An improved method for 21-cm foreground removal". In: 398.1, pp. 401–406. doi: 10.1111/j.1365-2966.2009.15156.x. arXiv: 0903.4890 [astro-ph.CO].

Lukić, Zarija et al. (Feb. 2015). "The Lyman α forest in optically thin hydrodynamical simulations". In: 446.4, pp. 3697–3724. doi: 10.1093/mnras/stu2377. arXiv: 1406.6361 [astro-ph.CO].

Madau, Piero & Tassos Fragos (May 2017). "Radiation Backgrounds at Cosmic Dawn: X-Rays from Compact Binaries". In: 840.1, 39, p. 39. doi: 10.3847/1538-4357/aa6af9. arXiv: 1606.07887 [astro-ph.GA].

Madau, Piero et al. (Apr. 1999). "Radiative Transfer in a Clumpy Universe. III. The Nature of Cosmological Ionizing Sources". In: 514.2, pp. 648–659. doi: 10.1086/306975. arXiv: astro-ph/9809058 [astro-ph].

Maitra, Soumak et al. (Oct. 2019). "Three- and two-point spatial correlations of intergalactic medium at z 2 using projected quasar triplets". In: p. 2422. doi: 10.1093/mnras/stz2828. arXiv: 1907.02086 [astro-ph.CO].

Makinen, T. Lucas et al. (Apr. 2021). "deep21: a deep learning method for 21 cm foreground removal". In: 2021.4, 081, p. 081. doi: 10.1088/1475-7516/2021/04/081. arXiv: 2010.15843 [astro-ph.CO].

Mason, Charlotte A. et al. (Mar. 2018). "The Universe Is Reionizing at z $\sim$ 7: Bayesian Inference of the IGM Neutral Fraction Using Lyα Emission from Galaxies". In: 856.1, 2, p. 2. doi: 10.3847/1538-4357/aab0a7. arXiv: 1709.05356 [astro-ph.CO].

Mason, Charlotte A. et al. (May 2019). "Inferences on the timeline of reionization at z $\sim$ 8 from the KMOS Lens-Amplified Spectroscopic Survey". In: 485.3, pp. 3947–3969. doi: 10.1093/mnras/stz632. arXiv: 1901.11045 [astro-ph.CO].

McDonald, Patrick (Mar. 2003). "Toward a Measurement of the Cosmological Geometry at z $\backsim$2: Predicting Lyα Forest Correlation in Three Dimensions and the Potential of Future Data Sets". In: 585.1, pp. 34–51. doi: 10.1086/345945. arXiv: astro-ph/0108064 [astro-ph].

McGreer, Ian D. et al. (Aug. 2011). "The first (nearly) model-independent constraint on the neutral hydrogen fraction at z $\sim$ 6". In: 415.4, pp. 3237–3246. doi: 10.1111/j.1365-2966.2011.18935.x. arXiv: 1101.3314 [astro-ph.CO].

McGreer, Ian D. et al. (Feb. 2015). "Model-independent evidence in favour of an end to reionization by z $\approx$ 6". In: 447.1, pp. 499–505. doi: 10.1093/mnras/stu2449. arXiv: 1411.5375 [astro-ph.CO].

Mertens, F. G. et al. (Apr. 2020). "Improved upper limits on the 21 cm signal power spectrum of neutral hydrogen at z $\approx$ 9.1 from LOFAR". In: 493.2, pp. 1662–1685. doi: 10.1093/mnras/staa327. arXiv: 2002.07196 [astro-ph.CO].

Miralda-Escudé, Jordi et al. (Feb. 2000). "Reionization of the Inhomogeneous Universe". In: 530.1, pp. 1–16. doi: 10.1086/308330. arXiv: astro-ph/9812306 [astro-ph].

Mo, H. J. et al. (Nov. 2005). “Pre-heating by pre-virialization and its impact on galaxy formation”. In: 363.4, pp. 1155–1166. doi: 10.1111/j.1365-2966.2005.09512.x. arXiv: astro-ph/0506516 [astro-ph].

Mo, Houjun et al. (2010). *Galaxy Formation and Evolution*. doi: 10.1017/CBO9780511807244.

Molaro, Margherita et al. (July 2022). “The effect of inhomogeneous reionisation on the Lyman alpha forest”. In: 1028, p. 1028.

Napolitano, L. et al. (Jan. 2025). “Seven wonders of Cosmic Dawn: JWST confirms a high abundance of galaxies and AGN at z □ 9─11 in the GLASS field”. In: 693, A50, A50. doi: 10.1051/0004-6361/202452090. arXiv: 2410.10967 [astro-ph.GA].

Nasir, Fahad & Anson D’Aloisio (Oct. 2019). “Observing the tail of reionization: neutral islands in the $z = 5.5$ Lyman-α Forest”. In: *arXiv e-prints*, arXiv:1910.03570, arXiv:1910.03570. arXiv: 1910.03570 [astro-ph.CO].

Nikolić, Ivan et al. (Dec. 2023). “Inferring reionization and galaxy properties from the patchy kinetic Sunyaev-Zel’dovich signal”. In: 526.2, pp. 3170–3183. doi: 10.1093/mnras/stad2961. arXiv: 2307.01265 [astro-ph.CO].

Ostriker, J. P. & E. T. Vishniac (July 1986). “Generation of Microwave Background Fluctuations from Nonlinear Perturbations at the ERA of Galaxy Formation”. In: 306, p. L51. doi: 10.1086/184704.

Parsons, Aaron R. et al. (Apr. 2010). “The Precision Array for Probing the Epoch of Re-ionization: Eight Station Results”. In: 139.4, pp. 1468–1480. doi: 10.1088/0004-6256/139/4/1468. arXiv: 0904.2334 [astro-ph.CO].

Peeples, Molly S. et al. (May 2010). “Pressure support versus thermal broadening in the Lyman α forest - I. Effects of the equation of state on longitudinal structure”. In: 404.3, pp. 1281–1294. doi: 10.1111/j.1365-2966.2010.16383.x. arXiv: 0910.0256 [astro-ph.CO].

Penzias, A. A. & R. W. Wilson (July 1965). “A Measurement of Excess Antenna Temperature at 4080 Mc/s.” In: 142, pp. 419–421. doi: 10.1086/148307.

Petrovic, Nada & S. Peng Oh (May 2011). “Systematic effects of foreground removal in 21-cm surveys of reionization”. In: 413.3, pp. 2103–2120. doi: 10.1111/j.1365-2966.2011.18276.x. arXiv: 1010.4109 [astro-ph.CO].

Planck Collaboration et al. (Nov. 2014). “Planck 2013 results. XVI. Cosmological parameters”. In: 571, A16, A16. doi: 10.1051/0004-6361/201321591. arXiv: 1303.5076 [astro-ph.CO].

Planck Collaboration et al. (Sept. 2016). “Planck 2015 results. XIII. Cosmological parameters”. In: 594, A13, A13. doi: 10.1051/0004-6361/201525830. arXiv: 1502.01589 [astro-ph.CO].

Planck Collaboration et al. (Sept. 2020). “Planck 2018 results. VI. Cosmological parameters”. In: 641, A6, A6. doi: 10.1051/0004-6361/201833910. arXiv: 1807.06209 [astro-ph.CO].

Pritchard, Jonathan R. & Abraham Loeb (Aug. 2012). “21 cm cosmology in the 21st century”. In: *Reports on Progress in Physics* 75.8, 086901, p. 086901. doi: 10.1088/0034-4885/75/8/086901. arXiv: 1109.6012 [astro-ph.CO].

Puchwein, Ewald et al. (July 2015). "The photoheating of the intergalactic medium in synthesis models of the UV background". In: 450.4, pp. 4081–4097. doi: 10.1093/mnras/stv773. arXiv: 1410.1531 [astro-ph.CO].

Puchwein, Ewald et al. (May 2019). "Consistent modelling of the meta-galactic UV background and the thermal/ionization history of the intergalactic medium". In: 485.1, pp. 47–68. doi: 10.1093/mnras/stz222. arXiv: 1801.04931 [astro-ph.GA].

Puchwein, Ewald et al. (Mar. 2023). "The Sherwood-Relics simulations: overview and impact of patchy reionization and pressure smoothing on the intergalactic medium". In: 519.4, pp. 6162–6183. doi: 10.1093/mnras/stac3761. arXiv: 2207.13098 [astro-ph.CO].

Rauch, Michael et al. (Nov. 1997). "The Opacity of the Lyα Forest and Implications for Ω_b and the Ionizing Background". In: 489.1, pp. 7–20. doi: 10.1086/304765. arXiv: astro-ph/9612245 [astro-ph].

Rorai, Alberto et al. (Apr. 2017). "Measurement of the small-scale structure of the intergalactic medium using close quasar pairs". In: *Science* 356.6336, pp. 418–422. doi: 10.1126/science.aaf9346. arXiv: 1704.08366 [astro-ph.CO].

Schaye, Joop et al. (Nov. 1999). "Measuring the equation of state of the intergalactic medium". In: 310.1, pp. 57–70. doi: 10.1046/j.1365-8711.1999.02956.x. arXiv: astro-ph/9906271 [astro-ph].

Schaye, Joop et al. (Nov. 2000). "The thermal history of the intergalactic medium*". In: 318.3, pp. 817–826. doi: 10.1046/j.1365-8711.2000.03815.x. arXiv: astro-ph/9912432 [astro-ph].

Singh, Saurabh et al. (Apr. 2018). "SARAS 2: a spectral radiometer for probing cosmic dawn and the epoch of reionization through detection of the global 21-cm signal". In: *Experimental Astronomy* 45.2, pp. 269–314. doi: 10.1007/s10686-018-9584-3. arXiv: 1710.01101 [astro-ph.IM].

Spergel, D. N. et al. (Sept. 2003). "First-Year Wilkinson Microwave Anisotropy Probe (WMAP) Observations: Determination of Cosmological Parameters". In: 148.1, pp. 175–194. doi: 10.1086/377226. arXiv: astro-ph/0302209 [astro-ph].

Spina, Benedetta et al. (Aug. 2024). "Damping wings in the Lyman-α forest: A model-independent measurement of the neutral fraction at $5.4 < z < 6.1$". In: 688, L26, p. L26. doi: 10.1051/0004-6361/202450798. arXiv: 2405.12273 [astro-ph.CO].

Springel, Volker (Dec. 2005). "The cosmological simulation code GADGET-2". In: 364.4, pp. 1105–1134. doi: 10.1111/j.1365-2966.2005.09655.x. arXiv: astro-ph/0505010 [astro-ph].

Springel, Volker & Lars Hernquist (July 2002). "Cosmological smoothed particle hydrodynamics simulations: the entropy equation". In: 333.3, pp. 649–664. doi: 10.1046/j.1365-8711.2002.05445.x. arXiv: astro-ph/0111016 [astro-ph].

Sunyaev, R. A. & Ia. B. Zeldovich (Jan. 1980). "Microwave background radiation as a probe of the contemporary structure and history of the universe". In: 18, pp. 537–560. doi: 10.1146/annurev.aa.18.090180.002541.

Telikova, K. N. et al. (Dec. 2019). “Thermal State of the Intergalactic Medium at z=2-4”. In: 887.2, 205, p. 205. doi: 10.3847/1538-4357/ab52fe. arXiv: 1910.13184 [astro-ph.CO].

Theuns, Tom et al. (Dec. 1998). “P3 M-SPH simulations of the Lyalpha forest”. In: 301.2, pp. 478–502. doi: 10.1046/j.1365-8711.1998.02040.x. arXiv: astro-ph/9805119 [astro-ph].

Theuns, Tom et al. (July 2000). “Broadening of QSO Lyα forest absorbers”. In: 315.3, pp. 600–610. doi: 10.1046/j.1365-8711.2000.03423.x. arXiv: astro-ph/9908288 [astro-ph].

Theuns, Tom et al. (Aug. 2002a). “Detection of He II Reionization in the Sloan Digital Sky Survey Quasar Sample”. In: 574.2, pp. L111–L114. doi: 10.1086/342531. arXiv: astro-ph/0206319 [astro-ph].

Theuns, Tom et al. (May 2002b). “Temperature fluctuations in the intergalactic medium”. In: 332.2, pp. 367–382. doi: 10.1046/j.1365-8711.2002.05316.x. arXiv: astro-ph/0110600 [astro-ph].

Trenti, Michele et al. (Aug. 2009). “Metal-free Gas Supply at the Edge of Reionization: Late-epoch Population III Star Formation”. In: 700.2, pp. 1672–1679. doi: 10.1088/0004-637X/700/2/1672. arXiv: 0905.4504 [astro-ph.CO].

Trott, Cathryn M. et al. (Apr. 2020). “Deep multiredshift limits on Epoch of Reionization 21 cm power spectra from four seasons of Murchison Widefield Array observations”. In: 493.4, pp. 4711–4727. doi: 10.1093/mnras/staa414. arXiv: 2002.02575 [astro-ph.CO].

Upton Sanderbeck, Phoebe R. et al. (Aug. 2016). “Models of the thermal evolution of the intergalactic medium after reionization”. In: 460.2, pp. 1885–1897. doi: 10.1093/mnras/stw1117. arXiv: 1511.05992 [astro-ph.CO].

Valageas, P. et al. (June 2002). “The phase-diagram of cosmological baryons”. In: 388, pp. 741–757. doi: 10.1051/0004-6361:20020548. arXiv: astro-ph/0112273 [astro-ph].

Viel, Matteo et al. (Nov. 2004). “Inferring the dark matter power spectrum from the Lyman α forest in high-resolution QSO absorption spectra”. In: 354.3, pp. 684–694. doi: 10.1111/j.1365-2966.2004.08224.x. arXiv: astro-ph/0404600 [astro-ph].

Walther, Michael et al. (Feb. 2019). “New Constraints on IGM Thermal Evolution from the Lyα Forest Power Spectrum”. In: 872.1, 13, p. 13. doi: 10.3847/1538-4357/aafad1. arXiv: 1808.04367 [astro-ph.CO].

Wang, Feige et al. (June 2020). “A Significantly Neutral Intergalactic Medium Around the Luminous z = 7 Quasar J0252-0503”. In: 896.1, 23, p. 23. doi: 10.3847/1538-4357/ab8c45. arXiv: 2004.10877 [astro-ph.GA].

Woosley, S. E. et al. (Nov. 2002). “The evolution and explosion of massive stars”. In: *Reviews of Modern Physics* 74.4, pp. 1015–1071. doi: 10.1103/RevModPhys.74.1015.

Worseck, Gábor et al. (Dec. 2014). “The Giant Gemini GMOS survey of z > 4.4 quasars - I. Measuring the mean free path across cosmic time”. In: 445.2, pp. 1745–1760. doi: 10.1093/mnras/stu1827. arXiv: 1402.4154 [astro-ph.CO].

Wu, Xiaohan et al. (Dec. 2019). “Imprints of temperature fluctuations on the z $\sim$ 5 Lyman-α forest: a view from radiation-hydrodynamic simulations of

reionization". In: 490.3, pp. 3177–3195. doi: 10.1093/mnras/stz2807. arXiv: 1907.04860 [astro-ph.CO].

Yang, Jinyi et al. (Nov. 2020a). "Measurements of the z ∼ 6 Intergalactic Medium Optical Depth and Transmission Spikes Using a New z > 6.3 Quasar Sample". In: 904.1, 26, p. 26. doi: 10.3847/1538-4357/abbc1b. arXiv: 2009.13544 [astro-ph.GA].

Yang, Jinyi et al. (July 2020b). "Pōniuā'ena: A Luminous z = 7.5 Quasar Hosting a 1.5 Billion Solar Mass Black Hole". In: 897.1, L14, p. L14. doi: 10.3847/2041-8213/ab9c26. arXiv: 2006.13452 [astro-ph.GA].

Zaldarriaga, Matias (Jan. 2002). "Searching for Fluctuations in the Intergalactic Medium Temperature Using the Lyα Forest". In: 564.1, pp. 153–161. doi: 10.1086/324212. arXiv: astro-ph/0102205 [astro-ph].

Zaldarriaga, Matias et al. (Oct. 1997). "Microwave Background Constraints on Cosmological Parameters". In: 488.1, pp. 1–13. doi: 10.1086/304692. arXiv: astro-ph/9702157 [astro-ph].

Zhu, Yongda (May 2024). "Constraining the Intergalactic Medium During the Later Stages of Reionization Using QSO Spectra". PhD thesis. University of California, Riverside.

Zhu, Yongda et al. (June 2022). "Long Dark Gaps in the Lyβ Forest at z < 6: Evidence of Ultra-late Reionization from XQR-30 Spectra". In: 932.2, 76, p. 76. doi: 10.3847/1538-4357/ac6e60. arXiv: 2205.04569 [astro-ph.CO].